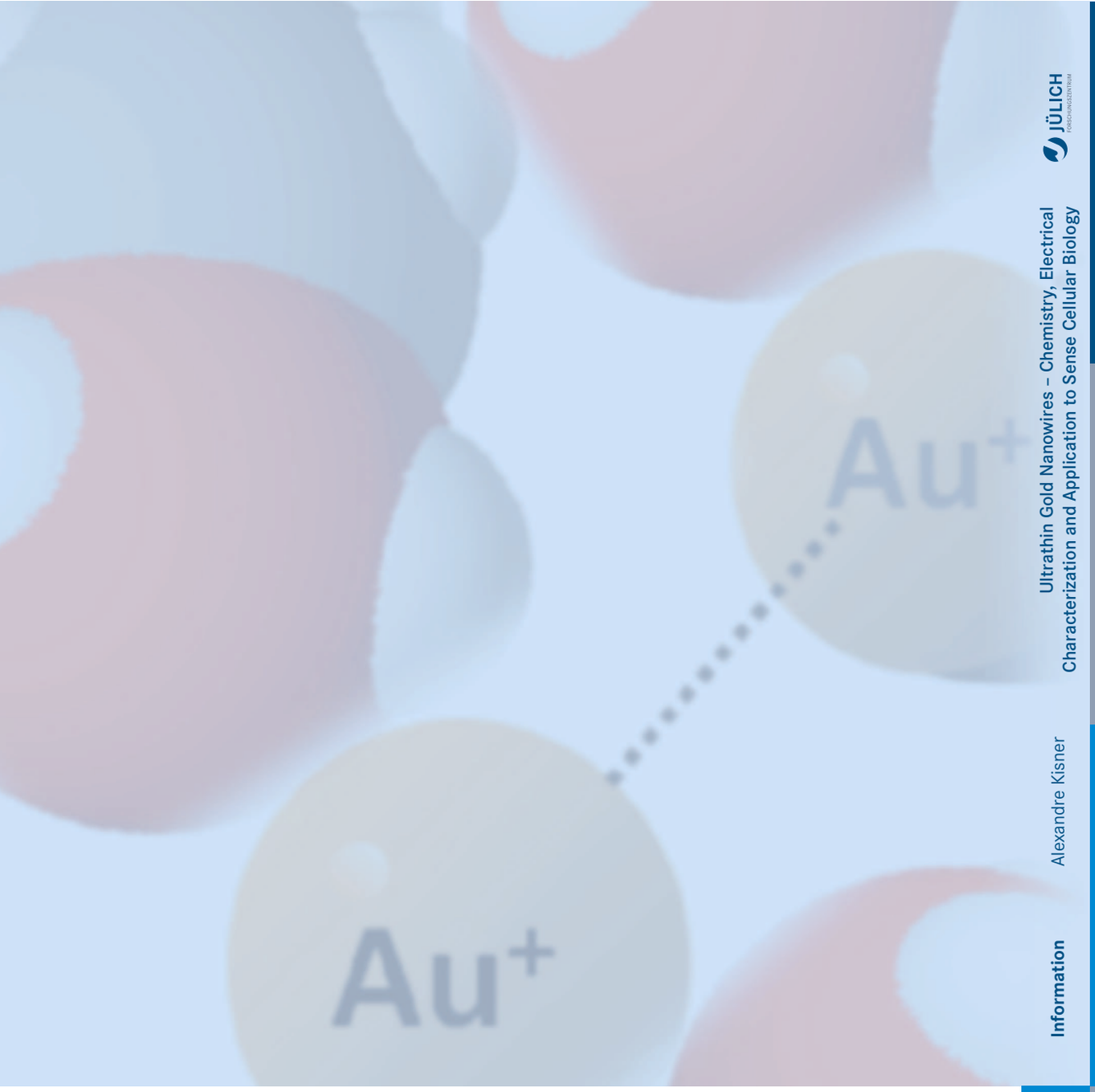

Information / Information
Band / Volume 24
ISBN 978-3-89336-824-2

JÜLICH
FORSCHUNGSZENTRUM

24

Member of the Helmholtz Association

Alexandre Kisner

Information

Ultrathin Gold Nanowires – Chemistry, Electrical Characterization and Application to Sense Cellular Biology

JÜLICH
FORSCHUNGSZENTRUM

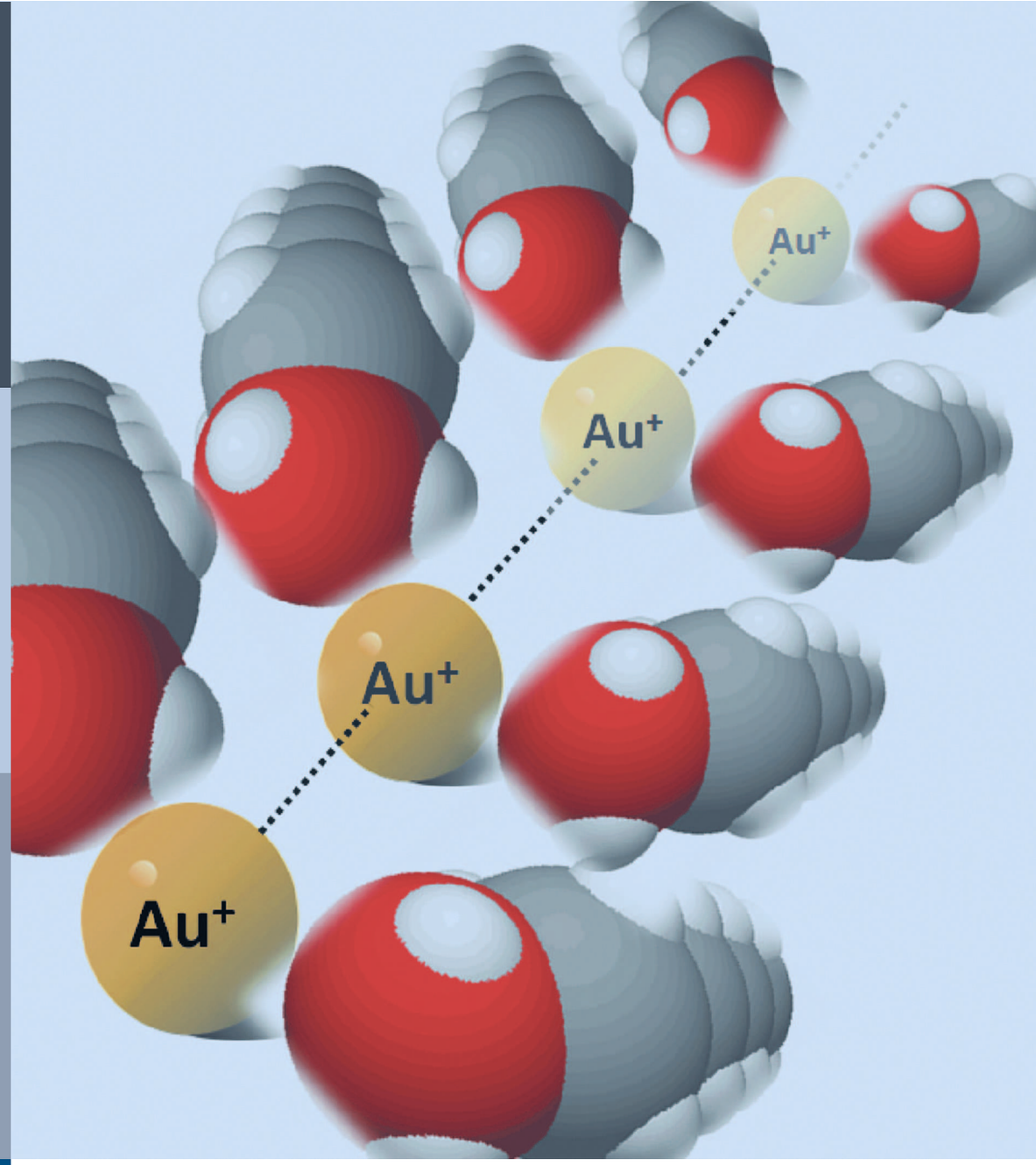

Ultrathin Gold Nanowires – Chemistry, Electrical Characterization and Application to Sense Cellular Biology

Alexandre Kisner

JÜLICH
FORSCHUNGSZENTRUM

Schriften des Forschungszentrums Jülich
Reihe Information / Information Band / Volume 24

Forschungszentrum Jülich GmbH
Peter Grünberg Institute / Institute of Complex Systems (PGI / ICS)
Bioelectronics (PGI-8 / ICS-8)

Ultrathin Gold Nanowires – Chemistry, Electrical Characterization and Application to Sense Cellular Biology

Alexandre Kisner

Schriften des Forschungszentrums Jülich
Reihe Information / Information

Band / Volume 24

ISSN 1866-1777

ISBN 978-3-89336-824-2

Bibliographic information published by the Deutsche Nationalbibliothek.
The Deutsche Nationalbibliothek lists this publication in the Deutsche
Nationalbibliografie; detailed bibliographic data are available in the
Internet at http://dnb.d-nb.de.

Publisher and Distributor: Forschungszentrum Jülich GmbH
Zentralbibliothek
52425 Jülich
Phone +49 (0) 24 61 61-53 68 · Fax +49 (0) 24 61 61-61 03
e-mail: zb-publikation@fz-juelich.de
Internet: http://www.fz-juelich.de/zb

Cover Design: Grafische Medien, Forschungszentrum Jülich GmbH

Printer: Grafische Medien, Forschungszentrum Jülich GmbH

Schriften des Forschungszentrums Jülich
Reihe Information / Information Band / Volume 24

D 82 (Diss., RWTH Aachen University, 2012)

ISSN 1866-1777
ISBN 978-3-89336-824-2

The complete volume is freely available on the Internet on the Jülicher Open Access Server (JUWEL) at
http://www.fz-juelich.de/zb/juwel

What if I were smiling and running into your arms ?

Would you see then what I see now ?

Last memorable quote from - Into the Wild

This thesis is dedicate to all those who believe that our most important job is to do all that we can to leave this world a better place than how we found it, and to teach others to do the same, because where there is willing and determination always there is also a transformation.

Abstract

The recent advances in the field of nanoscience and nanotechnology have motivated and challenged the fabrication of nanomaterials that can be assembled into functional networks. Based on this, ultrathin metal nanowires are considered essential building blocks that can be used to construct nanoelectronic devices for applications in sensors, photonics, and waveguides. In this thesis, we have endeavored to produce and understand the synthesis of ultrathin gold (Au) nanowires with diameter of ≈ 2 nm and lengths of up to 8 µm (aspect ratio of about 4,000). The nanowires could be synthesized employing a simple wet chemical approach using the organic molecule cis-oleylamine and AuCl as a metal precursor. Cis-oleylamine acted simultaneously as a surfactant, stabilizing and reducing agent of Au(I) ions, avoiding in this case the addition of further chemicals into the reaction. The influence of relativistic effects in the liquid phase solution of Au ions in an oxidation state +1 was investigated and demonstrated that these Au(I) species can form complexes with oleylamine. These complexes, which are believed to be formed through aurophilic interactions can induce as demonstrated from a series of spectroscopic techniques, the formation of such ultrathin nanowires.

Electrical resistors based on Au nanowire devices were produced through the assembly of these nanowires over silicon/silicon dioxide surfaces having lithographically produced metal electrodes to electrically contact the nanowires. Electrical characterization showed that the ultrathin Au nanowires present an increase in electrical resistance that was predicted by size effects. Additionally, correlating with observations from analysis of high-resolution transmission electron microscopy, which showed that the surface of the nanowires after the synthesis was covered with oleylamines molecules, the influence of contact resistance in the junction nanowires-metal electrodes was investigated. Measurements of resistance dependent on temperature demonstrated that the junction resistances were dominant and the linear electrical conduction presented an activation energy only near room temperature. Surface modification of nanowires with alkanethiols presenting functional groups with different charges when ionized showed that the electrical resistance of nanowires can readily be affected by minute amounts of these molecules on their surface. Besides, I–V curves of these devices in solution demonstrated that the ionic charges of functional groups of alkanethiols can promote re-arrangements in electrical double layer, and this can directly influence the electrical transport on the nanowires.

Finally, it was shown that these devices were biocompatible and neuronal cells were nicely grown on their top. Attempts to electrically stimulate and record ionic currents from these cells were performed and demonstrated promising results to application of such nanowires in electrophysiological experiments with high spatial resolution.

Zusammenfassung

Die Fortschritte der letzten Zeit im Bereich der Nanowissenschaft und Nanotechnologie fordern die Herstellung von Nanomaterialien in Form von funktionellen Netzwerken. Ultradünne metallische Nanodrähte sind dafür wichtige Bauteile: Sie können benutzt werden, um nanoelektronische Bauteile für Sensorik, Photonik und Wellenleiter herzustellen. In dieser Arbeit haben wir die Herstellung ultradünner Gold-Nanodrähte mit etwa 2 nm Durchmesser und Längen bis etwa 8 µm (Größenverhältnis 4.000) erforscht.

Die Nanodrähte wurden mit einem einfachen nasschemischen Verfahren unter Verwendung des organischen Moleküls cis-Oleylamin und Gold(I)-chlorid hergestellt. Cis-Oleylamin diente dabei gleichzeitig als oberflächenaktive Substanz, als Stabilisator und als Reduktionsmittel für die Gold(I)-Ionen, weshalb keine weiteren Reagenzien zugesetzt werden mussten. Der Einfluss relativistischer Effekte in flüssigen Lösungen von Gold(I)-Ionen wurde erforscht, und es wurde gezeigt, dass diese Gold(I)-Spezies Komplexe mit Oleylamin bilden. Man glaubt, dass solche Komplexe durch aurophile Interaktionen gebildet werden. Wie eine Reihe von Spektroskopischen Analysen gezeigt haben, können solche Interaktionen die Bildung ultradünner Gold-Nanodrähte bewirken. Lithographisch erzeugte Metall-Elektroden auf Silizium/Siliziumdioxid-Oberflächen wurden mit solchen Gold-Nanodrähten überbrückt, wodurch elektrische Widerstände gebildet wurden. Ihre elektrische Charakterisierung ergab, dass ihr elektrischer Widerstand in Einklang mit vorhergesagten verringerten Größeneffekten ist. Hochaufgelöste Transmissionselektronenmikroskopie ergab, dass die Nanodrähte nach ihrer Herstellung mit Oleylaminen überzogen sind. Daher wurde auch der Einfluss des Kontaktwiderstandes von Metallelektroden zu Nanodrähten untersucht. Die Messung des Widerstandes in Abhängigkeit von der Temperatur ergab, dass der Kontaktwiderstand (oder Brückenwiderstand) dominierte. Die Oberfläche der Nanodrähte wurde mit verschiedenen Alkanthiolen modifiziert, deren funktionelle Gruppen im ionisierten Zustand unterschiedliche Ladungen haben. Messungen ergaben, dass bereits winzige Mengen dieser Moleküle auf der Oberfläche den elektrischen Widerstand der Nanodrähte deutlich beeinflussten. Die Strom-Spannungs-Kennlinien solcher Bauelemente in Lösungen zeigten außerdem, dass die ionische Ladung funktioneller Gruppen an Alkanthiolen eine Umordnung der elektrochemischen Doppelschicht bewirken kann, was den elektrischen Transport in den Drähten direkt beeinflussen kann.

Zum Schluss wurde die Biokompatibilität solcher Bauelemente gezeigt, indem auf ihnen Neuronen gezüchtet wurden. Versuche zur Stimulation und Signalableitung von den Zellen ergaben vielversprechende Resultate und legen eine Verwendung der Bauelemente in elektrophysiologischen Versuchen mit hoher räumlicher Auflösung nahe.

CONTENTS

Chapter 1

Introduction

Research on low-scale materials represents an exciting and emergent interdisciplinary area that has begun to revolutionize a broad range of fields in chemistry, physics, engineering, energy, materials and life sciences. Advances in the development of materials on the nanoscale over the past decade have led to a significant increase in knowledge on the fabrication of powerful devices or functional systems, ranging from nanoscale transistors, light-emitting diodes (LEDs), nanolasers, nanoresonators, ultrasensitive chemical/biological sensors and very promising energy devices.[1-4] A central challenge in the successful building of new and useful types of technology based on nanomaterials is to exploit the "micro-macro" duality of such structures, where the consequences of miniaturization can be extended to understand the macro world. In this sense, two main paradigms in the field of nanoscience and nanotechnology have to be set up. The first is to develop a combination of tools and materials that allows us to make small structures and control the architecture of large structures on the nanometer length scale. The second important paradigm is to determine the chemical and physical consequences of miniaturization. This is where real nanoscience meets nanotechnology. Essentially, the central starting point for these challenges is the synthesis of the nanostructured materials, the building blocks in this case. The controllable and tunable chemical composition, structure, size, morphology, and consequently defined electronic, optical/magnetic properties are critical to comprehensively understand the fundamental properties of these nanoscale structures and to further explore their physical limits as functional devices.[1,5] Last but not least, there is the hierarchical assembly and organization of these building blocks into highly integrated systems with predictable and versatile functions.

Ultrathin (diameter < 10 nm) metal nanowires are of great interest for nanoscience studies as well as for nanotechnology applications.[6] Ultrathin nanowires, compared to other low-dimensional systems, present a higher surface area and have two quantum-confined directions,

while still leaving one unconfined direction for electrical conduction. This, for instance, enables metallic nanowires to be used in applications where electrical conduction, rather than tunneling transport, is required. In addition to the high surface area, the very high density of electronic states and joint density of states near the energies of their van Hove singularities, their enhanced exciton binding energy and increased surface scattering for electrons and phonons are just some of the ways in which nanowires differ from their corresponding bulk materials.[1,5]

The hierarchical assembly that eventually enables the organization of these unidimensional nanostructures is critical from an application standpoint, where certain properties can be independently controlled in nanowires, but not in their bulk counterparts.[5]A general example is the assembly and creation of a highly spatially resolved interface between nanowires and biological systems. Due to the similarity in size between natural nanostructures and nanowires, these latter represent a very sensitive tool for probing biological organisms. In fact, nanowire sensors are potentially smaller in size, more sensitive, demand less power and react faster than their macroscopic counterparts. Arrays of nanowire sensors could, in principle, achieve nanometer-scale spatial resolution and therefore provide accurate real-time information regarding not only the concentration of a specific analyte,but also its spatial distribution, as well as providing corresponding information on other analytes within the same submicron volume. Such arrays could be very useful, for example, for dynamic studies on the effects of chemical gradients on biological cells. The operation of sensors made with nanowires, nanotubes or nano-contacts is based mostly on the reversible change in the conductance of the nanostructure upon absorption of the agent to be detected, but other detection methods, such as mechanical and optical detection, are conceptually plausible.[2] The increased sensitivity and faster response time of nanowires is a result of the large surface-to-volume ratio, and the small cross-section available for conduction channels. On the other hand, in the bulk counterpart, the abundance of charges can effectively shield external fields, and the abundance of material can afford many alternative conduction channels. Therefore, a stronger chemical stimulus and longer response time is necessary to observe changes in the physical properties of a 3D sensor in comparison to a nanowire.

The chemical synthesis of ultrathin one-dimensional metallic nanowires is challenging for fundamental studies and further applications. Metal nanowires are usually produced by template-assisted techniques. However, the structures produced are generally polycrystalline and

present a diameter greater than 10 nm. Recently, a simple wet chemical approach using oleylamine has been reported for the synthesis of micrometer–long gold nanowires 2 nm in diameter.[7-12] Despite the success of the synthesis and the efforts to understand it, a series of questions and concerns remains. Improving this basic understanding of the production of ultrathin gold nanowires and their electrical characteristics as well as their application for sensing specific events in electrogenic cells is the focus of this thesis. Briefly, the chapters are organized as follow:

Chapter 2 presents the basic principles of the chemistry of gold and the relativistic effects that can be induced when appropriate chemicals are brought together for the synthesis of ultrathin gold nanowires. Moreover, basics of electric transport in nanowires in air and in solution are also given. The last part of this chapter discusses the electrical activity of electrogenic cells and how the metal nanowires can be used to sense it.

Chapter 3 describes the synthesis of ultrathin gold nanowires, their structural characterization using high-resolution transmission electron microscopy, and the preparation of nanowire devices to investigate their electrical transport and to be used as sensors.

Chapter 4 presents the results and discussion about the findings of the synthesis of nanowires and their structural and electrical characterization in air and in solution at room temperature, and also at cryogenic temperatures. Finally, the last part presents the data and the discussion on the experiments with neuronal cells.

Chapter 5 summarizes the conclusions of this thesis and provides an outlook for future research with such ultrathin gold nanowires.

Chapter 2

Fundamentals

This chapter will introduce the basic concepts about the chemistry of gold and how it can be exploited to synthesize ultrathin gold nanowires. A short overview of some methods commonly employed to fabricate gold nanowires and their limitation to produce high aspect ratio ultrathin nanowires is also presented. The fundamentals about the electrical properties of metal nanowires in air is discussed in Section 2.4, while the electrical effects of the electrical double layer formed on the interface metal nanowire/electrolyte is presented in Section 2.5. Section 2.6 introduces the concepts of how metal nanowires can be applied as nanoelectrodes to sense the electrical activity of neuronal cells. Finally, the objectives of this work are described in Section 2.8.

2.1 Gold (Au): A Noble Element

Undoubtedly, the most remarkable characteristic of Au is its inertness towards its reactivity with other atoms or molecules at the interface of a gas or a liquid state. The inertness of Au confers to it the title of the most noble of all metals. In principle, it does not mean a general inability of Au to form chemical bonds, by contrary Au is able to form very stable alloys with many other metals. It looks a paradox, but to understand this nobleness of Au one has to understand a simple surface reaction involving the dissociation of H_2 on the surface of Au and over other three metals (copper (Cu), nickel (Ni) and platinum (Pt)) lying close to it on the periodic table for comparison.[13] Figure 2.1A illustrates a schematic representation of the interaction between two electronic states of two atoms. Quantum mechanics assumes that the electronic states of two atoms overlapping are orthogonal to each other.[13] As a consequence, the down-shift of the bonding state is smaller than the up-shift of the antibonding state because the overlap of the initial states gives rise to an energy cost (Pauli repulsion) related to the

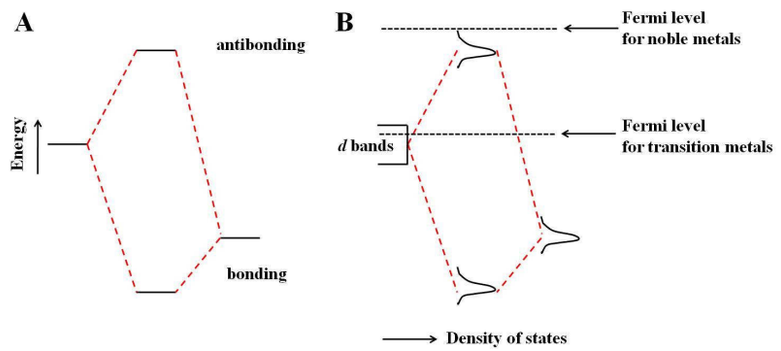

Figure 2.1. Illustration of the interaction between two electronic states. A- The simple case of two atomic states. B – The interaction between the *s* and *d* states of a metal with the states of an adsorbate on the surface of the metal. The Figure was adapted from [13].

orthogonalization of the two states.[13] In the case where only the bonding state becames occupied, an attractive interaction in the hybridization effect will occur and counteract against the ortogonalization energy cost. On the other hand, if the bonding and the antibonding states became occupied, no energy hybridization is gained and the ortogonalization energy remains.[13]

This context can now be extended for the molecular adsorption of H_2 on Au and also onto Cu, Ni and Pt (Figure 2.1A). For this case, the adsorbate-metal interaction should be considered in two steps. Firstly, the 1*s* state of hydrogen interacts with the 4*s* bands of transition-metals (Cu and Ni) or with 6*s* band from noble metals (Au and Pt). This interaction leads to a full filled bonding state and an empty antibonding state, which results in an attractive interaction that can be considered the same for all four surfaces. For the interaction of the bonding state with the metal *d* states, an extra shift induced by the hydrogen states in the bonding and in the antibonding state occurs. The energy of this hybridization interaction depends on the filling of the antiboding state and the coupling between the *s* and the *d* states, which determine the tendency for atomic chemisorptions energies.[13,14] The magnitude of these couplings is larger for the 5*d* metals than the 3*d* metals due to the more extended 5*d* states. As the orthogonalization energy increases with the magnitude of the coupling states, the energy cost increases down through the groups of the periodic table, making Au less reactive than the transition-metals.[1,2]

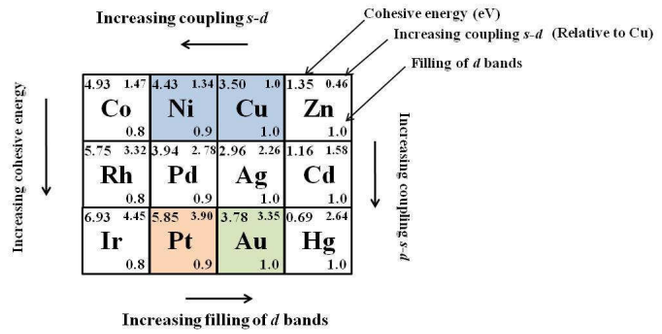

Figure 2.2. Schematics of the vicinity of Au in the periodic table showing the tendency for the *s* and *d* coupling, the filling of the metal *d* bands through the interaction adsorbate-metal *d* antibonding state, and the cohesive energy related to the ability of the metal to resist corrosion and dissolution. The Figure was adapted from [13].

In this sense, the two most important factors for the nobleness of the metals are: 1) the degree of filling of the antibonding adsorbate-metal *d* states and 2) the magnitude of the coupling states. While the filling increases to the right in the transition-metal series and is complete for the noble metals, the magnitude of the coupling states increases down through the groups of the periodic table, making the 5*d* metals the most noble.[13,14] Another important aspect is the ability of the metals to form stable bonds. The generation of a bond between adsorbate-metal means that a metal-metal bond should be broken, and this implies in an intrinsic cohesive energy of the metal. As it is demonstrated through Figure 2.2, the 5*d* metals have the largest cohesive energy and this justifies why these metals are more noble and also it explains why Pt is more noble than Cu despite the fact that Cu is less reactive than Pt.[13]

2.2 The Relativistic Effect on Au and the Aurophilicity Phenomenon

If on a metallic state Au presents an indistinguishable inertness, in its ionic state in solution phase this scenario is completely different. The atomic number (Z) of Au is 79 and its electronic ground state configuration is $[Xe][4f^{14}][5d^{10}][6s^{1}]$, which yields a large number of Au(I) compounds with a closed-shell configuration $[5d^{10}]$ similarly to the situation in Cu(I)

[$3d^{10}$] and silver (I) (Ag(I)) [$4d^{10}$]. However, as the first ionization potential of the isolated Au atom in the gas phase is higher (9.225 eV) in comparison to that for Ag (7.576 eV), the oxidation potential from Au(0) to Au(I) is high and makes as explained before, Au as a non-corrosive noble metal.[15] Owing to its relatively high oxidation potential and also its high electron affinity (electronegativity compared to iodine), only a few chemical compounds of Au are thermodynamically stable. Among these compounds are the halogens (F, Cl, Br and I) and the heavy chalcogens (Se and Te). Remarkably, this high redox potential and high electron affinitiy of Au in comparison to other elements with Z = 72–83 in the periodic table distinguish its tendency characteristics and can only be understood by combination with relativistic effects.[16] The influence of effects predicted by the theory of relativity in heavy-elements chemistry was only recognized in 1970s, but it always had a profound impact in the existing actinides and lanthanides. The general concept for the relativistic effects arises from the finite speed of light, c = 137.035 989 au, as compared to c = ∞. In the case of atoms with high atomic number, which present an increased nuclear point charge, the electrons in the outer shells reach velocities that approach the velocity of light. As a consequence, the relativistic mass of the electron (m_e) is increased as demonstrated by:[17]

$$m_e = m_0 / (1-(v_e/c))^{1/2} \qquad \text{(Eq. 2.1)}$$

being m_0 the rest mass and v_e the speed of the electron. The effective Bohr radius (a_0), which is given by

$$a_0 = (4\pi\varepsilon_0)(\hbar^2/me^2) \qquad \text{(Eq. 2.2)}$$

will decrease for inner shell electrons with large average speeds. For example, in the case of 1*s* shell at the non-relativistic limit, this average speed is Z au. Thereby, the 1*s* electron of mercury (Hg) has a ratio v_e/c of 80/137.035 989 = 0.58, implying a radial shrinkage of 23%. Because the higher *s* shells are assumed to be orthogonal against the lower ones, they suffer a similar contraction. Owing to interacting relativistic effects, this contraction can be extended, as in the case of Au, where the 6*s* shell has a larger relativistic effect than the 1*s* shell.[17,18] Among the transition and noble metals, this relativistic effect is more pronounced in Au and can be better visualized through Figure 2.3A, which exhibits a relation of the relativistic (r_{rel}) over a hypothetical non-relativistic ($r_{non-rel}$) radius of the valence electrons as a function of Z.[17]

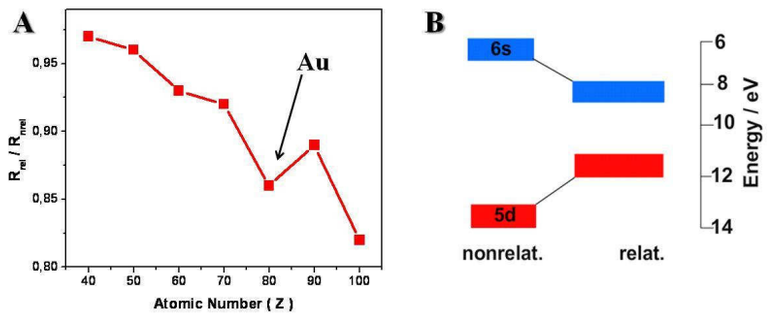

Figure 2.3. A- Plot of the ratio of relativistic (r_{rel}) over a hypothetical non-relativistic ($r_{non\text{-}rel}$) radius of 6*s* electrons as a function of the atomic number Z, showing the contraction of 6*s* in Au. The Figure was modified from [17]. B- Schematic illustration depicting the decrease of energy in the gap between orbitals *d* and *s* in Au.

Figure 2.3A clearly demonstrates that this ratio deviates from unity as Z is increased and reaches a pronounced local minimum at 79, the correspondent atomic number of Au. As pointed before, the main consequences of this strong influence of relativity at Au atom are a contraction of *s*-orbitals and an expansion of the *d*-orbitals.[17,18] This implies that the difference of energy to the valence shell electrons of different orbitals (*s*, *p*, *d*) is minimized, especially between the 6*s* and the 5*d* states, which are brought much closer as illustrated in Figure 2.3B.[18] A clear example of this effect is the color of bulk Au, which due to the small band gap between the full 5*d* band (expanded orbitals) and the Fermi level of the half-filled 6*s*-band (contracted orbitals), is yellow.[17]

It is notorious and intuitive that these atomic effects in Au have an influence not only on the metallic state, but also in its ionic state in solution phase. The small energy of the band gap between the filled 5*d* states and the empty 6*s* and 6*d* states for Au in an ionic state +1 (valence electronic configuration 5*d*) in solution, means that the affinity of this ions of closed-shell centers for each other is relatively high and Au(I)–Au(I) interactions can occur.[18-20] This interaction, also termed “aurophilic” or metallophilic interaction has an energy of 7–12 kcal/mol, which is comparable to those of hydrogen bondings.[18,19] Surprisingly, it overrules the Coulomb’s principle for repulsion of species having the same electrical charge. The discovery of these

interactions was done by Jones, who in the beginning of 1980s reported a series of surveys about structural work of Au complexes.[21-24] Jones noted an unusual mutual affinity of Au centers in all analyzed molecules. The linearly two-coordinate Au(I) complexes, L-Au-X, followed a structural pattern completely different from that of related complexes of metals (Cu, Ag) on the same period of the periodic table.[21-22] While the complexes with Cu and Ag formed dimmers or oligomers with the anionic ligand X approaching the cationic metal center, the oligomerization of Au compounds was governed by a close approach of the metal atoms. This approach may occur with the molecular axes parallel, anti-parallel or perpendicular, but in all the cases the interaction Au–Au represents the shortest distance between the molecular components. The typical distances for the Au–Au interactions observed were in a range of 2.8–3.3 Å, well below the sum of the van der Waals radii (ca. 3.6 Å).[21-23]

The valence state +1 of Au in solution seems to be a pre-requisite to observe the aurophilicity phenomenon. It was showed that on the oxidation state +1, Au has an ionic radius much smaller than Ag and in fact it is between Cu and Ag.[18] This small radius and also the small coordination number of two, enables Au(I) to form neutral or ionic compounds of general formula X-Au-Y, where the ligands X and Y can be the same or different and neutral or anionic. In a monovalent state, Au(I) minimizes also the steric hindrance and small and linear or unbranched chain-like ligands can form complexes with a linear or snake-like molecular shapes. In case the substituents are pointing away from the molecular axis, the complexes can adopt either a flat or a tree-root shape.[18]

2.2.1 Engineering new Materials from Aurophilic Interactions

Since the works reported by Jones in 1980s, aurophilic interactions have gained a lot of attention and research in the field of supramolecular chemistry has rapidly grown in the last decades leading to the generation of fascinating structural topologies with intrinsic physical properties.[25-27] In a similar manner of hydrogen bonding, π–π stacking and coordinate bonding, which are interactions that are usually applied to assembly supramolecular polymeric systems that can be extended to one-, two-, or three-dimensions, aurophilic interactions can also be used to structurally increase the dimensionality of new compounds and/or materials.[28] Figure 2.4 illustrates a cartoon showing how the aurophilic interactions could induce the assembly of an

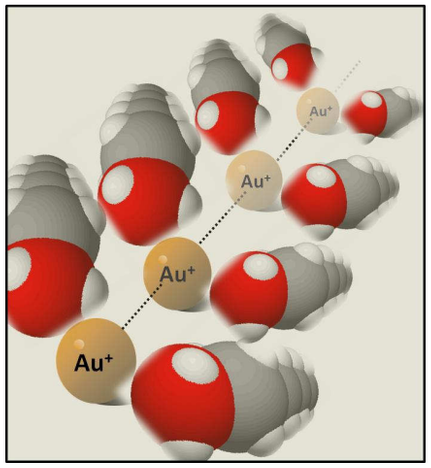

Figure 2.4. Illustration of aurophilic interactions inducing the assembly of organic molecules on Au(I) ions. In the hypothetical organic molecule the red balls represent nitrogen atoms, while gray balls are carbon and white balls are hydrogen.

aliphatic organic molecule having a primary amine group (-NH_2) as the moiety ligand, interacting in the perpendicular direction of a linear chain of Au(I) ions. This assembly can lead the molecules to aggregate into oligomers or polymers.[18,28] The complexes remain in the monomeric form only in cases where the steric bulk of the ligand prevents any close intermolecular Au-Au contacts. Thus, the degree of polymerization depends on the steric hindrance of the ligands, and this dependence may be altered if there are specific interactions between the ligands, in particular hydrogen bondings, π–π stacking or more often coordinate bonding.[19] Leznoff's group has been pioneer in this idea and has shown the combined synthesis of a series of compounds driven by aurophilic interactions and other heterometallic moieties. These compounds have a three-dimensional structure and present a large birefringence (D_n = 0.4).[28,29] Another interesting relation due to the molecular organization induced by Au–Au interactions was the formation of liquid crystals made of Au, which was revised by Espinet. However, in this case the role of Au in the molecular arrangement of these compounds is still ambiguous.[30]

Recently, Lu and co-workers reported that the molecular assembly induced by aurophilic interactions can also be used to synthesize ultrathin Au nanowires with diameter around 2 nm and length of a few micrometers.[9] Employing cis-oleylamine as a ligand and AuCl as a salt precursor, Lu *et al.* claimed that linear chains formed from [(oleylamine)AuCl] complex via aurophilic interaction can form bundles of polymeric strands. When Au(I) was reduced to Au(0), these polymeric strands could then act as a template to form such ultrathin nanowires.[9] Although the claims of Lu and co-workers about the aurophilic interactions were more speculative and the aurophilicity phenomenon was not clearly demonstrated experimentally, it still was a fascinating demonstration to the liquid phase synthesis of ultrathin metallic nanowires with a high aspect ratio. Although relatively simple, this synthesis is very ambiguous and the interactions between Au(I) ions and oleylamine molecules resembles other experiments involving similar ligand molecules, where aurophilic interactions were showed to occur.[31] Thus, it does not only instigate the understanding of these interactions, but also the production of ultrathin Au nanowires with such geometrical characteristics, which so far were not demonstrated by no other kind of synthesis or physical technique, as it will be introduced in next Section.

2.3 Synthesis of Au Nanowires

The recent advances in the field of nanoscience and nanotechnology have motivated and challenged the fabrication and the shrinkage of materials that can be rationally organized in functional networks. In this sense, nanowires are considered essential components that can be used to build nanoelectronic devices for applications in sensors, photonics, and waveguides.[5] Nanowires made of Au are extremely attractive for such applications because they are chemically inert, have low electrical resistance and can transport light over their axial direction.
The synthesis of Au nanowires has been widely reported on literature and it is the main focus of this Section that intends to present and compare those approaches with the one claimed by Lu and co-workers to produce Au nanowires through aurophilic interactions.

2.3.1 Template Based Synthesis

A general question that arises in the nanowires fabrication is how to assemble atoms or other building blocks into nanometer-scale objects with diameters much smaller than the available lengths ? There are many approaches to prepare 1D nanostructures.[32-35] As a whole, top-down and bottom-up methods are general strategies that have been carried out intensively. Particularly, electrochemical methods based on top-down or bottom-up represent a suitable alternative to get well arranged and defined one-dimensional nanostructures. In this context, template-based synthesis is one of the most successful bottom-up methods to prepare nanowires and nanotubes.[34,35] This method is based on substrate-like materials pursuing a set of poles and boards, which nanometer-sized structures are generated in situ and shaped into the pre-determined morphology of the template. A common template approach has been inspired in patterned surfaces. In this approach, either nano or microstructural defects are generated positively or negatively on the surface of a solid substrate using lithography and etching techniques. In the case of positive-template, wire-like nanostructures, such as DNA and carbon nanotubes (CNT) act as templates to guide in a posterior step the electrodeposition of the intended material on the surface of the template.[36-38] In this way, there is no physical restriction by template size and the diameter of the nanostructures may be controlled by adjusting the quantity of material deposited on the template.

In the negative-template method, V-like grooves structures are used to electrochemically deposit metal or semiconductors at the bottom of each groove. Using this simple procedure, continuous thin nanowires with lengths up to hundreds of micrometers may be prepared on the surface of solid substrates. These nanostructures can be sequentially released into free-standing form or transferred onto another support.[39] Indeed, this is one of the best advantages of template technique, that is, the template limits only physically the geometrical features of nanowires. After the synthesis, the template can selectively be removed by etching or calcination, allowing the collection of the resultant nanowires.

2.3.1.1 Mesoporous Templates

Other successful negative-templates are those based on nanoporous membranes. In that case, the nanometer-scale pores of membranes such as polycarbonate and anodic alumina or even zeolites are used to confine and grow the nanostructures.[40,41] Specifically, anodic alumina membranes (AAM) are of particular interest because their geometrical features (e.g., thickness, pore and cell diameter) and composition can easily be controlled experimentally. Furthermore, another interesting characteristic is the growth of arrays of self-organized hexagonal compacted cells with central pores parallel to each other and perpendicularly oriented to the substrate surface.[42] In this case, aluminum foils are usually anodized under constant voltage using a dilute acid electrolyte (e.g., H_2SO_4, H_3PO_4, $C_2H_2O_4$). It is important to note that the pore-size diameter can be controlled by the employed electrolyte.[43] For instance, anodization performed with sulphuric acid may yield pores with diameter smaller than 25 nm, whereas phosphoric acid may provide larger pores of about 500 nm. Meanwhile, anodized aluminum in oxalic acid solutions results in pores with diameters ranging from ~ 50 nm to ~ 400 nm. After anodizing, the aluminum substrate is removed and the AAM is soaked in an acid solution to remove a barrier layer formed at the bottom of the pores during the anodization. Finally, a conductive layer that serves as a cathode in an electrochemical cell is deposited in one side of AAM. Thus, wires or tubes with the pore-size diameters and lengths of several micrometers cannot only be growth by electrochemical deposition, but also by electroless plating solutions.

One of the pioneers to experience both kind of deposition was the Martin's group.[32,33] Unsurprisingly, the researches showed that electroless plating allowed for more uniform deposition, in this case Au, than electrochemical plating method. The differences in field distribution along the porous membrane were suggested as the main factor of these observations. In general, template-based methods represent a simple, highly-oriented, low effective cost and mass production way to fabricate nanowires and nanotubes from various materials. Interestingly, if one consider a nanoporous membrane with a constant lattice of 500 nm and a pore diameter of 400 nm, there will be 460,000,000 pores per square centimeter, which in theory might yield after a deposition procedure the same amount of nanowires.

2.3.2 Atomic Metal Wires from Electrochemical Etching / Deposition

All the electrochemical methods reported until now represent a promising approach to synthesize nanowires with controlled chemical composition and geometrical dimensions, however, they are difficult to produce nanowires with diameters shorter than 10 nm. Tao's group described an electrochemical method to fabricate quantum metal wires.[44] Using a thin metal wire pursuing only a small portion uncovered for a glue and supported onto a solid insulate substrate, the researchers exposed the uncovered portion of the wire to an electrolyte solution for electrodeposition and etching. This exposed portion which was less than a few micrometers was then reduced to the atomic scale, in which the conductance became quantized.[44]

An essential difference between the conductance sensitivity of these quantum metallic wires and those produced for example by template methods are the inherent wavelength and mean free path of electrons. Metals such as Au, Ag and Cu have wavelength of only a few angstroms and mean free path of a few tens of nm, which allows the conductance quantization be pronounced even at room temperature, as long as the diameter of metal wires reach the size of an atom. In contrast, conventional nanowires with diameters of a few tens of nanometers are not expected to present marked conductance sensitivity. Tao *et al*. observed that the atomically thin metal wires make the quantized conductance be sensitive to the adsorption of molecules onto the nanowire.[45,46] This high sensitivity allowed these materials to be applied as chemical sensors. However, some limitation such as selectivity should be overcome.

2.3.3 Solution Based Synthesis of Nanowires and Soft Matter Templates

Another common alternative to produce nanowires are the solution based methods. The nanowires synthesized using such methods have usually a smooth surface and are already dispersed in solution, without the need to be released from a hard template as the methods described previously.[47] Moreover, in comparison to the atomic nanowires produced by Tao's group, solution based methods offer, at least in theory, the possibility to synthesize readily ultrathin nanowires with high aspect ratio that are stable over the time, allowing these nanowires to be assembled into functional nanodevices with different configurations. Due to these

advantages of solution based methods, this Section will give a special focus on soft matter templates and show how a crystalline nanomaterial can be developed from these methods.

Solution based synthesis usually employs mesophasic structures such as surfactants, which form well known structures as micelles or inverse micelles when their concentration reaches a critical value in solution.[47] These anisotropic structures are also considered soft templates that can be used in combination with appropriate chemical or electrochemical reactions to synthesize one-dimensional materials, such as nanorods and/or nanowires. Some demonstration of this principle was already done with success by Wang *et at.*, who showed the synthesis of Au nanorods employing rod-like micelles of cetyltrimethylammonium bromide (CTBA).[48] In a similar manner, Murphy and co-workers used a seed mediated growth to synthesize Au nanorods with controllable thickness and aspect ratio.[49] Murphy *et al.* added Au nanoparticles of 3–5 nm diameter as seeds into a solution of CTBA containing a dissolved metal precursor as $HAuCl_4$. When a weak reducing agent was added to the solution, the seeds served as nucleation sites for the growth of nanorods within the confined micelle structure.[49] The experimental approach described by Lu and co-workers for synthesizing ultrathin Au nanowires via polymeric strands induced by aurophilic interaction resembles this soft template technique described in this Section. This synthesis was first reported by Halder and Ravishankar in 2007.[7] In that occasion, the authors did not mention about the influence of aurophilic interactions in the reaction and it was only in 2008 when four independent groups, including Lu and co-workers, reported almost at the same time and with a similar synthesis the production of ultrathin Au nanowires.[8-11] Considering that oleylamine is also a surfactant-like molecule, it would be very plausible to assume that a combined effect of the micellar configuration of this molecule with possible aurophilic interactions led to the synthesis of ultrathin Au nanowires. Based on these concepts, it is worth considering and revising the formation of a nanocrystal inside of a micelle since its beginning. The next Section will introduce some fundaments about the growth and the thermodynamic properties of nanocrystals.

2.3.3.1 Basic Concepts about Small Particles in Solution

The properties of nanomaterials are determined by a set of physical parameters that include its composition, structure, size and shape. Thus, understanding the rational assembly of

atoms into structures with nanometer size diameters but much longer lengths is one of the main basic chemistry and physics keys to prepare nanowires with tailored properties. As a first approximation to understand the formation of these structures, we have to consider a nucleation step. Nucleation can be generically described as the formation of a small cluster (nuclei) from atoms in the solution and it is a very important stage in any crystallization process because it represents the very primary stage of crystal formation, although it is still not clear how nuclei and crystals are evolved from a precursor.[50,51] In a solution-phase reaction, the nuclei can be formed either by decomposition or reduction of the precursor compound used. In this Section, we will focus in the reduction route because the reaction to form the ultrathin nanowires is based on an electroless process. In this route, it is not totally clear whether the precursor compound is firstly reduced into zero-valent atoms, which form the nuclei and then grow into nanocrystals or if the unreduced metal species begin forming nuclei prior to reduction. First-principle calculations have indicated that precursor compounds can be directly converted into nuclei and add to other precursor based nuclei or growing nanocrystals without going through a zero-valent state. The classical examples are the dimers Pt(II)-Pt(I), which are stabilized with Cl^- and Au(I)-Au(I) formed through aurophilic interactions. Due to the orbital delocalization, these dimers have a higher electron affinity than the precursor, thus reduction is expected to occur preferentially via electron transfer from the reductant to these dimeric units. In this way, the detachment of a ligand from a cluster can drastically accelerate the growth of a metal nanocrystal.[51]

During this process of cluster growth, structural fluctuations become energetically important so that the nuclei reaches a size with relatively stable crystallinity and well defined crystallographic facets exposed on its surface. This new structure now is termed as a “seed”. The shape of a seed is mainly determined by the minimization of surface energy. For a spherical single crystalline particle, the surface energy is relatively high because it must contain high index crystallography planes. Consequently, facets tend to form on the particle surface to increase the number of low index planes. This description is based in a reaction under thermodynamic control, which seeds attempt to minimize the total interfacial free energy of a system within a given volume. The interfacial free energy, γ_i, can be described as the energy required to form a unit area of a new surface through:[51]

$$\gamma = \left(\frac{\partial G}{\partial A}\right) \qquad \text{(Eq. 2.3)}$$

where G is free energy and A is the surface area. However, for newly formed seeds the crystal symmetry is broken due to missing bonds at the surface causing the surface atoms to be attracted toward the interior. To pull the surface atoms back to their original positions a restoring force is needed. In this context, the interfacial free energy is given by:[52]

$$\gamma = \frac{1}{2} N_b \varepsilon \rho_a \qquad \text{(Eq. 2.4)}$$

where N_b corresponds to the number of broken bonds, ε is the bond strength, and ρ_a is the density of surface atoms. For Au, which typically presents a face-centered-cubic (fcc) structure and has a lattice constant, a, of 4.080 Å, the surface energies of the low-index crystallographic facets that are often formed on nanocrystals can be estimated as: $\gamma\{100\} = 4(\varepsilon/a^2)$, $\gamma\{110\} = 4.24(\varepsilon/a^2)$, and $\gamma\{111\} = 3.36(\varepsilon/a^2)$, resulting in the energetic sequence of $\gamma\{111\} < \gamma\{100\} < \gamma\{110\}$. This sequence implies that for a single-crystal seed, the surface is a polyhedron (or Wulff polyhedron). For this reason, single-crystal seeds are expected to exist as truncated octahedrons enclosed by a mix of {111} and {100} facets, which yield a nearly spherical profile, and thus the smallest surface area to minimize the total interfacial free energy.[51,53,54]

After these stages, the seeds can still grow into a nanocrystal with several possible shapes. This growing process occurs through the adsorption of atoms to the seeds surface, and consequent diffusion of these adatoms around the surface until they find a step site where they can be incorporated. The growth step is then controlled by a competition between a decrease in bulk energy, which in fact thermodynamically favors the growth and an increase in surface energy that favors the dissolution. It is based on this dynamic interplay of growth and dissolution that seeds finally become nanocrystals.[51,54] As introduced previously, single crystal seeds tend to grow into polyhedrons, however, depending on surface capping agents, defect structures or crystal overgrowth, other possible crystals with different shapes can be produced. For example, Xia *et al.* demonstrated that polyvinylpyrrolidone (PVP), a polymeric capping agent, can be employed to produce nanocubes of Ag and Pd from single crystal seeds terminated with only {111} and {100} facets of those metals.[55] The use of capping agents to define the shape of a nanocrystal may be considered a thermodynamic control of the shape as it makes some facets thermodynamically more favorable by reducing their interfacial free energies through chemisorptions. This chemical interaction with a metal surface can change the order of free

energies for different crystallographic planes, and thus change also the relative growth rate for these planes. Consequently, a plane with slower addition rate will be more exposed on the nanocrystal surface. This effect is well observed through the work of Xia *et al.* with PVP to produce Ag and Pd nanocubes, i.e. oxygen atoms from PVP bind most strongly to the {100} facets, as a consequence metal atoms will be added more preferentially to {111} facets and afterwards these adatoms can then migrate to the face edges, resulting in an elongation of the {100} facets and the formation of nanocubes.[55] Electronegative ligands, such as Br^- and Cl^- can also work like capping agents, although their role on the surface is still elusive. Henglein have proposed that addition of a coordinating anionic ligand that strongly interacts with Ag can increase the reactivity of the metal.[56] It was speculated that for any Ag atom on the surface of a particle to bond with a ligand, it has to pass some negative charge to other Ag atoms on the surface. This increase of electronegativity on the surface would make it more reactive to processes such as oxidation.[56]

The reactivity of surfaces and their oxidation is another aspect that plays an important role in directing the growth of nanocrystals with different shapes. In this sense, the presence of structural defects on the crystals represents a highly reactive point, and thus can directly dictates the anisotropic growth of a crystal into a nanorod or nanowire.[50] However, from the basics it is known that fcc metals have a cubic crystal structure and there is no intrinsic driving force to grow one-dimensional structures such as nanowires. The only way to accomplish this is breaking the cubic symmetry of the lattice. In fact, during the nucleation stage not only single crystal seeds are formed, but also single and multiple twinned seeds containing at least one twin defect.[50,51] The twin defects are the most popular defects in nanocrystals and they are often observed for fcc structured metal nanocrystals. Twinning is the result of two subgrains sharing a common crystallographic plane, where the structure of one subgrain is the mirror reflection of the other by the twin plane. Another typical planar defect observed in fcc metals are the stacking faults. Stacking faults are formed by a distortion on the stacking sequence of atom planes. For example, the (111) plane stacking sequence of a fcc structure follows A-B-C-A-B-C-A-B-C-. If this stacking sequence is changed to A-B-C-A-B-A- B-C-, then a stacking fault is created. Both defects, twin and stacking faults, are generated probably due to the high strain energy in the volume.[51] Taking into account that among the fcc metals, Ag and Au have the lowest energy barrier for incorporating planar defects in their crystals, the presence of such defects can

introduce self-propagating ledges that can serve as active sites for crystal growth. This growth mechanism based on defects is also a key point to kinetically control the shapes of crystals. For instance, by keeping the rates of atomic addition slow, multiply twinned seeds can prevail over single-crystal ones because multiply twinned seeds can be kept at small sizes for a long period of time.[51,54] This slow addition of atoms tends to form nuclei and seeds through random hexagonal close packing presenting stacking faults. In this way, the seeds usually take a shape different from that favored by thermodynamics (i.e. higher energy structure), as a consequence plate-like seeds covered by {111} facets at the top and bottom surfaces and with defects (twins and stacking faults) in the vertical direction instead polyhedron seeds are formed. This mechanism of controlled addition of atoms during the reaction is also known as a kinetically controlled mean.[51] All of these concepts describe how a nanoparticle, nanorod or nanowire can grow based on the mechanism induced by the solution phase, the next Section will introduce the concepts about the electronic transport in such systems. The size and surface effects in the electronic conduction of metal nanowires and specially in those ultrathin nanostructures are expected to have a profound influence in their intrinsic properties.

2.4 Electrical Transport in Metal Nanowires

The electrical conduction in a metal wire is classically described by Ohm's law by considering the ratio between an electrical current (I) in the wire and a voltage (V) applied to produce it, Figure 2.5. This relation is then expressed by R = V/I, where R corresponds to the electrical resistance of the wire.

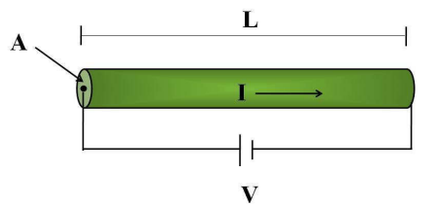

Figure 2.5. Illustration showing a macroscopic wire with a length L, a cross-sectional A and an electrical current I induced by a potential V.

Assuming that the wire presents a cylindrical shape having a length L and a cross-sectional area A, the resistivity (ρ_0) of this wire can then be expressed as:

$$\rho_0 = R\frac{A}{L} \qquad \text{(Eq. 2.5)}$$

For bulk Au, the typical resistivity measured is about 2.2 μΩ.cm.[57]

This electrical transport in metals is described by Landauer-Fermi theory (Figure 2.6), which states that in solids the outer shell electrons have a continuous range of energy levels (quantum bands). In metals, the highest-energy occupied state (valence band) and the lowest-energy empty state (conduction band) differ only infinitesimally in energy.[58] Thus, it means that electron states at energies slightly higher than the thermal energy κT (where κ is Boltzmann constant and T the absolute temperature) below the Fermi level (E_F) are almost fully occupied. The Pauli exclusion principle states that an electron can only be scattered into an empty state in the conduction band.[58] Excitation of deep electrons is highly suppressed by the scarcity of empty states, so that only electrons near the Fermi level undergo scattering. This situation is clearly understood under the action of an external field, where only the electron occupation near the Fermi level is altered. As a result, the density of states (DOS) near the Fermi level is the most

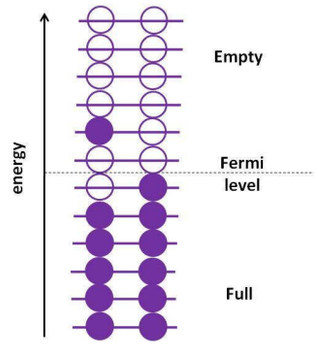

Figure 2.6. Schematic energy spectrum in a metal. Filled and empty circles represent full and empty quantum states, respectively, with two per level corresponding to the two spin orientations, just as in an atom.

important for the metal electrical properties, and only those electrons in a small range of energy around the Fermi level contribute in fact to the electrical conduction.[58]

In case of a metallic nanowire, the size effects play a critical rule in the electrical properties and the electrical resistance of the material can drastically change in comparison to that of bulk metal. For nanowires with lateral dimensions x and y having widths of L_x, $L_y < \lambda_{dB}$, where λ_{dB} corresponds to the electron wavelength (also termed de Broglie length), the carriers are confined into the x and y directions and the electron energy become quantized. In the perpendicular direction z, electrons travel as waves and the conductance (G) through the nanowire is given by:[59]

$$G = \frac{2e^2}{h} T_n \qquad \text{(Eq. 2.6)}$$

where e is the electron charge, h is Planck's constant and T_n is a transmission-probability function. For an ideal wire $T_n = 1$ and the term $2e^2 / h = 77{,}4\ \mu S$, which is called the quantum conductance. In this case, the transport of electrons along the wires is ballistic and the electron wave can travel through the wire without experiencing scattering that can change its momentum or phase. In the case of a nanowire with diameter larger than λ_{dB}, but smaller than the mean free path of conducting electrons, the transport through the nanowire is dominated by scattering. Scattering occurs due to the collision of the conducting electrons with vibrating lattice atoms (phonons), impurities and defects. In such a case the transport is said to be diffusive.[60] Surface scattering is the main effect observed in the electrical properties of those nanowires synthesized using the methods introduced in Section 2.3.

It was Fuchs and Sondheimer who first modeled (FS model) a kinetic theory to the electrical resistance of thin metallic films due to surface scattering, and later Chambers extended the FS model for general shape of conducting circular wires.[61-63] They showed that the electrical resistance of thin films with thickness comparable or smaller than the electron mean free path is much higher than in their bulk counter-part. Surface impurities or contaminations also strongly contribute to the increase in surface scattering, specially in nanowires because with the decrease of the diameter, the surface to volume ratio increases and more chemical contaminants can be adsorbed on their surface. The presence of adsorbates on the surface of nanowires can represent also an implication to the technological application of these nanomaterials as nanoelectronic

devices to be used either in interconnections or sensors. Based on this observation, the next sub-Section introduces the concept of electrons tunneling and the problem of surface contamination to the electronic transport between metal nanowires and metallic macroelectrodes.

2.4.1 Electrons Tunneling in Nanowire-Metal Junctions

Ultrathin metal nanowires are expected to present electronic transport based on the concepts of Landauer-Fermi theory. In this case, considering a nanowire-metal electrode junction, which is typically formed to electrically characterize these nanostructures, the electron transport between these two pieces of metal is based on the quantum phenomenon of tunneling.[59] For nanowires or metal electrodes having some adsorbated molecules or oxide in their surface, this junction can be described as a capacitor formed by two metals separated by a thin insulating layer, as illustrated in Figure 2.7. The process of tunneling in this case involves the application of a voltage between the electrodes, causing consequently an extension of the wave function of an

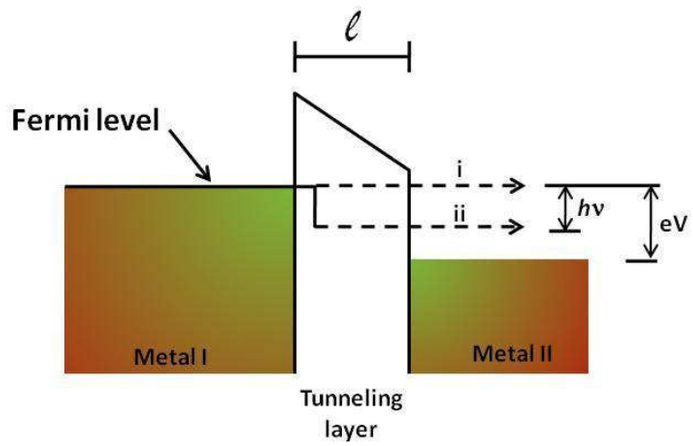

Figure 2.7. Schematic illustration of a Fermi level diagram for a metal-insulator-metal junction demonstrating elastic (i) and ineslatic (ii) tunneling. The inelastic current has a threshold voltage described by V = *h*ν/e.

electron from one metal into the insulating layer and overlapping the wave function of an electron from the other metal. The tunneling occurs due to the overlapping of the wave functions. This happens either without loss of energy (elastic tunneling) or with loss of energy to elementary excitations of the oxide or molecules adsorbed on the insulating layer (inelastic tunneling). For the case of inelastic tunneling, it occurs when $eV > h\nu$, where ν is vibrational frequency energy of an adsorbed molecule. The threshold voltage for such inelastic event is equal to $h\nu/e$. Thus, it means that there is a different threshold voltage for each vibrational mode of the molecule.[64]

The tunneling current has contributions from both elastic and inelastic processes and the threshold voltage can be identified by the onset of an inelastic tunneling that is observed when the conductance increases. In this manner, considering that in a junction nanowire-metal electrode the contact area is very small, the thickness and the dielectric constant of the insulating layer represent two main barriers for the tunneling, implying that the same junction can present different threshold voltages due to possible variations in the contact area.[64] These points should be considered when a nanowire-metal junction is electrically analyzed, specially in cases where it is exposed to liquid environments. The next Section will not focus on this, but on interfacial processes that develop on the surface of nanowires when they are exposed to aqueous solutions.

2.5 Nanowires in Solution

The last Section described how the electric transport of nanowires in air can be affected by scattering effects, specially by the adsorption of chemical species on their surface. This Section will give an overview of the interfacial processes when ultrathin nanowires are submerged in aqueous solutions containing ionic species. It is already known from the classical macroscopic electrodes that when they are immersed in a conducting medium, an electrochemical equilibrium is established on their surface. In the case of nanowires, it is the same but with a remarkable difference in the diffusional process on the surface of the wires. As the nanowires present a large surface and do not present a planar configuration, it is expected that a three-dimensional diffusion process of species occur. It implies that a much larger number of species are able to reach and adsorb on the surface of nanowires. This effect as well as the

charging and the formation of the electric double layer on the surface of nanowires will be presented in sequence.

2.5.1 Nanowires-Electrolyte Interface

From elementary electrostatics, it is known that when a metallic nanowire is immersed into a solution containing ionic species such as dissolved NaCl, an electrical double layer will be formed at the solid-liquid interface. Taking into account the double layer model proposed by Bockris, Devanathan and Müller, the molecules of the solvent, in this case water, strongly adsorb by dipole interactions on the nanowire surface.[65] This model, which is considered more complete shows the predominance of water molecules near to the nanowire/solution interface. Figure 2.8 shows an illustration of the respective model demonstrating the adsorption of water molecules on nanowire by electrostatic (dipole) interactions according to the charge on the surface of the nanowire.[65] Following the electrical double layer model, these adsorbed molecules constitute the first layer of the internal Helmholtz plane (IHP). The external one (OHP) refers to the adsorption of the solvated ions and the next respective layer is the diffusion layer.[66]

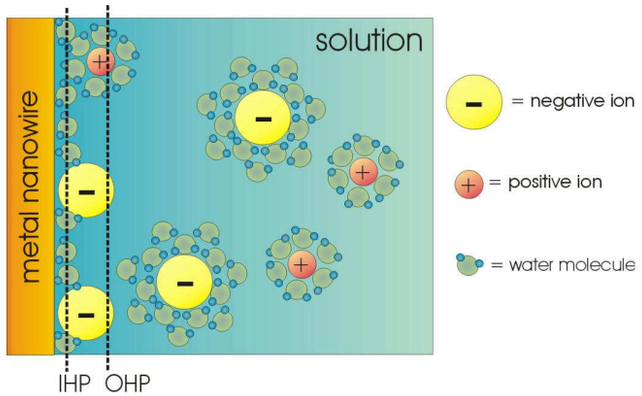

Figure 2.8. Schematic representation of Bockris Devanathan and Müller model for ions and water molecules distributed inside of the electrical double layer and adsorbed with oriented dipole on the surface of a nanowire. In the representation of water molecules the blue balls represent the hydrogen atoms, while the green balls are oxygen.

This ionic configuration with oriented dipoles on the interface resembles the structure of a simple capacitor. The capacitance C_{dl} in this case is determined by the dielectric permittivity of electrolyte ($\varepsilon_o\varepsilon_r$), the interfacial area (A_i), and the distance (d_{OHP}) of OHP from the nanowire surface

$$C_{dl} = \frac{\varepsilon_0 \varepsilon_r A_i}{d_{OHP}} \quad \text{(Eq. 2.7)}$$

where ε_o is the permittivity of free space (8.85419 x10^{-12} F/m) and ε_r is the relative permittivity of the electrolyte. The value of C_{dl} can provide an estimative of the outer capacitance in the electric double layer, although the values of ε_r and d_{OHP} can be very variable.

2.5.2 Debye-Hückel Theory and the Electrostatic Potential at the Nanowires

The electrostatic potential of an ion or charged molecule near the nanowire can be described by the Debye-Hückel theory, which provides a good approximation for such species in solution. In this model, the Debye length (λ_D), which characterizes the distance that significant charge separation can occur, is defined as:[67,68]

$$\lambda_D = \frac{1}{\sqrt{4\pi l_B \sum_i c_i z_i^2}} \quad \text{(Eq. 2.8)}$$

where l_B corresponds to the Bjerrum length (0.7 nm for water at room temperature) and $\sum_i c_i z_i^2$ is the sum over all ion species, with a concentration c_i and a valence state z_i. For salted solutions of binary monovalent ions such as NaCl, this last term is also referred as the ionic strength of the solution. In the Debye-Hückel relation, the potentials will exponentially decay with the decrease of the ionic strength due to the increase of the distance of charge separation and their screening from each other. Therefore, the estimation of λ_D provides an information of the potential gradient at the surface of a nanowire.[67,68]

It is worth pointing out that the capacitance C_{dl} is also dependent on the ionic strength. As the molar concentration increases, the Debye length decreases and cause a corresponding increase in the capacitance near to the solid surface (nanowire in this case). This effect is shown

in Figure 2.9 in combination with the effects of changing potential.[67] In case the nanowire is not polarized, the values of C_{IHP} and C_{OHP} will be the same. However, if a bias is applied to the nanowire, the capacitance C_{OHP} will decrease causing the overall capacitance to be dominated by C_{IHP}. Thus, the capacitance increases to a maximum dictated by C_{IHP}.

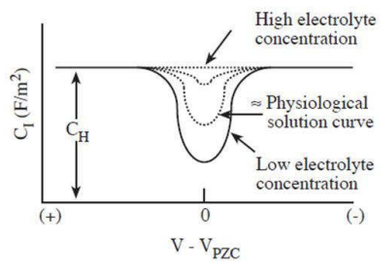

Figure 2.9. Representation of the changes on the interfacial capacitance with electrolyte concentration and potential. The Figure was adapted from [67].

In case of a Faradaic reaction occurs on the surface of nanowire, a thin depletion layer, which is a consequence of the finite rate which the reactant can be transported from the bulk to the nanowire surface, is established in the solution adjacent to the electrode surface. For ultrathin nanowires, the thickness of the depletion layer is comparable to the thickness of the electrical double layer. If a steady-state response is established, it is possible to express the depletion layer, δ, in terms of electrode radius (r_0), as shown in Equation 2.9.[69-72]

$$\delta = ar_0 \qquad \text{(Eq. 2.9)}$$

The term a is a numerical constant that depends on the relative contributions of migration and diffusion, which are predominant in this case. For a spherical nanoelectrode of a 10 nm radius immersed in a salted solution of NaCl 0.001 mol/L, the Debye length is about 10 nm and the spherically symmetric diffuse layer thickness is estimated as $1.5\lambda_D$.This distance from the electrode surface corresponds to the distance where the electrostatic potential decays to 10% of its surface value.[69] It means that in this case the depletion layer can be approximated as $\delta = 10r_o$

= 100 nm. For a macroscopic surface in the millimetric range immersed in a solution containing an excess of supporting electrolyte, the λ_D is just an insignificant fraction of δ, and the electric field within the double layer has a negligible effect on the transport of ions to the surface.[69,71]

However, for an ultrathin nanowire the electric field originating on its surface is expected to accelerate or retard the flux of ions.[69,73] For example, the migration current corresponding to the oxidation of a specie A^- at $r_0\lambda_D = 10$ in a reactant ion/supporting electrolyte ratio of 10^{-3} is about 20% larger than in a purely diffusion-controlled process.[69] This deviation is ascribed to electrostatic double layer forces acting on the reactant within the depletion layer. In fact, it reflects the relative dimensions of the double layer with respect to the depletion length, which in turn is determined by the electrode radius and the electrolyte concentration. When $\lambda_D << r_0$, the thickness of the double layer is insignificant compared to the thickness of the diffusion layer and reactants ions do not experience an electrostatic force until they are in the immediate vicinity of the electrode. On the other hand, if $\lambda_D >> r_0$, the thickness of the diffusion layer is significantly smaller than the thickness of the double layer and in this case the electric field can increase or decrease the transport limited current. It implies that diffusion and molecular transport within the double-layer region are significantly different from those of the bulk electrolyte.[69-72] In this case, the Debye length plays an important role because the dimensions of the nanowires are also comparable to that of charge separation within the double layer. Ogawa and co-workers showed that the electrical conduction in an electrode based on very small tin oxide particles is affected by the particles size and the Debye length.[74] The authors suggested that when the particle size (D) is comparable to the twice of Debye length, the width (L_c) of the channel where the carriers can move without any disturbance by surface charge becomes narrow as described in Equation 2.10.

$$L_c = D - 2\lambda_D \qquad \text{(Eq. 2.10)}$$

The surface scattering strongly influences the electronic transport and consequently the conductance of the nanomaterials. This effect is more remarkable when $D \approx 2\ \lambda_D$.

Such predictions and demonstrations of how capacitance develops at nanowire/electrolyte interface and how the resistance of a nanowire changes with its surface charging due to an applied potential suggest that ultrathin Au nanowires could be applied as sensors or biosensors.

Based on this concept, the next Section will introduce how nanowires could be used to sense the electrical activity of electrogenic cells, such as neuronal cells.

2.6 Coupling Metal Nanowire Devices with Biological Cells

Based on the idea that the surface charge due to ions adsorption on the surface of nanowires can cause change in the electrical resistance of the nanowires, this Section will describe how the electrical activity of neuronal cells could be monitored using ultrathin metal nanowires. In the first part, fundamentals about neurons and their electrical activity through action potentials will be introduced. In sequence, a model for signal transduction and detection will be discussed.

2.6.1 The Neuronal Cell

The neurons are considered the fundamental building blocks of the central nervous system (CNS), including the brain and the spinal cord. The human brain has about 100 billions of neurons that have as main functions the receiving and the transferring of electrical signals through ions and chemical molecular species, also called neurotransmitters. Thus, the neuronal activity is the primary functional output of the nervous system and deviations from its physiological level often result in adverse behavioral or physiological function.[75,76]

The neurons can present different shapes and sizes and are classified according to their morphology and function. Figure 2.10 illustrates different kinds of neurons found in different parts of the CNS as role of their activity in these areas. All neurons share common structural aspects such as axons, soma (cell body) and dendrites. The dendrites act as receptors of signals from thousands of other cells and transmit them to the soma, which is the main part of the cell containing the nucleus and is where the signal processing occurs, and then is forward along the axon that will transmit this signal through electrical or chemical synapses to other cells. The main mechanism for this signaling is based on the transport of ions such as Na^+, K^+, Cl^- and Ca^{2+} through the cell membrane.[75,76] The following section will present this mechanism with more details.

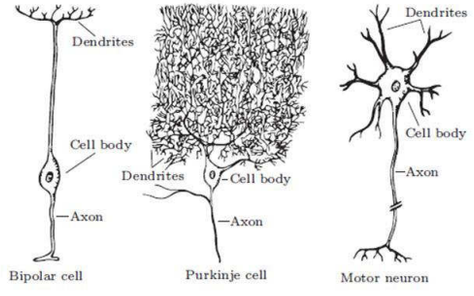

Figure 2.10. Illustration of three different kinds of neurons found in the CNS showing their different morphologies. The Figure was adapted from [75].

2.6.2 The Cell Membrane and the Ionic Transport

The cell membrane is the main component of a cell to keep different gradients of ions and molecules into and out of the cell. The cell membrane is basically constituted by phospholipid molecules which form a 4-10 nm thick lipid bilayer due to the hydrophobic interactions between the aliphatic and hydrophobic parts of the molecules.[75,76] A kind of transmembrane proteins that have a critical function in these cells are the voltage-dependent ion channel proteins. These transmembrane proteins are not exclusive of only neuronal cells, but have a critical function in these last ones. These ions channels are selective to the transport of ions such as Na^+, K^+, Ca^{2+} and Cl^- into and out of the cell. Their selectivity is based on the conformational configuration of the proteins that form the channels.[75] These molecular configurations exhibit variable pore sizes that are dependent on charge distribution in the molecular channels and that generate differentiation between ion polarities and sizes. By changing the electrical potential difference near these proteins they can adopt configurations that allow the ions transport through the cell membrane. This transport is purely passive over the concentration or the field gradient. Other membrane spanning proteins called *ion pumps* actively pump ions against their concentration gradient across the membrane. This transport mechanism is called active transport.[75,76]

When neurons are not transmitting signals they are said to be in their resting state exhibiting a constant electrical potential across their membrane. This resting potential has its origin in the different ion concentrations into and outside of the cell. These ions concentration for a mammalian neuron is showed in Table 2.1. It is interesting to note that in the resting state, most of K^+ channels are opened while Na^+ are closed, resulting in a high concentration of Na^+ ions out of the cell and a low concentration of these ions into of it. The inverse occurs for K^+ ions.

Table 2.1. Intra and extracellular ion gradient concentrations in a mammalian neuron.[76]

Specie	Intracellular Concentration (mmol L^{-1})	Extracellular Concentration (mmol L^{-1})
Na^+	15	150
K^+	150	5
Ca^{2+}	0.0001	2
Cl^-	10	120

This gradient of ions inside and outside of the cell leads to a difference of electric potential in the cell membrane. At equilibrium no ions are crossing the membrane and an equilibrium potential (E_i) that can be described by Nernst equation (Equation 2.11) is established.

$$E_i = \frac{RT}{z_i F} \, ln \frac{[i]_{in}}{[i]_{out}} \qquad \text{(Eq. 2.11)}$$

where R is the gas constant, T the temperature, z_i the valence of the ion, F the Faraday constant, and $[i]_{in/out}$ are the respective ion concentrations. Considering the values from Table 2.1 for a membrane only permeable to K^+ gives an equilibrium potential of -91.2 mV. The resting potential of neurons can vary between -40 and -100mV, because next to a large amount of opened K^+ channels some opened Na^+ and Cl^- channels also contribute to the potential difference.[77] A more accurate description of this voltage membrane was described by the model of Goldman-Hodgkin-Katz and is given by:

$$V_m = \frac{RT}{z_i F} \, ln \frac{P_K[K^+]_{in} + P_{Na}[Na^+]_{in} + P_{Cl}[Cl^-]_{in}}{P_K[K^+]_{out} + P_{Na}[Na^+]_{out} + P_{Cl}[Cl^-]_{out}} \qquad \text{(Eq. 2.12)}$$

in this case, *P* represents the permeability of the respective ions.[75]

In 1952, Hodgkin and Huxley introduced an electrical equivalent circuit of the cell membrane. This circuit, which is illustrated in Figure 2.11, describes the electrical behaviour of the membrane by voltage sources equal to the respective equilibrium potential E_i of the ion species and by resistors with a conductivity G_i proportional the respective ion permeabilities.[78,79]

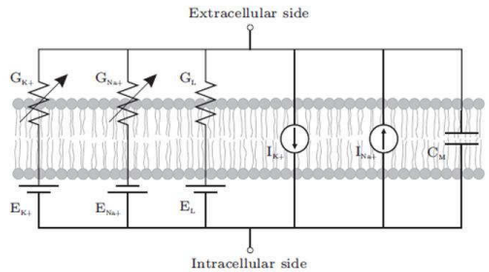

Figure 2.11. The equivalent electrical circuit for a membrane of a neuronal cell proposed by Hodgkin and Huxley. The Figure was adapted from [79].

The circuit also contains two current sources I_K^+ and I_{Na}^+ which model the ion pumps that can actively transport K^+ and Na^+ against their electrochemical gradient across the membrane. This equilibrates the different gradient of ion concentrations on either side of the membrane. The final element in the electrical circuit is the membrane capacitance C_M, which models the lipid bilayer. This bilayer is impermeable to ions but can nevertheless be charged and discharged just like a capacitor. The specific membrane capacitance usually presents values of 1 μF cm^{-2} and an artificial lipid bilayer without transmembrane proteins has a specific conductivity of about 10^{-8} S cm^{-2}. In a natural membrane with embedded proteins the specific conductivity can vary from 1 S cm^{-2} to 10^{-4} S cm^{-2}.[77]

2.6.3 The Action Potential

As mentioned before, the signal propagation in neuronal cells is driven by an influx and an efflux of ions through the cell membrane. This process, which is trigged by a threshold voltage is also called action potential (AP). The electric pulses generated by APs travel like a

wave along the cell membrane.[77,80] Above the threshold voltage the cell membrane is said to be depolarized and voltage-gated sodium and potassium channels are opened. Figure 2.12 depicts an example of an action potential correspondent to Na^+ and K^+ ions conductance changes.

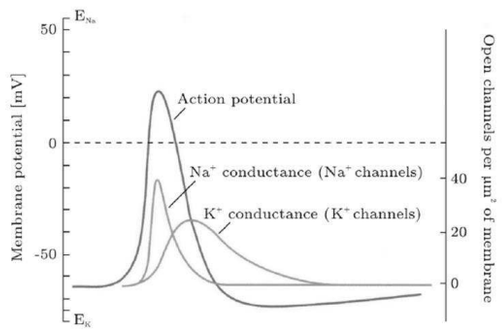

Figure 2.12. Representation of the voltage trace over the time of an action potential and the correspondent Na^+ and K^+ ions permeabilities. The scale in the right side represents the number of ion channels opened. The Figure was adapted from [75].

As demonstrated, the fast Na^+ channels open first, allowing Na^+ ions to flow into the cell, thereby driving the membrane potential towards the equilibrium potential of Na^+ (+ 61.6 mV). This potential is not quite reached because the slow K^+ channels open delayed, enabling K^+ ions to flow out of the cell. The closing Na^+ channels are inactivated until the cell reaches its resting potential again. This refractory period limits the frequency at which action potentials can be generated. The K^+ channels stay opened even after the resting potential is reached, forcing the cell to enter in a hyperpolarisation state where the membrane potential is more negative than the resting potential. Finally, in a last step the voltage gated K^+ channels close and the resting potential is re-established. The generation of an action potential follows the principle that once a stimulus surpasses the threshold voltage and the cell is not in its refractory period, an action potential will be generated. Stronger stimuli result in several action potentials being emitted in a row.[75,77,80]

2.6.4 Signal Transduction

In Section 2.5, it was introduced the basic concepts about the interface electrode/electrolyte and the how the effects of the electrical double layer can change the capacitance and the resistance of a nanoelectrode. These concepts can be applied to determine how a biological signal would be transduced into an electrical signal that can be amplified and processed by external circuitry. Although several models have been used to describe the cell/electrode interface, the interpretation of the measured signals is still one of the main challenges. Some factors that strongly contribute to the signal shape are the extracellular tonicity, the electrode geometry, the coupling of the cell to the electrode as discussed in the previous section and perhaps others. Apart of these, there are generalities that can be considered about the shape of the signal and additionally, there are different ways of visualizing the transduction process as it will be discussed in sequence.

2.6.5 The Moving Dipole Model

When an action potential is fired, it travels along a cell membrane and induces different regions of the membrane to carry different transmembrane potentials. It is based on this phenomenon that the action potential propagates. Thus, it means that some regions of the membrane must have a negative transmembrane potential, whereas other exhibit a positive transmembrane potential. This charge distribution can be described as a moving dipole model. As this dipole moves past the electrode, the charge movement induced across the interfacial capacitance will cause the potential at the amplifier to first fall, then rise and fall again as depicted in Figure 2.13. This is what is observed in electrocardiograms and is also the case for extracellular recordings where the action potential propagates along a cell and/or along a sheet of cells.[81]

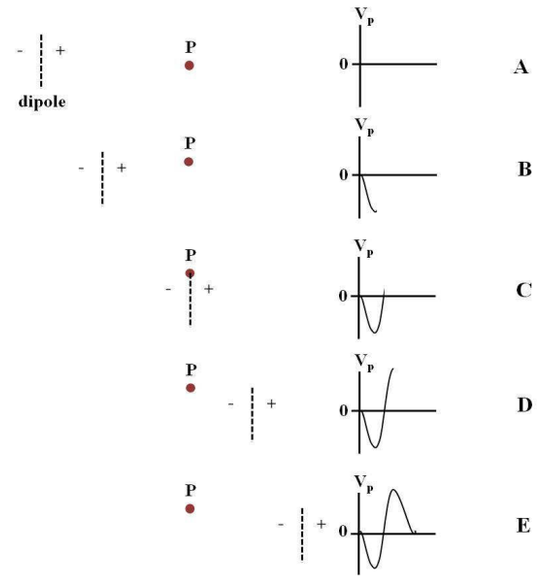

Figure 2.13. Schematic illustration of a dipole moving over an electrode at point P (from A to E). The charging of the dipole leads to a mirror charge at the electrode. As the dipole moves over the electrode, the polarity of the image charge changes and results in a signal with shape characteristic of an extracellular AP. The Figure was adapted from [81].

2.6.6 Traveling Waves and Seal Resistance

The cell/solid substrate interface can be well described by the point contact model (Figure 2.14).[82,83] Following this model, the separation between the cell and the substrate is filled with electrolyte and exhibits a resistance, which is also known as a seal resistance (R_J). All basal membrane currents (those flowing through the bottom membrane of the cell) associated with a traveling wave must flow through this seal resistance. This, results in a voltage drop between the electrode and the electrolyte bathing the cell, which can be monitored using an underneath electrode. The current flowing through the basal membrane is the sum of the ionic and capacitive

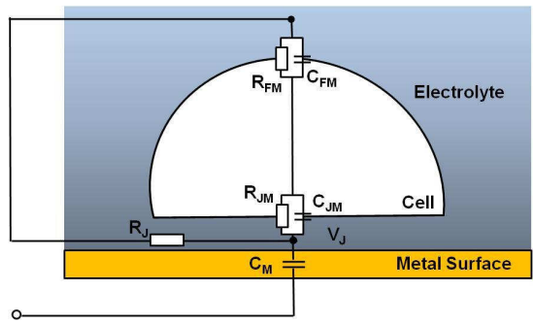

Figure 2.14. Representation of the cell/metal surface junction showing the circuitry elements described by the point contact model. The terms C_M, R_J and V_J correspond to the capacitance of the metal, the seal resistance and the voltage developed in the junction cell/metal surface, respectively. The other circuitry elements, R_{JM}, C_{JM}, R_{FM} and R_{FM}, are the resistance and the capacitance of the membrane in the junction and the free part of the membrane exposed to the electrolyte solution, respectively.

currents. As this current flows through the seal resistance, a voltage (V_J), which is proportional to the second derivative of the transmembrane potential is developed in the junction cell/substrate. This voltage is also proportional to the magnitude of seal resistance and a near linear correlation can be observed.[84] In the extreme of an infinite seal resistance, this voltage in the junction would correspond to the intracellular potential, thereby simulating whole-cell patch configuration. This direct correlation has since long been already demonstrated experimentally and through simulation.[85,86]

2.6.7 Electrode Transduction

The voltage signal V_J is then transduced by the electrode according to the model described herein. That is, the electrode detects the local variations of the electrical potential due to the movement of ions into the cleft between the cell and the electrode. For most practical

systems in the bandwidth of interest, the electrode is mostly capacitive. Additionally, apart from the noise and consequent signal attenuation, the seal resistance is correlated with the basic configuration of the electrode and it has a direct influence in the recorded extracellular signal strength. For instance, Lind and co-workers were one of the first to model the extracellular signal strength for a spherical cell surrounded by extracellular fluid, a cell above an extracellular electrode, a cell above an electrode in a groove, and a cell above an electrode in a cubic pit where the groove and pit dimensions were slightly larger than the cell.[87] The resulting extracellular voltages calculated were 142 µV, 168 µV, 391 µV, and 1.2 mV, respectively. Thus, a significant improvement was predicted by confining the space around the cell. While these simple considerations are only guidelines, they can provide the insight required for interpreting biological signals recorded using ultrathin Au nanowires as metal electrodes.

2.7 Characterization Techniques: Electron Microscope

During the experimental work of this thesis, transmission electron microscopy technique was employed to characterize the structure of ultrathin Au nanowires. This Section will briefly describe the working principle of this microscope.

2.7.1 Transmission Electron Microscopy

The transmission electron microscope (TEM) is a powerful tool for investigating the crystallographic structure of materials, providing real space images on the atom distribution and reciprocal lattice information in a crystal and on its surface. Additionally, TEM is a versatile tool that provides not only atomic resolution lattice images, but also chemical information at a spatial resolution of 1 nm or better, thus, enabling the direct chemical identification of a single nanocrystal.[88] The basic principle of a TEM is straightforward and it starts with an electron beam illuminating an object, which should be thin enough to be transparent for electrons. High-resolution work on an atomic scale requires an object with a thickness of less than 10 nm. Inside the object, the electrons interact with the atomic scattering potential and thus carry information about the atomic structure of the object. After the transition of the object, the electrons are

guided by electron-optical lens system in order to form a strongly magnified image. Thereby the information about the traversed three dimensional object structure is transferred into a two-dimensional image. Figure 2.15 shows a schematic illustration of an electron-optical transfer in a common TEM. The details of the ray-optical diagram are described in sequence:[88]

- The illumination system is the uppermost element inside the column of the electron microscope. The most used electron sources are the lanthanum hexaboride (LaB_6) coated cathode of needle-like shape and field emission gun (FEG). Field emission systems have higher coherence lattice imaging, electron holography and higher spatial resolution microanalysis.

- After emission, the electrons pass the electron gun for acceleration. A high tension between 200 to 400 kV accelerates the electrons emitted from the source cathode. The magnitude of the accelerating voltage is a compromise between higher resolution and increasing radiation damage to the object.

- The condenser lenses and the condenser aperture are used to ensure a bright and parallel illumination of the object by the electron beam.

- In about half-height of the microscope column is the object holder. It provides control of the object in three dimensions and a tilt around two perpendicular axes. The incident electrons interact with the atomic scattering potentials inside the object.

- The most crucial component of the microscope is the objective lens. Due to the very short focal length of around 1–2 mm, it requires high currents of several ampere flowing through the lens coils.

- The selected area aperture is used in diffraction mode to select the area of the object that contributes to the diffraction pattern.

- Through the intermediate lenses the first intermediate image or the first diffraction image is post-magnified. A further magnified image is generated by the projector lens.

- The chemical analysis system is composed by the energy dispersive x-ray spectroscopy (EDS) and an electron energy-loss spectroscopy (EELS) system. While the first one can be used to quantify the chemical composition of the specimen, the EELS system can provide information about the electronic structure of the specimen.

- Finally, the data recording system tends to be digital with the use of a charged coupled device (CCD), allowing quantitative data processing and quantification.

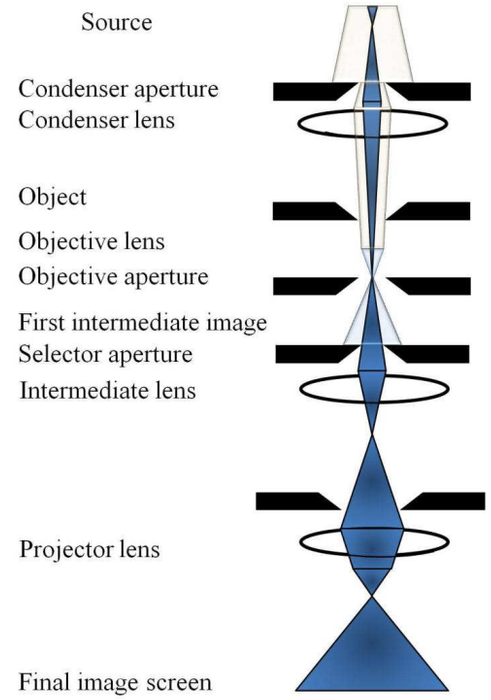

Figure 2.15. Ray-optical diagram for the transmission imaging mode of a typical TEM. The Figure was modified from [88].

Considering a metal with a face-centered cubic (fcc) structure as that demonstrated in Figure 2.16A, if the sample is oriented when the electron beam of TEM is in parallel with one of its crystallographic directions, then the obtained image should be a bidimensional projection of the atomic arrangement along that direction. Figures 2.16B–D show the expected image when the fcc structure is observed along [100], [110] and [111] directions, respectively.

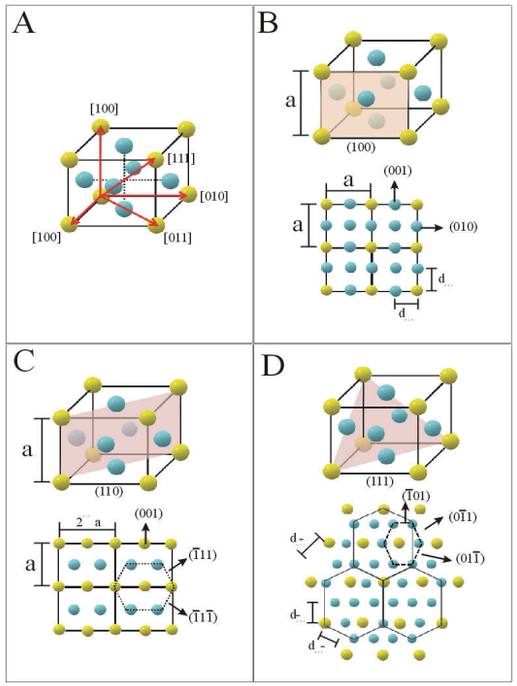

Figure 2.16. Illustration of the expected images of a fcc crystal (**A**), when observed using a HRTEM along (**B**) [100] direction, (**C**) [110] direction and (**D**) [111] direction. The yellow balls represent the Au atoms in the corner of the crystallographic structure, while the blue balls are the Au atoms in the face of the crystal.

Initially, it is possible to determine the observation axis following the observed pattern, that is, if it is oriented along [100] direction a square should be seen, in case of [110] a hexagone and if along [111] direction a perfect hexagone should be observed. The observed points in Figure 2.16 belong also to the crystalline planes, thus, not only the angles, but also the distance of the interplans should agree with the expected values of the material analyzed. From the images it is also possible to determine the crystalline directions in the plane of the specimen, i.e. it is possible to determine the direction that the nanowire is formed. It is worth also to mention that the resolution limit of TEM is about 0.1 nm, which is comparable to the distance between the

crystalline planes and thus, it represents an important limitation for the measurements. For instance, considering the case of Au for Figure 2.16D, where the atomic image is projected along [111] direction that is formed by (220) plans that have an interplane distance of 0.14 nm. If the resolution of the used TEM is > 0.14 nm, a few contrast only will be observed. The results and discussion of TEM and HRTEM analysis for Au nanoparticles and nanowires are given in Section 4.3.

2.8 Objectives of the Present Work

Based on the concepts and fundamentals presented in the previous Sections, the main aims of this thesis were:

- Synthesize ultrathin Au nanowires employing a wet chemical synthesis previously described in literature, and improve its understanding envisaging to explore the limits that the synthesis can provide to produce such ultrathin nanowires with high aspect ratio.

- Characterize the electrical properties of Au nanowires in air at room temperature and at low temperature to investigate possible quantum phenomenon in the electrical transport.

- Modify the surface of nanowires with alkanethiol molecules having different functional groups and characterize the electric transport of these modified nanowires in solution, focusing their application for sensors.

- Fabricate resistors based on ultrathin Au nanowires devices, and apply such devices to stimuli and sensing ion currents from action potentials in neuronal cells.

Chapter 3

Experimental Methods and Procedures

As discussed in the Fundamentals, the synthesis of ultrathin Au nanowires was first reported by Halder and Ravishankar,[7] the ultrathin nanowires investigated in this thesis were produced following a similar methodology employed by those scientists, but with slight modifications during the synthesis. Thus, the chemical synthesis of ultrathin Au nanowires and the techniques to structurally and electrically characterize these nanomaterials will be described in this chapter. Section 3.1 describes the chemical synthesis of nanowires, Section 3.2 describes how the morphology and the structural characterization of nanowires was performed using transmission electron microscopy. Section 3.3 details the assembly of Au nanowires on solid surfaces and over metal electrodes produced by lithography. Additionally, it describes the electrical characterization of nanowires by the two probe method at room and at cryogenic temperatures. Surface modification of nanowires with alkanethiol molecules and their electrical characterization in solution are reported in Section 3.5. Finally, Section 3.6 describes the experiments with Au nanowires to sense the electrical activity of neuronal cells.

3.1 Chemical Synthesis of Ultrathin Au Nanowires

For the synthesis, all chemicals were used as received. AuCl (99.9%), oleylamine (technical grade, 70%), hexane and absolute ethanol were obtained from Sigma-Aldrich. The Au nanowires were synthesized by dissolving 7.4 mg of AuCl in 10 mL of oleylamine and 1 mL of hexane (final AuCl concentration ~ 3 mmol L^{-1}). The solution had a light yellow color, typical of Au(I) compounds. Thereafter, the reaction was left undisturbed at room temperature for 24 h. After that, the solution was heated to 80 ^{o}C for 6 h. The Au nanowires were precipitated out by adding ethanol and centrifugation (12000 rpm for 20 min). The yield of the reaction, i.e. the production of nanowires, was determined through gravimetric analysis by weighting the dark

precipitated obtained in the end of the reaction. The nanowires were dispersed in hexane and this solution was stored in the fridge at 3 °C. The solution containing the nanowires is stable for at least one year.

3.1.1 X-ray Analysis of Intermediate Products Formed during the Reaction

While the reaction was left undisturbed for 24 h, a whitish gel was formed into the flask of the reaction. In order to analyze this gel, x-ray measurements were performed. In doing so, after the period of 24 h when the whitish product was formed, 5 mL of acetone were added to the solution to precipitate it. The supernatant of the reaction was removed and the x-ray analysis of the precipitated product was then carried out in a transmission mode employing a STOE Stadi P instrument equipped with a Cu K_α radiation source and image plate detector. As a control sample, an aliquot of oleylamine only that was separated from the solvent using the same methodology was also analyzed.

3.1.2 Differential Scanning Calorimetry Analysis of Intermediate Products

The separated whitish gel was also analyzed by differential scanning calorimetry (DSC). In this case, a Perkin Elmer Pyris Diamond DSC instrument with a power compensation-type DSC was used. This configuration allowed the heat flow difference required to heat the sample and a reference pan (empty aluminum pan) at a certain rate be measured. The DSC measurements were carried out in a scan rate of 5 $^{\circ}$C/min.

3.1.3 Chemical Synthesis of Cu and Ag Nanostructures

The same methodology employed in the synthesis of Au nanowires was also used for investigating the synthesis of Cu and Ag nanostructures. In this case, anhydrous $CuCl_2$ (99,995%) and $AgNO_3$ (99,0%), both purchased from Sigma-Aldrich were used as metal precursors. For the reaction involving $CuCl_2$, 4.03 mg of the salt was dissolved in 10 mL of

oleylamine and 1 mL of hexane (final $CuCl_2$ concentration ~ 3 mmol L^{-1}) using ultra-sound for about 15 min. The same procedure was applied for the reaction involving $AgNO_3$, but in this case 1.69 mg of the salt was dissolved with the help of ultra-sound for 15 min in 10 mL of oleylamine and 1 mL of hexane. The final concentration of $AgNO_3$ was ~ 1 mmol L^{-1}. This slight lower concentration in comparison to that used for AuCl and $CuCl_2$ was due to the low solubility of $AgNO_3$ in oleylamine and hexane. Both reactions were left undisturbed for 24 h and after that period they were heated to 80 °C for 6 h. Afterwards, the products of the reactions were precipitated out by adding ethanol and centrifugation (12000 rpm for 20 min) and finally, were analyzed using transmission and scanning electron microscopy.

3.1.4 Analysis of Chemical Complex formed During the Reaction

In this section, we will describe the preparation of Au nanoparticles and the techniques employed to analyze the complexation processes during their synthesis. Briefly, the nanoparticles were typically synthesized by dissolving 0.05 g of AuCl in a mixed solution composed of 2 mL of oleylamine and 2 mL of hexane. Afterwards, in order to speed up the reaction this solution was added to a glass containing 18 mL of oleylamine at 80 ^oC and the mixture was left undisturbed for 5 h. The AuNPs were precipitated out by adding acetone and centrifugation. Sequentially, the nanoparticles were washed several times with ethanol and then redispersed in hexane. TEM analysis of particles was carried out as described in Section 3.2. The equilibrium constants were determined by UV-visible measurements of the complex using a Perkin-Elmer Lambda 900 instrument. The analysis was performed for different concentrations of AuCl dissolved in oleylamine. The UV-visible spectra were obtained directly after the preparation of the solutions. Fourier transform infrared spectroscopy (FTIR) spectra were recorded using a Perkin Elmer spectrometer. Mass spectroscopy (MS) analysis was carried out in a ThermoScientific LTQ FT MS instrument operating in a positive mode.

3.1.5 Synthesis of Au Nanowires Bubbling Oxygen into the Reaction

In the Section 3.1, it was described the chemical synthesis of ultrathin Au nanowires in air, in this Section, the experimental details for the synthesis of nanowires in air, under N_2 (99.8% from Praxair) atmosphere and under saturation of the solution with O_2 (99.998% from Praxair) were the same as that described in Section 3.1. In the case of saturation of the solution with O_2, the pressure of the O_2 valve was set to 1.7 bar. For the synthesis of Au nanostructures in the absence of halides, Au_2S (99.9% from Sigma–Aldrich) was used as a precursor. In this case, for the reaction with Au_2S under N_2 and in air, the solid (14.8 mg) was dissolved in oleylamine (10 mL) and hexane (1 mL; final Au_2S concentration ≈ 3 mmol L^{-1}). The solution had a dark color and was not stirred for 24 h. At that moment, no whitish gel was observed in the bottom of the flask. After 24 h, the solution was heated to 80 °C for 6 h. The produced nanostructures were precipitated out by adding ethanol and centrifugation (12 000 rpm for 20 min) and afterwards, redispersed in hexane and analyzed by TEM.

3.2 Morphology and Structural Characterization of Au Nanowires

The morphology and the structural characterization of the Au nanowires were carried out with a TEM FEI CM20 and an FEI Technai F20 transmission electron microscope, both operated at 200 kV, by drop casting the product dispersions on copper grids coated with carbon film. High resolution transmission electron microscopy (HRTEM) experiments were also performed with an FEI Titan 80-300 transmission electron microscope equipped with a spherical-aberration corrector unit for the objective lens. We employed negative spherical aberration imaging (NCSI), providing bright atom contrast up to the information limit of 0.08 nm.[89,90] Additional microstructural analyses were performed using an FEI Technai F20 transmission electron microscope. For experiments involving the use of graphene sheets, the sheets were purchased from Plano GmbH and the specimens were prepared by drop casting the solution of nanowires over the graphene support.

3.3 Assembly and Electrical Characterization

The following sections will describe how ultrathin Au nanowires were assembled over metal electrodes and how their electrical characterization was performed at room and at cryogenic temperatures.

3.3.1 Device Fabrication for Electric Characterization of Nanowires in Air

In order to characterize the electrical properties of Au nanowires, they have to be connected to leads produced over a solid platform. To address this issue, firstly we fabricated Au leads over a silicon/silicon oxide substrate (Si/SiO_2). The details of the fabrication process are described in sequence, while the basic fabrication steps are illustrated in Figure 3.1. The whole procedure described in Figure 3.1 was performed in the cleanroom facilities of the Peter Grünberg Institut (PGI-8) at the Forschungszentrum Jülich GmbH. Initially, a p-doped (resistivity > 3000 Ω.cm) silicon wafer <100> of 4 inches in size (Figure 3.1 (i)) was thermally oxidized to produce a 400 nm oxide layer on the top (Figure 3.1 (ii)). In sequence, a layer of poly(methyl methacrylate - methacrylate) 33% (PMMA-MA 33%), which is an electron resist, was spun at 4000 rpm on the substrate. At this rotation a PMMA-MA layer of 480 nm was produced. The electron resist was then pre-baked for 15 min. Afterwards, PMMA 50 K was spun at 4000 rpm over this surface. The thickness of this new PMMA layer was 8 nm and the sample was pre-baked for 15 min. again right after the deposition process. The lanes to deposit the metal leads and the contact pads were patterned by electron-beam lithography (EBL) applying a doses of 470 $\mu C/cm^2$, Figures 3.1 iii and iv. The development of the electron resist was carried out for 1 min. using the PMMA developer 600-55 K, followed by submersion of the sample in iso-propanol for 30 s and drying sequentially in nitrogen (N_2). Afterwards, an adhesion layer of 10 nm of titanium followed by a thicker layer of 50 nm of Au was deposited by electron beam evaporation over the substrate (Figure 3.1 (v)). Employing a liftoff process, the Au leads and the contact pads were then formed in the defined areas (Figure 3.1 (vi)). Figure 3.2 shows different magnification of the designed pattern used to write the leads with EBL. The leads present a

width of 300 nm and were separated in three groups of 20 electrodes. The distances between the leads in each group were 5 μm, 1 μm and 500 nm.

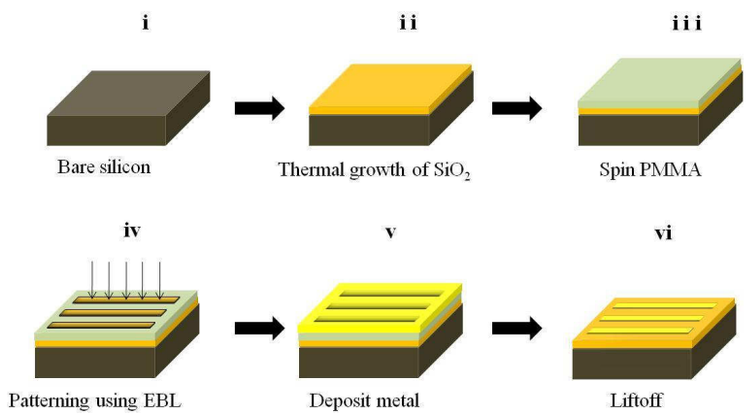

Figure 3.1. Schematic of the fabrication process of metal leads in a Si/SiO_2 substrate, including: the thermal oxidation of the bare silicon substrate (i and ii); the deposition and the patterning of PMMA by EBL (iii and iv); the deposition of Au and the liftoff process to remove the layer of PMMA and form the metal leads (v and vi).

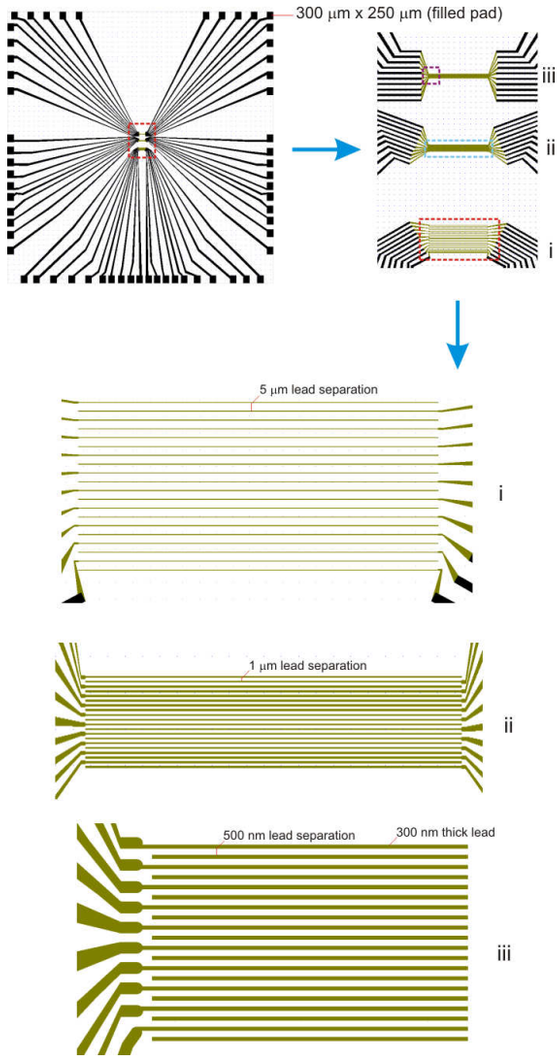

Figure 3.2. Mask design pattern for EBL. Each panel following the arrow corresponds to a zoomed image from the rectangular region in the previous panel. i, ii and iii indicate the different electrode configuration (separation between the leads) on the chip.

3.3.2 Assembly of Au Nanowires

To perform the electrical characterization of nanowires they had to be assembled over at least two leads. To accomplish this, we employed the solution of Au nanowires dispersed in hexane and exposed it to ultra-sound for about 10-15 s. The ultra-sound produces microscopic bubbles that collapse and generate shock waves that help the nanowires to disperse in the solvent. Afterwards, the nanowires assembly was carried out by flowing ~ 20 µL of the ultra-sonicated solution inside of a poly(dimethylsiloxane) (PDMS) microfluidic channel that was previously aligned over the metal leads. The details of the fabrication process of this microfluidic channel are described in Appendix A. Although the solution of nanowires was applied to the microfluidic channel through a manual micropipette instead to use an external pump, the flow rate inside of the channel was reliably controlled in ~ 10 mm/s. The simplest way to empty the PDMS channel was to wait the evaporation of the hexane solvent, which in this case took only around 30 s due to the high vapor pressure (151.3 mmHg at 25 °C) of this solvent. This approach to assembly the ultrathin Au nanowires over a solid platform is relatively simple and as the PDMS mold is not covalently sealed through -O-Si-O- bonds on the substrate, it allows the microfluidic channel to be removed after each set of experiments and reused for other substrates. To visualize the assembled nanowires, we analyzed the samples using a field-emission scanning electron microscope (SEM) JEOL JSM 6330F.

3.3.3 Current–Voltage Measurements at Room Temperature

The electrical characterization of the assembled nanowires was carried out employing a Keithly semiconductor analyzer (model 4200 SCS). The leads were electrically contacted through the bond pads using tungsten needles. The main electrical characterization was based in a two-point probe measurement, where DC voltages were applied and the resulting current was measured, i.e. current-voltage (I–V) measurements (DC bias). The resistance of the nanowires was then calculated from the I–V curves.

3.3.4 Electrical Measurements at Cryogenic Temperatures

The electric characterization of nanowire devices at cryogenic temperatures was also performed using a two probe method employing a Keithely 2400 DC mode. Figure 3.3 demonstrates a schematic illustration of how the measurements were carried out. The principle to reach cryogenic temperatures was described in ref [91] and it is briefly summarized here. Initially, the pad contacts of the samples were wire bonded directly to the cold finger of an insert (**1**), which is immersed in a liquid helium (^{4}He) bath (**2**) at approximately 4.2 K. The insert (**1**) contains inter alia, a ^{3}He pot (**3**) containing liquid ^{3}He (**4**) in use and, a ^{3}He filling/pumping tube (**5**) which is filled via a ^{3}He filling tube (**6**) connected to a ^{3}He storage dump via a suitable valve. The liquid helium bath (**2**) is mounted in a suitable cryostat. A sample (**7**) was mounted in vacuum on the base of the ^{3}He pot (**3**). A ^{4}He "1 K pot" (**8**) was mounted to the ^{3}He tube (**5**) such that it conducted heat away from the walls of the tube (**5**) in the positions indicated at (**9**). The vapor of liquid ^{4}He (**10**) in the 1 K pot was pumped to a low pressure by a rotary pump attached to exhaust tube (**13**) to reduce its temperature. The 1 K pot (**8**) was filled continuously through the variable flow needle valve (**12**), set for the required flow rate. By pumping off the ^{4}He vapor above the liquid ^{4}He (**10**), the temperature of the liquid He (**10**) is reduced to 1-2 K. The insert (**1**) also contains a sorption pump (**14**). When this sorption pump was cooled it pumped (i.e. adsorbs) the gas to a pressure dependent upon the temperature. A very high (and clean) vacuum could be achieved by this type of pump. The sorb (**14**) was cooled by a heat exchanger (**15**) which was fed with ^{4}He from the helium bath (**2**) via inlet tube (**16**) and a needle valve (**17**). The ^{4}He flows through the heat exchanger (**15**) controlled by valve (**17**) and exited via exhaust tube (**18**). When the sample (**7**) has been mounted and the insert (**1**) has been cooled to approximately 4.2 K, the 1 K pot (**8**) was pumped and the needle valve (**12**) was opened slightly to allow liquid helium to flow into the pot (**8**), cooling it to below 1.5 K. The sorb (**14**) was warmed above 40 K by the heater so that it will not adsorb ^{3}He gas (or will release adsorbed gas). The ^{3}He gas was free to condense on the 1 K pot assembly (**8**) and runs down to cool the ^{3}He pot (**3**) and sample (**7**). After a certain time, most of the ^{3}He gas should have condensed to give liquid ^{3}He (**10**) in the ^{3}He pot (**3**). At this stage the ^{3}He pot (**3**) is nearly full of liquid ^{3}He at approximately 1.5 K. The sorb (**14**) was then cooled, and it began to reduce the vapour pressure of the liquid ^{3}He (**10**)

so that the sample temperature dropped.[91] In our case, the lowest temperature reached was 500 mK. To heat the sample, a temperature controller lake shore 320 was employed, and to reach room temperature liquid helium was replaced by liquid nitrogen.

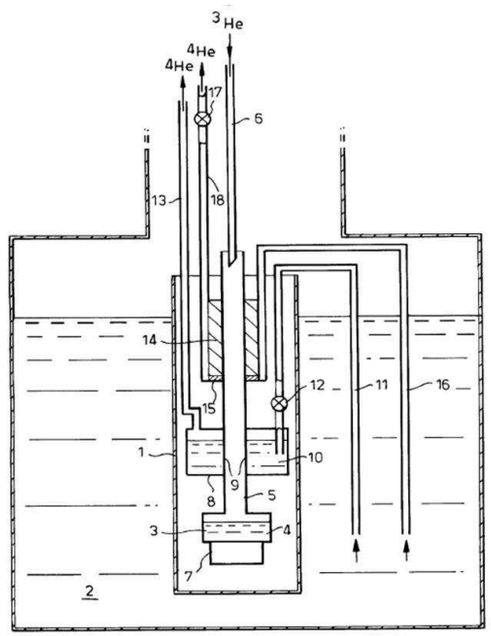

Figure 3.3. Schematic illustration of a helium refrigerator used to perform electrical characterization of nanowires at cryogenic temperatures. The description of each term and piece is given in text above. The Figure was adapted from ref. [91].

3.4 Device Preparation for Electric Measurements of Nanowires in Solution

For electrical characterization of Au nanowire devices in solution, the contact areas where the nanowires were assembled over the electrodes had to be passivated. The next Section describes how passivated Au nanowire devices were fabricated.

3.4.1 Fabrication of Passivated Au Nanowire Devices

The fabrication of passivated Au nanowire devices was performed in a similar manner of those devices not passivated, however, in this case, electrodes with a different configuration were fabricated. This fabrication process is described in sequence. Briefly, the photoresist AZ 5214 was spun at 4000 rpm over silicon substrates with 400 nm thermal SiO_2 on the surface. Sequentially, a photolithography step where the substrates were exposed to the UV-vis light (365 nm) for 6 s was performed. Afterwards, a post-bake process at 130 °C for 75 s, followed by the development of the photoresist for 50 s in the metal-ion-free 326 (MIF 326) solution was carried out and opened the lanes to deposit the metal leads and the contact pads. The devices were then fabricated by depositing by electron beam evaporation 10 nm of Ti and 50 nm of Au and sequentially performing a liftoff process in acetone to remove the photoresist. Figure 3.4 shows the design of the mask used in the photolithographic process.

The nanowires were then assembled over the leads employing the microfluidic approach described in Section 3.3.2. It is worth mentioning that although the use of this methodology does not allow an alignment of nanowires at specific positions, it is not critical because more concentrated solutions of nanowires can be used and thus, the probability of assembling nanowires between a pair of leads is higher. In fact, using a 1 mg/mL solution of Au nanowires dispersed in hexane, it was possible to assembly nanowires in more than 25 out of 30 pair of leads, as verified through SEM analysis. Another important detail in this approach is the configuration to have the nanowires on top of the leads instead to have the leads on top of the nanowires, as it is usually employed with other kinds of nanowires or nanotubes. Specifically, in this case it was used this configuration due to the thermal instability and melting of nanowires at temperatures higher than 100 °C. As during the lithographic process to fabricate the leads the

photoresist has to be post-baked at temperatures higher than 120 °C, the approach to have the leads on top of nanowires was avoided.

In order to check the electrical resistance of the assembled nanowires, I–V characterization for each nanowire or ropes (bundles) of nanowires was carried out before the next step. This characterization was important because it provided a prior information about the number of devices that were working properly.

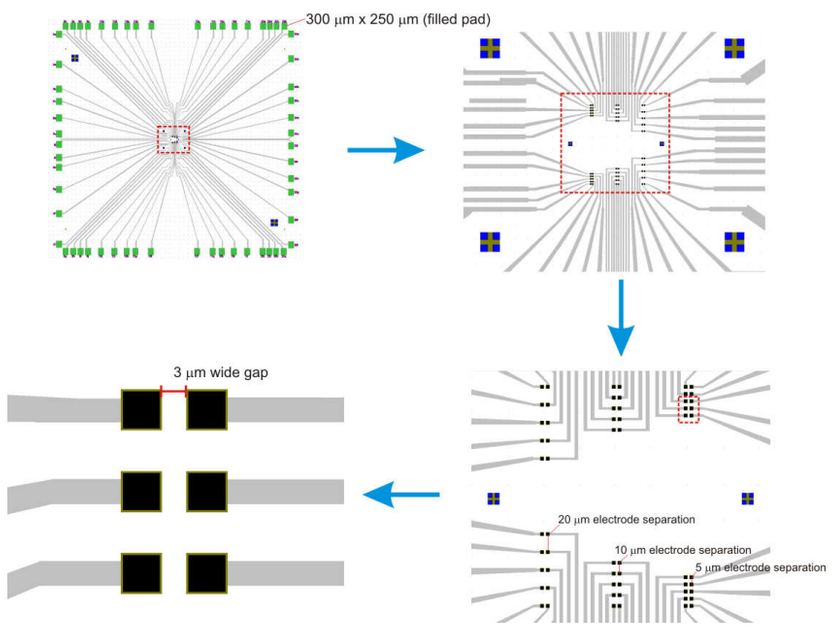

Figure 3.4. Different magnifications of the mask design pattern for fabricating the Au nanowire devices. Each panel following the arrow corresponds to a zoomed image from the rectangular region in the previous panel.

Afterwards, the passivation of the metallic leads was performed by covering the whole surface with a layer of about 220 nm of PMMA 600 K, which was spun at 4000 rpm, whereas the areas of the contact pads and between the pair of leads containing the nanowires were

sequentially patterned by electron-beam lithography using a doses of 300 μC/cm^2. The development and the removal of PMMA from this patterned areas was performed as described in Section 3.3.1 and generated channels (grooves) between the pair of leads, leaving the surface of the assembled nanowires exposed to the environment. Additionally, the removal of PMMA from the contact pads allowed them to be electrically contacted from external sources. Figures 3.5A and B show optical images of the leads passivated with PMMA and the formed grooves between the pair of leads. Figures 3.5C and D show two micrographs of the passivated devices containing the Au nanowires between the leads.

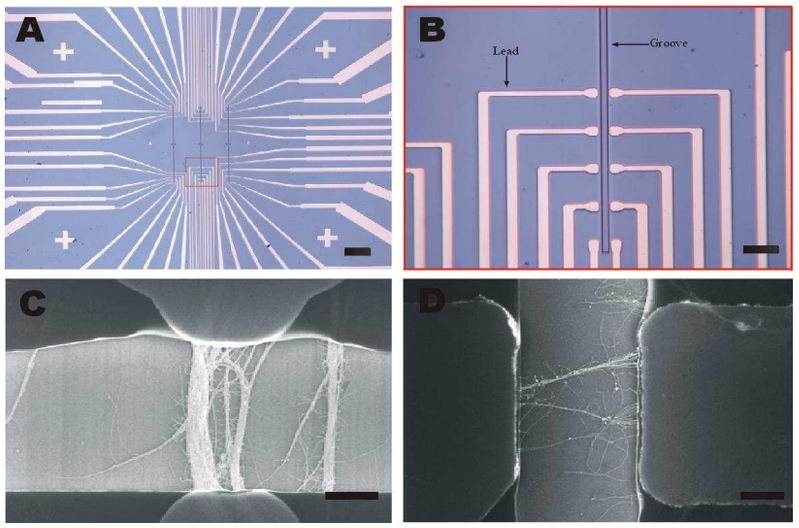

Figure 3.5. A **-** Optical image of the central area of a device array. The bright structures correspond to the metal leads, while the three lines in parallel in the middle are the grooves. Scale bar, 30 μm. B **-** Optical image from the region highlighted by the red box in A showing one row of pair of leads passivated with PMMA and separated by a groove. Scale bar, 5 μm. C and D **-** Representative SEM images of ropes of nanowires assembled over pair of leads passivated with PMMA. Scale bars, 1 μm.

After this passivation process, I-V characterization of each device containing the nanowires was performed again. A flow-chart summarizing this step of device preparation is shown in Figure 3.6.

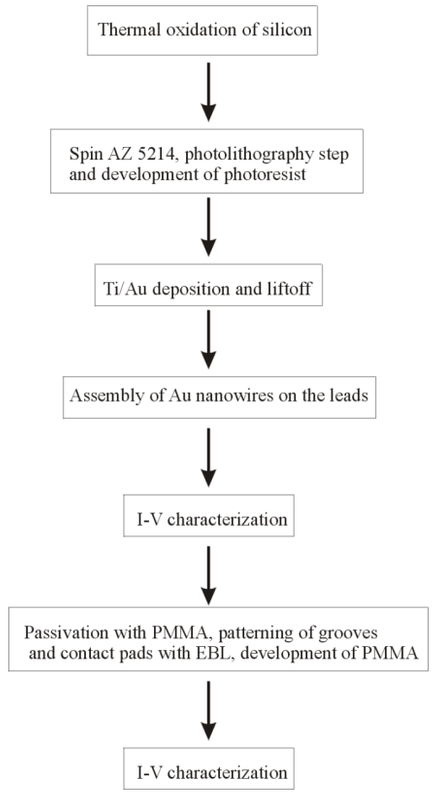

Figure 3.6. Flow-chart summarizing the steps for fabrication of Au nanowire devices passivated with PMMA.

3.5 Surface Modification of Au Nanowires and Electric Characterization in Solution

The devices produced as described in Section 3.4 were then characterized in solution. The next Sections will describe how measurements were performed in salted solutions and also how the surface of nanowires was modified with alkanethiols and electrical characterization of such wires was carried out in aqueous media.

3.5.1 Electric Characterization of Au Nanowires in Salted Solutions

The electrical characterization of passivated Au nanowire devices was firstly carried out employing aqueous solutions with different concentrations of NaCl (> 99,0%, Sigma-Aldrich). The I–V curves of the devices were measured using the Keithly semiconductor analyzer (model 4200 SCS) after a drop of the salted solution had been placed over the central area of the chips where the devices were produced. After the measurements, the devices were washed with Milli-Q water and dried with a stream of Ar.

3.5.2 Surface Modification of Au Nanowire Devices with Alkanethiols

The surface of Au nanowires was modified with three different kinds of alkanethiol molecules, i. e., 1-mercapto-propane (thiolpropane), mercapto-propionic acid and cysteamine. All the alkanethiols were purchased from Sigma-Aldrich and presented purity > 98,0%. Solutions with different concentrations of the respective alkanethiols were prepared in absolute ethanol (from Merck). The surface modification of Au nanowires was performed by exposing the central area of the devices to the alkanethiol solutions for 10 min. Afterwards, the devices were first washed with absolute ethanol and then rinsed with Milli-Q water and dried with a stream of Ar. The electrical characterization of the modified Au nanowires was also carried out using the Keithly semiconductor analyzer (model 4200 SCS). I–V measurements were led in air and also with the surface of the devices covered with a drop of Milli-Q water.

3.5.2.1 Zeta Potential Measurements

In order to estimate the surface potential generated by the adsorption of such alkanethiol molecules on nanowires, zeta potential measurements were carried out. In doing so, Au nanowires dispersed in hexane were centrifuged during 15 min at 20 000 rpm. Afterwards, the supernatant was removed and 10 mmol L^{-1} of alkanethiol solutions prepared in absolute ethanol were added over the nanowires precipitated in the bottom of the flask. After 10 min the alkanethiol solutions were removed and the wires were washed twice with pure Milli-Q water before Zeta potential measurements. For Zeta potential measurements a Malvern ZetaSizer 4 equipped with a LaserZee Meter (Pen Kem Model 501) was then used. For each sample, 5 independent measurements were carried out. All data were recorded at 20 °C.

3.6 Device Surface Preparation and Experiments with Neuronal Cells

As introduced in Chapter 2, sensing the electrical activity of electrogenic cells using ultrathin Au nanowires requires that we plate the cells over the nanowires, which should be assembled and electrically contacted on a solid platform. The following Sections will report the seeding of neuronal cells over the passivated Au nanowire devices and how the electrical measurements were conducted.

3.6.1 Chip Surface Preparation for Cell Culture

In order to perform the cell culturing, firstly a compartment to keep the culture medium on the surface of the chips had to be adapted. In doing so, a glass funnel was glued with PDMS mixed in a 5:1 ratio of base to curing agent on the chips, and left for 2 h in an oven at 60 °C to cure the polymer. A representative chip containing a funnel in its surface is shown in Figure 3.7. Afterwards, the chips were left in a bench for 1 h under ultra-violet (UV) light for sterilization. In sequence, the surface of the chips was covered for 40 min by 500 µL of a solution 0.1 mg/mL

of poly-l-lysine (PLL). After this period, the PLL solution was removed and the surface was not washed.

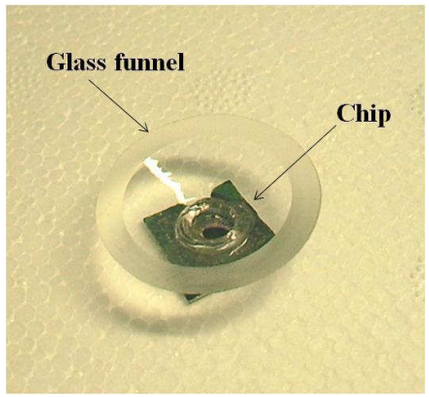

Figure 3.7. Photo of a representative chip containing the Au nanowire devices and a glued glass funnel in its surface.

3.6.2 Cell Culturing

The electrogenic cells used in this step were cortical neurons, the whole protocol describing the cell culture is given in Appendix B.

Cell Platting – Cortical Neurons: Day 18 embryonic primary cortical cells from pregnant Wistar rats were suspended in culture medium (neurobasal serum-free medium containing 0.5 mM glutamine, B27 supplement and streptomycin antibiotic) and further diluted with neurobasal/glutamine/B27/streptomycin to the desired plating density. The cell suspension was transferred to sterilized and pre-incubated chip surfaces and incubated for 240 min at 37 °C in a 5% CO_2 incubator depending on the desired cell density. Excess cells were removed (except for a wetting layer on the chip surface) and fresh, pre-warmed medium was added. The chips containing the neuronal cells were incubated at 37°C with 5% CO_2 for periods of 7-10 days in vitro (DIV).

3.6.3 Immunocytochemistry Assays

The morphology of neuronal networks was investigated via immunocytochemistry assays using a fluorescence microscope from the company Carl Zeiss SMT, Oberkochen, Germany model AxioImager Z.1. The microscope had a filter system for the detection of fluorescence at wavelengths of 495 nm and 524 nm. Neuronal cells grew either over the chips containing Au nanowires or chips without nanowires (control samples) were stained with ethidium homodimer (EtHD, Invitrogen) and calcein (Invitrogen). Both calcein and ethidium homodimer are fluorescence dyes with excitation peaks at 495 nm and 524 nm, respectively. Both substances were added to the culture medium of the sample (concentrations were 1 mM of calcein and 2 mM of EtHD). The samples were incubated for 10 min at 37 °C and then were examined with fluorescence microscope. The analyses were performed after 7-10 DIV.

3.6.4 Cellular Recordings

The experiments to detect the electrical activity of the cells were carried out by applying different electrical DC biases to the couple of leads where the nanowires were assembled and consequently monitoring the change in current along the time. The biases were applied to the leads through a patch-clamp amplifier from HEKA Elektronik GmbH. In this system, an EPC-10 Triple PCI and an EPC-10 Quadro PCI were controlled by a personal computer running the software PatchMaster. By this means, up to seven channels on the chip could be operated at once, while each channel features a DA and an AD converter allowing the simultaneous application of a voltage ramp and the recording of a current. These currents could be measured down to the pA regime at a sampling rate of up to 50 kHz. An Ag/AgCl reference electrode was connected to the ground provided by one of the seven preamplifiers to maintain a stable reference potential. The entire box was grounded and the experiments were performed in a Faraday cage. Figures 3.8A and B show a photo of the HEKA amplifier and the arrangement of a chip electrically connected by two tungsten needles used to apply the DC biases to the leads where Au nanowires were assembled, respectively.

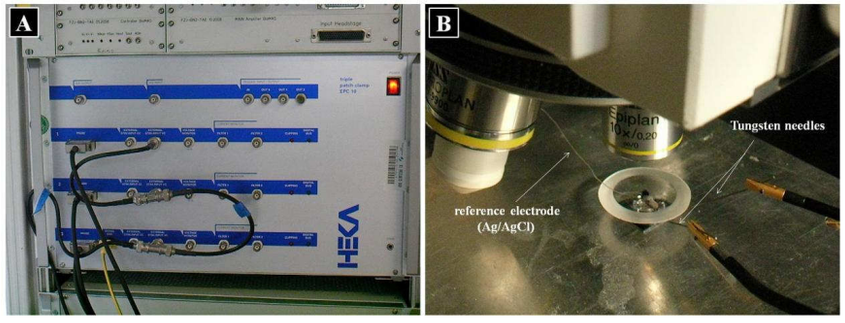

Figure 3.8. **A -** Photo of the HEKA amplifier used in the cellular recordings with the Au nanowire devices. **B** - Photo of the arrangement of a chip containing the Au nanowire devices being electrically connected by two tungsten needles. The arrangement of the Ag/AgCl reference electrode during the measurements is also shown.

3.7 Culturing of Cardiomyocyte HL-1 Cells for investigation of Cell-substrate interaction using Focused Ion Beam

For analysis of cell adhesion on passivated Au nanowire devices, cardiomyocyte HL-1 cells were employed. The HL-1 (Louisiana State University Health Science Center, New Orleans, LA, USA) cells is a cell line that represent a hybrid between embryonic and adult myocytes rather than an intermediate stage of myocyte maturation.[92] These cells were derived from AT-1 cells (mouse cardiomyocyte tumor) and maintain the phenotype and contractile activity of differentiated cardiomyocyte in vitro. The analysis of the interaction between these cells and the substrate where Au nanowire devices were produced was performed by focused ion beam (FIB). In a FIB workstation a focused gallium ion beam is used for ablation and deposition of material on the surface of a specimen. Cross-sections of a sample can be prepared with such beams, and as the FIB source is incorporated into a high resolution electron microscope, micrographs from those cross-sectional areas can be taken. The following sections describe the culturing of HL-1 cells, their fixation and the FIB analysis.

3.7.1 Culturing HL-1 Cells

The HL-1 cell line was cultured in T25 flasks at 37 °C and 5% CO_2 in Claycomb medium with 10% FBS, 100 µg/ml penicillin-streptomycin, 0.1 mM norepinephrine and 2 mM L-glutamine in an incubation chamber. After cells reached confluency and started beating, they were split and seeded onto the chips following standard protocols. Briefly, cells were rinsed with PBS followed by trypsination using 1 ml 0.05% trypsin/EDTA. Trypsination was stopped by adding 5 ml of medium followed by centrifugation for 5 minutes at 500 g. Supernatant was removed, and the pellet was re-suspended in medium. Approximately 2000 cells/mm^2 were plated on each chip in a volume of 50 µl. After 4 hours of initial adhesion, the chips were filled with 500 µl of medium. Medium was changed daily. The cells were fixed after 2 DIV.

3.7.2 Cell Fixation

The preparation of cultured HL-1 cells for analysis using focused ion beam (FIB) was performed as described in the following steps:

1. Firstly, the cells were rinsed twice at 37 °C with warm phosphate buffered saline (PBS).

2. Fixed for 12 h with 3.1% (v / v) glutaraldehyde in 20 mM HEPES buffer (pH 7.3 adjusted with NaOH).

3. Rinsed twice with Milli-Q water.

4. Dehydrated with an increasing isopropanol concentration (30%, 50% for 10 min each; 70% over night; and 90%, 95%, for 10 min each and finally stored in 100%).

5. Before the FIB analysis, about 10 nm of gold was sputtered on the surface.

3.7.3 FIB Analysis

The FIB-SEM system model used in the experiments was a Dual Beam of FEI (model Nova NanoLab 200). After depositing a platinum (Pt) layer over the area where the cells were grown, a beam of gallium (Ga^+) ions of 30 kV and current of 6.5 nA was used for cutting parts of this area and produce the cross-sectional areas to be analyzed with SEM.

Chapter 4

Results and Discussion

In this chapter, the findings and the discussion of the results related to the synthesis, electrical characterization and application of ultrathin Au nanowires as sensors will be presented. The chapter was organized with the following sequence: Initially, the results about the synthesis and the chemical mechanism involved in the formation of Au nanowires will be shown and discussed. From Section 4.5 the results about assembly, electrical characterization of ultrathin nanowires in air and in solution are demonstrated. The last part of this chapter (from Section 4.6) shows some preliminar results to use the nanowires as sensors to detect the electrical activity of neuronal cells.

4.1 Synthesis of Ultrathin Au Nanowires

The synthesis of ultrathin Au nanowires is from an experimental point of view relatively simple, as demonstrated in Section 3.1. Overall, the synthesis involves the mixing of a metal salt precursor such as AuCl with oleylamine and a small amount of hexane just to help the dissolution of the salt. In this case, oleylamine acts as a solvent, reducing agent and stabilizer. It was noted during the period of 24 h when the reaction was left undisturbed that the color of the solution changed gradually from light yellow to almost colorless. Additionally, a whitish gel was formed in the bottom of the flask. This gradual change in the color of the reaction solution indicated the complexing of Au(I) by oleylamine, while the presence of the whitish gel strongly suggested that the co-produced $[Au(oleylamine)]^{+}$ complex formed polymeric chains, as it was already pointed out.[9-11] More details about the formation of this complex will be presented and discussed in Section 4.2. Without heat the reaction, the color of the solution and of the whitish gel remained almost the same for several days. A very light red color could only be observed in the solution after 3 days. This light red color was attributed to the formation of Au nanoparticles. The production of these nanoparticles and also of Au nanowires involves an electroless reaction,

where Au(I) ions are reduced and oleylamine molecules are oxidized. In aqueous media, the electrochemical potential to reduce Au(I) to Au(0) is 1.83 V versus NHE (normal hydrogen electrode), indicating that Au(I) species are strong oxidizing agents.[67] The electrochemical potential to oxidize oleylamine has not been reported yet. However, in general the reducing potential of the primary amine groups in organic molecules is lower than 1 V,[93,94] suggesting that these groups can easily be oxidized in the presence of strong oxidizing agents. Although these values cannot be applied to our reaction because they were determined for redox processes in aqueous solutions, we note that the potential of the cell for the reaction between Au(I) ions and oleylamine molecules should still be high. In this case, the limiting factor for the rate constant of electron transfer would be the organic media. Indeed, in less than 1 h heating the reaction at 80 °C the color of the solution became red, and after 6 h at this temperature it was dark red. Figures 4.1A-C show a sequence of pictures of a flask of the solution during these periods of the reaction. Transmission electron micrographs of the products of the synthesis demonstrated that ultrathin Au nanowires with diameter of 2 nm and length of a few micrometers were produced, Figures 4.2A-B. A few nanowires presenting diameter between 10 and 20 nm were also observed. Additionally, as pointed before Au nanoparticles were also produced during the synthesis of nanowires. The details for the concomitant formation of these particles are described in Section 4.2. The histogram in Figure 4.2C demonstrates that the predominant mean diameter of 75 nanowires was ≈ 2 nm. When Au nanowires were completely separated from Au nanoparticles in the end of the reaction and then dispersed in hexane, the solution presented a light brown color. Solutions containing Au nanoparticles dispersed in hexane were typically red, Figure 4.2D.

Figure 4.1. Sequence of photos of a representative flask of the reaction during different periods of the synthesis. A – Right after the dissolution of AuCl in oleylamine and hexane. B – After 24 h at room temperature leaving the reaction undisturbed. C – After heating the solution at 80 °C for 6 hours.

.

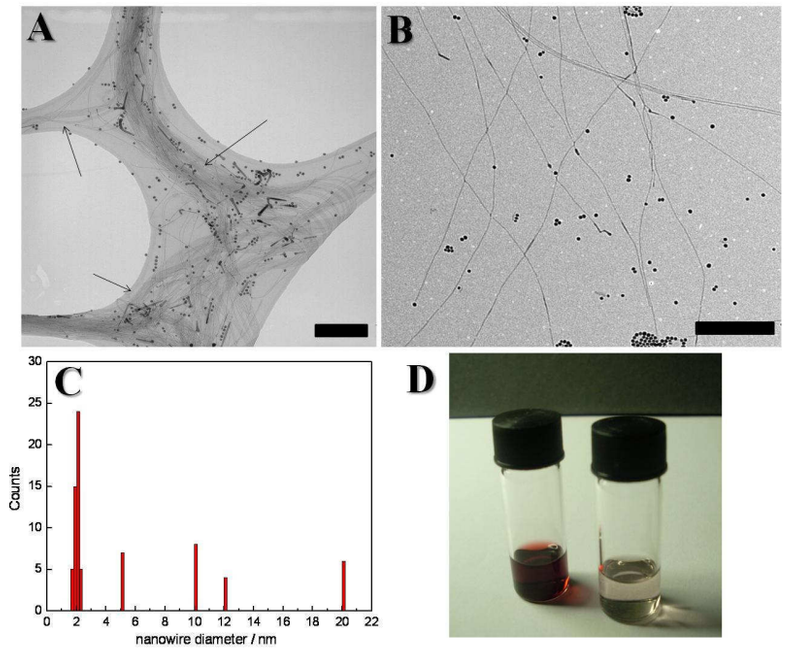

Figure 4.2. A and B – Transmission electron micrographs with low and high magnifications of the produced ultrathin Au nanowires (indicated by the arrows), respectively. The scale bar is 200 nm. C – Histogram of the distribution diameter of Au nanowires. D – Photo of solutions containing only Au nanowires (right flask) and nanowires and nanoparticles dispersed in hexane (left flask).

4.1.1 Influence of Aurophilic Interactions in the Formation of Au Nanowires

In Section 2.2.1, it was introduced how aurophilic interactions can be used to engineering new materials. It was also cited that Lu and co-workers reported that aurophilic interactions induced the $[Au(oleylamine)]^+$ complex formation and this complex generated polymeric chains that assisted the synthesis of ultrathin Au nanowires with diameter of about 2 nm and length of a few micrometers.[9] The experimental evidences of aurophilicity phenomenon showed by Lu *et. al* were not clear and as a matter of fact the interactions between Au(I) ions and oleylamine molecules are very ambiguous. In this part of the work, it was attempted to investigate these

interactions and the possible influence of aurophilic attractions in the formation of Au nanowires. In doing so, the whitish gel, which was formed during the reaction and was attributed to the [Au(oleylamine)]$^{+}$ complex formation, was precipitated out and analyzed by differential scanning calorimetry. Table 4.1 list the endothermic and the exothermic peaks found during the DSC analysis of oleylamine only and for the whitish gel formed by oleylamine and Au(I) ions.

Table 4.1 – Endothermic and exothermic peaks and the correspondent enthalphies for DSC analysis of oleylamine only and oleylamine/Au(I).

	Heating (°C)	**Cooling (°C)**	**Enthalpy – Heating (kJ/mol)**	**Enthalpy – Cooling (kJ/mol)**
Oleylamine only	16.2	5.1	16.6	-21.6
Oleylamine/Au(I)	14.2	4.2	4.9	-9.3
	54.8	30.9	26.4	-38.5
	79.8	74.3	15.3	-16.4

The presence of an endothermic and an exothermic peak for oleylamine only clearly indicated that the molecules exhibited a crystalline organization, where the endothermic peak at 16,2 °C with an enthalpy of 16,6 kJ/mol reflected the melting point of the crystal and the exothermic peak at 5,1 °C with an enthalpy of 21,6 kJ/mol its crystallization temperature. Although there are no DSC data available on literature for oleylamine, these values were similar of that found during DSC analysis of cis-9-octadecenoic acid (oleic acid).[95] For cis-9-octadecenoic acid it has been well established that the molecules can crystallize in three different configurations, α, β and γ.[96] The melting temperature found for oleylamine was similar to that associated of the α crystalline form of cis-9-octadecenoic acid.[95]

Notably, the DSC analysis of whitish gel exhibited three endothermic and exothermic peaks, as listed in Table 4.1. The peaks of melting and crystallization at lower temperatures were close but not identical of those for oleylamine only. The enthalpies for these peaks were also much lower than those for oleylamine without Au(I). Interesting enough, melting and crystallization peaks at even relatively high temperatures (79,8 °C and 74,3 °C, respectively) were observed. The observation of these new peaks indicated the formation of the new transition phases in oleylamine when it was mixed with Au(I) ions. The melting and crystallization

temperatures of these new peaks suggested that even when the solution was heated the oleylamine molecules presented a certain crystalline organization. Iwahashi *et al.* demonstrated that cis-9-octadecenoic acid exhibits three different liquid structures: one in the temperature range below 30 °C, another between 30 °C and 55 °C, and above 55 °C with a crystallization transition occurring specifically between 70 °C and 80 °C.[95]

The precipitated whitish gel was also analyzed by x-ray diffraction. The respective spectra for oleylamine only and for oleylamine and Au(I) ions are shown in Figure 4.3. The data clearly demonstrate that new diffraction peaks were formed in the whitish gel in comparison to the spectra of oleylamine only. Additionally, a shift in the diffraction peaks was observed. These results are consistent with the observations from the data of DSC analysis, where new transition phases in the whitish gel were detected. Table 4.2 lists the correspondent interplanar spacing (*d*) values calculated using the Braggs'law[97] from the peaks at the 2θ angles showed in the x-ray diffraction spectra in Figure 4.3.

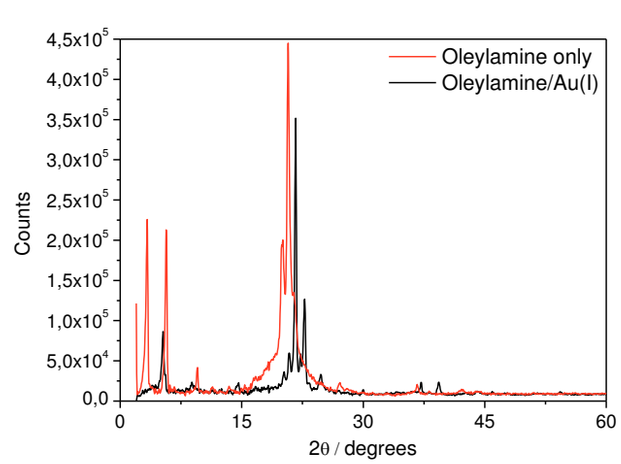

Figure 4.3. X-ray diffraction spectra of oleylamine only and the whitish gel formed by oleylamine/Au(I). Both spectra were recorded at room temperature.

Table 4.2 – The interplanar spacing (d) values calculated from the correspondent peaks at the 2θ angles of the x-ray diffraction spectra showed in Figure 4.3.

	short spacing / Å	intermediate spacing / Å	long spacing / Å
Oleylamine only	2.05 2.13 2.35 2.44 3.29 4.15 4.28 4.43	6.56 7.77 9.30	15.54 26.63
Oleylamine/Au(I)	1.68 1.97 2.04 2.28 2.41 2.97 3.31 3.59 3.90 4.10 4.24 4.39	6.09 9.98	16.73

For oleylamine only, the shortest spacing values were from 2.05 Å to 4.43 Å. These values are attributed to the distance between adjacent molecules, and strongly suggest that oleylamine molecules aggregate in parallel with each other producing a rodlike configuration, as it was also pointed out for cis-9-octadecenoic acid.[98] The long spacing values found were 15.54 Å and 26.63 Å. These long distances were related to the plane made by aligned molecules and indicated the typical formation of molecular clusters having a lamellar structure in the liquid phase.[95,98] Intermediate spacing values from 6.56 Å to 9.30 Å were also observed and correlated to the distance between these lamellas formed by the molecules.

The *d* values found for the whitish gel exhibited peaks with short distances ranging from 1.68 Å to 4.39 Å. These values are shorter than those detected for oleylamine only and indicated that the distance between adjacent molecules was also shorter. Peaks with spacing values of 2.97 Å, 3.31 Å and 3.59 Å that were not observed in the spectrum of only oleylamine, were detected

in the spectrum of oleylamine and Au(I) ions. These values are typical distances for aurophilic interactions and strongly suggest that Au(I) – Au(I) interactions occurred and induced the oleylamine molecules to arrange in distances different from those of "pure" oleylamine.[18-20,99] Additionally, two peaks of intermediate distances at 6.09 Å and 9.98 Å, and only a single peak at 16.73 Å for long spacing were observed. This last peak was longer than the correlated long spacing peak of 15.54 Å observed for oleylamine only. Based on these results and also on those from DSC analysis, the following model to explain the interactions between oleylamine molecules and Au(I) ions was proposed: Oleylamine molecules (Figure 4.4A) have a molecular length that is between the long spacing values of 15.54 Å and 26.63 Å observed. In a liquid phase, these molecules form lamellar clusters and/or inverse micellar structures as illustrated in Figure 4.4B. In this case, the primary amine groups tend to be oriented to each other, whereas the alky chains can arrange longitudinally producing interdigitated structures. Due to the cis configuration of oleylamine molecules and the ability of the methyl and methylene groups near to the end of the alky chain to move significantly, the molecules are not straight and can present the crystalline organization having the respective long spacing as showed in Figure 4.4B. This kind of alignment in the longitudinal direction was also reported for cis-9-octadecenoic acid and dodecanoic acid molecules in A-form crystal.[95,98,100] This structure resembles the molecular organization in a smectic liquid crystal (Figure 4.4C).[30]

In the presence of aurophilic interactions, as demonstrated through the peaks at 2.97 Å, 3.31 Å and 3.59 Å in the whitish gel, oleylamine molecules can laterally interact with Au(I) ions through the free electron pair of primary amine groups (Figure 4.4D). In fact, due to the orbital delocalization in these Au(I) – Au(I) interactions, the ions have a higher electron affinity and can easily induce the molecular assembly of Lewis bases such as oleylamine molecules. This molecular assembly compact the adjacent molecules and makes their lateral distance shorter, as observed experimentally. Also, owing to the longitudinal orientation during the molecular assembly, long longitudinal intermolecular spacing could be enlarged or broken. The assembly and the lateral coalescence of these molecules would then induce the formation of the observed whitish gel. The results observed from DSC analysis indicated that such molecular configurations can exist even at relatively high temperatures. Thus, it means that during the reduction of Au(I) ions to Au(0), the assembled molecules could still present a crystalline organization that would assist the formation of the ultrathin Au nanowires.

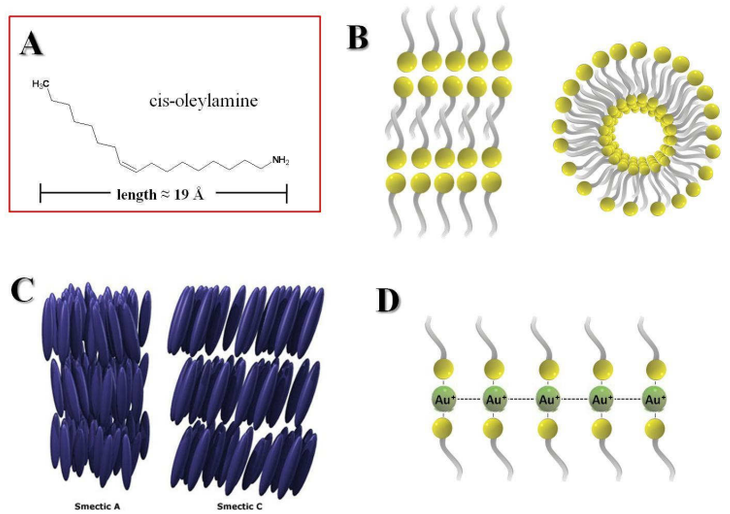

Figure 4.4. A – Molecular structure of oleylamine. B – Illustration of the lamellar (left) and micellar (right) configurations formed by oleylamine molecules in liquid phase. The yellow balls represent the primary amine groups, while the gray tails are the alkyl chains of the oleylamine molecules. C – Representation illustrating the similarities in the molecular arrangement of oleylamine with the molecular configuration of two kinds of smectic liquid crystals. The Figure was adapted from ref. [101]. D – Representation of the assembly of oleylamine molecules in Au(I) ions interacting with each other through aurophilic interactions.

The model could also be confirmed through additional experiments for the synthesis of Au nanowires by replacing hexane for chloroform. Figure 4.5 shows that in the presence chloroform, only Au nanoparticles with a mean diameter of 10 nm were produced. This is consistent with the fact that upon addition of a solvent that presents a molecular structure, which was able to better interact with the primary amine group of oleylamine, it could break the crystalline network formed by oleylamine molecules. Naturally, oleylamine still presented an inverse micellar configuration and led to the formation of nanoparticles. The same results were also reported by Lu and co-workers, who synthesized only Au nanoparticles when AuCl was dissolved in oleylamine and chloroform and the reaction was then heated.[102]

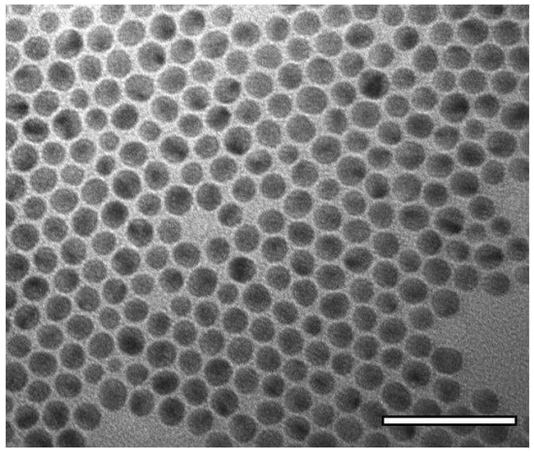

Figure 4.5. Transmission electron micrograph of Au nanoparticles produced when hexane was replaced by chloroform during the synthesis of nanowires. Scale bar is 50 nm.

Another independent verification of the influence of aurophilic interactions in the assembly of molecules that could assist the formation of nanowires was made by analyzing the products of the reactions when $CuCl_2$ and $AgNO_3$ were used as metal precursors. As demonstrated from Figures 4.6A and B, only Cu and Ag nanoparticles were produced, respectively.

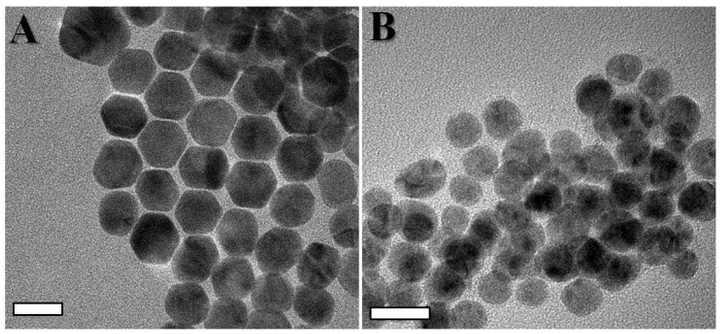

Figure 4.6. Transmission electron micrographs of Cu (A) and Ag (B) nanoparticles produced employing the same experimental conditions used to prepare Au nanowires, but using $CuCl_2$ and $AgNO_3$ as metal precursors. Scale bars are 20 nm.

Indeed, during the period of 24 h when both reactions were left undisturbed at room temperature, no whitish gel was observed. Thus, indicating that the formation of this whitish product in the synthesis of Au nanowires occurred due to the aurophilic interactions and it was essential for producing such wires. As expected, Cu^{2+} and Ag^{+} ions do not form metallophilic interactions, and thereby could not induce the formation of new crystalline phases in oleylamine that would assist the production of nanowires from the respective metals.

These findings revealed an important piece in the synthesis of ultrathin Au nanowires using the respective chemical approach. That is, how aurophilic interactions can induce the molecular organization of oleylamine in solution, and how this organization can assist the formation of Au nanowires with diameters of about 2 nm. Although these results were important to understand the synthesis of nanowires, several questions regarding the chemical processes involved in the formation of this whitish gel are still elusive. Based on these concerns, the following Section will present the results about the complexation of Au(I) ions by oleylamine molecules.

4.2 The Chemical Complexation of Au(I) Ions with Oleylamine

One of the main purposes of this thesis is to understand the chemical processes that lead to the formation of Au nanoparticles and ultrathin Au nanowires. In this context, little is known about the chemical equilibrium formed between the micellar complex of oleylamine and aurous halide during the synthesis of Au nanoparticles and nanowires employing a Au(I) precursor. In this Section, the investigation of the stability constant of the intermediate oleylamine/Au complex during the first stages of the reaction that produces Au nanoparticles using an amine compound as reducing agent will be reported. A similar version of this Section appeared in Journal of Physical Chemistry C,113, 20143-20147, 2009.

4.2.1 Fundamentals of Intermediate Complex during the Synthesis of Au Nanoparticles and Nanowires using Aurous Halide

Due to their intrinsic eccentricities, in particular, Au nanoparticles are one of the most exploited systems applied in the nanoelectronic industry.[103-105] The literature contains plenty of

reports dealing with chemical methods for producing Au nanoparticles.[106-108] However, the ability to synthesize them in a monodispersed manner with a well-defined crystalline core, size, shape, and highly oriented structure remains a challenge. Recently, one interesting and alternative approach was demonstrated by Lu *et al*.[102] They used an oleylamine/aurous halide complex to produce Au nanoparticles with an average distribution size ranging from ~ 4 to 12 nm with a low polydispersity. A templateless approach such as that using amine complexes of the Au(I,III) species is very promising. It offers great flexibility for producing not only highly symmetric nanostructures, but also nanoparticles of different sizes under mild conditions, where oleylamine simultaneously acts as both reducing agent and stabilizer. In addition, it has been proposed that if the nucleation of metal is controlled in the intermediate complex, where Au is in a +1 oxidation state, different morphologies of Au nanostructures can be obtained.[109] However, the complexation stages and chemical equilibrium involved in such a reaction are not well known and have been poorly exploited in the past. As different interactions may cause different stabilization and concomitantly varied complexing steps, it is imperative that the equilibrium of complexation be characterized for these species. In order to analyze the chemical equilibrium of this reaction, the following sub-sections will describe how we determined the stability constant of the intermediate complex formed between oleylamine and Au(I) during the first stages of the reaction. A spectrophotometric investigation showed that the complex has two equilibrium constants that were dependent on Au(I) precursor concentration.

4.2.2 The Complexation of Au(I) by Oleylamine

Oleylamine molecules form inverse micellar structures by self-assembling the polar groups (-NH_2) attracting each other and forming a kind of core, where the amine groups can interact with Au species, while the hydrophobic chains alternate in a perpendicular direction (Figure 4.7A). When the AuCl was mixed with oleylamine (OA), a complex of general form co-existed in equilibrium:

$$AuCl + OA \rightleftharpoons [Au(OA)]^{+} + Cl^{-}$$

Leaving the reaction undisturbed at room temperature led after a few hours to the formation of a whitish gel, which was associated here with the self-assembly of linear polymer chains of the

coordinating ligand formed through aurophilic interaction, as it was proposed on literature and we observed in section 4.1.1[9,110] As the electroless reaction between Au(I) species and primary amine-based compounds is thermodynamically favorable, oleylamine chains can slowly be oxidized at room temperature, while Au(I) can be reduced to Au^0 and consequently form Au nanoparticles, as indicated by :

$$[Au(OA)]^+ + Cl^- \longrightarrow Au^0 + OA^+ + Cl^-$$

The Au nanoparticles (Figure 4.7B) produced using this procedure present a narrow size distribution of ≈ 10 nm with a low standard deviation of about 8.6 % (Figure 4.7C). The diameter can still be tuned by changing the total time of reaction.[102] As the particles are capped with a very thin layer of oleylamine, they can even be assembled to form monolayers of nanoparticles on unmodified surfaces (Figure 4.8). Selected area electron diffraction (SAED) of such particles (inset Figure 4.7B) shows they are polycrystalline.

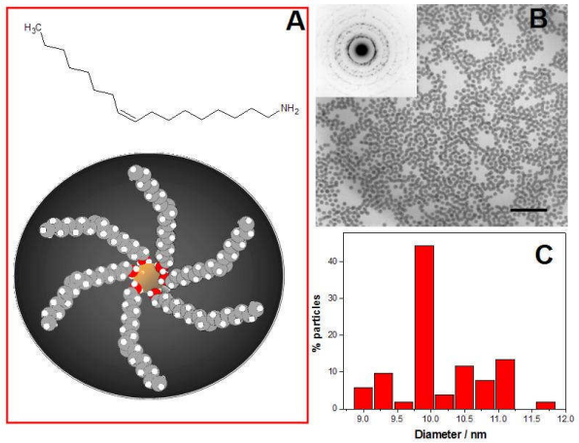

Figure 4.7. A- Top: the molecular structure of oleylamine; bottom: a schematic illustration of the micellar complex formed around the Au species (brown ball). The white balls represent hydrogen atoms, gray are carbon and red nitrogen atoms. B - TEM image of Au nanoparticles (scale bar is 100 nm). The inset shows the SAED pattern. C - Histogram of the particle size distribution.

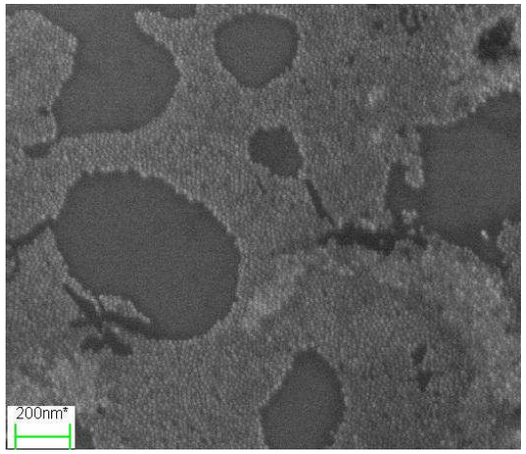

Figure 4.8. SEM image of Au nanoparticles dispersed on a SiO_2 surface.

4.2.3 The Mechanism of Chemical Complexing

In order to follow the mechanism of chemical complexing during the intermediate step of reducing Au(I) and forming nanoparticles, a spectrophotometrical investigation of the complex $[Au(OA)]^+$ was performed directly after dissolving AuCl in OA. Figure 4.9 shows the absorption spectra of the Au(I) complexes at different concentrations of the AuCl precursor. It can be clearly seen that the reaction between AuCl and OA is affected by the ratio of the species. Using a relatively low concentration of AuCl (Figure 4.9 curve b) any absorption band could be observed. However, increasing the concentration of AuCl to 0.9 mmol L^{-1} (Figure 4.9 curve c), a shoulder with an absorption maximum at 354 nm was detected. This band was attributed to the absorption of $[Au(oleylamine)]^+$ complex. A further increase in AuCl concentration resulted also in an increase in the complex concentration and the shoulder of absorbance tended to increase and bathochromically shifted to an absorption maximum at 384 nm (Figure 4.9 curves f, g, and h). It is well established that longitudinal shifts such as batho/hypsochromic shifts in the UV-visible spectrum are related with chemical changes in the solution.[111] Thus, the observed shift here would be in accordance either with the substitution of Cl^- ions with amine groups or

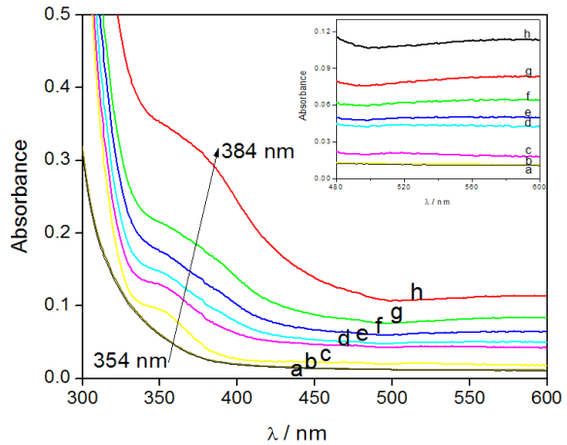

Figure 4.9. UV-visible spectrum of [Au(oleylamine)] complex at different concentrations of AuCl. a) only oleylamine, b) 0.2 mmol L^{-1}, c) 0.9 mmol L^{-1}, d) 10 mmol L^{-1}, e) 21 mmol L^{-1}, f) 32 mmol L^{-1}, g) 43 mmol L^{-1}, h) 64 mmol L^{-1}. The inset shows an expanded view of the UV-visible spectrum where the surface plasmon resonance from Au nanoparticles started to appear.

the reduction of Au(I) ions by amine groups followed by structural changes in the oleylamine molecule. In fact, it has already been showed in the literature that the reaction between amine compounds and Au(I) ions may lead to structural changes in the reducing molecule.[112-114] The broad absorption maximum between 500 and 600 nm, which was caused by excitation of surface plasmon vibrations in Au nanoparticles (insert Figure 4.9), confirmed the initial reduction of Au(I) and consequent formation of Au colloids. Further UV-visible experiments along the time to confirm that the initial absorption bands at 354 nm and 384 nm were due to the complex formation were also performed (Figure 4.10). UV-visible analysis of $[Au(OA)]^{+}$ complex at different concentrations of AuCl was performed just after mixing both compounds, after 4 h and again after 24 h. The UV-visible spectra (Figures 4.10 a) and b)) show that when AuCl in both concentrations, 0.9 mmol L^{-1} and 64 mmol L^{-1}, was just mixed with oleylamine, a shoulder with a maximum of absorption at 354 nm and 384 nm in each spectrum was observed, respectively.

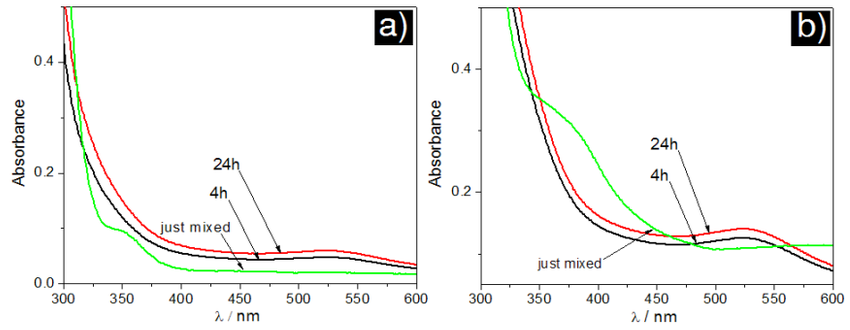

Figure 4.10. UV-visible spectra of [Au(OA)] complex with different concentrations of AuCl, a) 0.9 mmol L^{-1} and b) 64 mmol L^{-1}, at different times.

At this moment, a broad absorption band between 500 nm and 600 nm was also observed, but only when the concentration of AuCl was 64 mmol L^{-1}. After 4h, the UV-visible spectra for both cases show the same feature, that is, the shoulders of absorption at 354 nm and 384 nm disappeared, whereas the broad absorption band between 500 nm and 600 nm observed previously demonstrated a light increase. During this time, a light broad absorption band in the same region in the spectrum of AuCl 0.9 mmol L^{-1} was detected. At 24 h, this absorption band between 500 nm and 600 nm showed in both spectra a small increase in comparison to 4 h, while no shoulder of absorbance at 354 nm and 384 nm was seen. These observations not only corroborate that the shoulders of absorbance were due to the formation of $[Au(OA)]^+$ complex but also suggested the complex as a whole was unstable along the time. The broad absorption band between 500 nm and 600 nm and its light increase along the time also demonstrated that Au nanoparticles were formed while the $[Au(OA)]^+$ complex was being decomposed.

In order to clearly identify any chemical change in the oleylamine molecule caused by the reaction, solutions of Au(I) with different concentrations were analyzed by FTIR (Figure 4.11A). The major bands in the FTIR spectrum of oleylamine (Figure 4.11A, curve a) were characterized by a C-H stretch around 2850-2960 cm^{-1}, N-H bending at 1619 cm^{-1}, CH_2 bending at 1500-1300 cm^{-1}, a weak C-N stretch at 1071 cm^{-1}, and two typical bands of primary amine at 792 cm^{-1} and 721 cm^{-1} due NH_2 bending out of plane (NH_2 wagging).[115] A comparative analysis of FTIR spectra with different AuCl concentrations shows that when a relatively low concentration of AuCl was dissolved in oleylamine (Figure 4.11A, curve b), no significant difference was observed in relation to the pure oleylamine spectrum. The same behavior was observed during

the UV-visible measurements of 0.2 mmol L^{-1} AuCl , i.e. no absorption band could be seen (Figure 4.9, curve b).

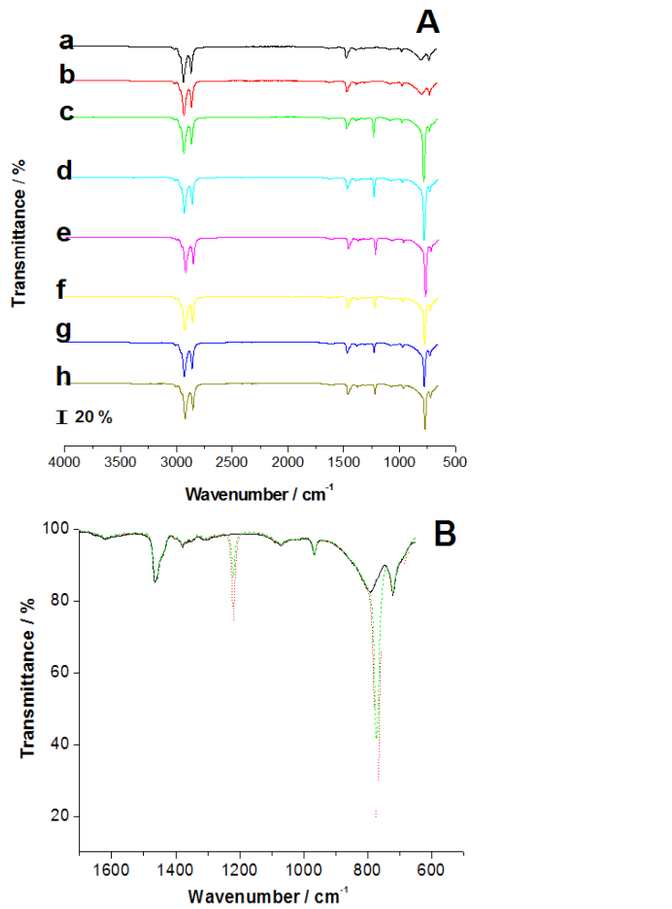

Figure 4.11. A - FTIR spectrum of oleylamine and $[Au(oleylamine)]^+$ complex at different concentrations of AuCl. a) pure oleylamine b) 0.2 mmol L^{-1}, c) 0.9 mmol L^{-1}, d) 10 mmol L^{-1}, e) 21 mmol L^{-1}, f) 32 mmol L^{-1}, g) 43 mmol L^{-1} and h) 64 mmol L^{-1} of AuCl. B - Expanded view of FTIR spectrum of curves a) (solid line), c) (dot line) and h) (dash line) shown in A.

However, when the AuCl concentration was increased to 0.9 mmol L^{-1} (Figure 4.11A, curve c), two new bands – one at 1219 cm^{-1} and another at 771 cm^{-1} – appeared in the fingerprint region. The former was attributed to C-N stretch, while the later, which clearly overlaps the band at 792 cm^{-1}, was ascribed to N-H wag. As in the fingerprint region each different functional group produces different patterns, this part of the spectrum can therefore be used to identify these two new bands. In this way, based on the positions of those bands, they were here attributed to the formation of a secondary amine (-C-NH-C-).[115] The formation of a secondary amine during the reaction between oleylamine and AuCl was also recently observed by Lu *et. al.*, who used mass spectroscopy to analyze the complex [AuCl(oleylamine)].[102] The deviation in the position of infrared bands is also associated with complex formation, which is responsible for shifts in the infrared spectrum.[116] Apart from this evidence of chemical change in the oleylamine molecule, it should also be noted that a further increase in the AuCl concentration led to a decrease in the intensity of these two new bands (Figure 4.11A, curves d-h). Figure 4.11B shows a comparison of the FTIR spectrum of solutions containing relatively low and high concentrations of AuCl. Taking into account the chemical equilibrium of the complex, the decrease in the intensity of the bands indicated that this secondary amine was not stable with the increase in the AuCl concentration. The stability along the time of this secondary amine was also checked (Figures 4.12, 4.13 and 4.14).

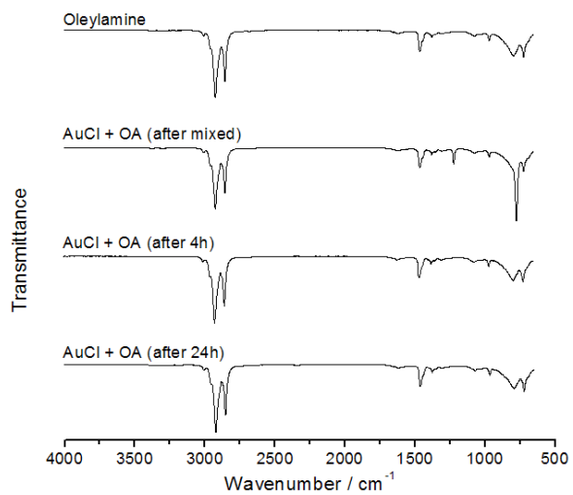

Figure 4.12. FTIR spectra of $[Au(OA)]^+$ complex at different times.

FTIR and MS analysis of $[Au(oleylamine)]^+$ complex with AuCl in a concentration of 3 mmol L^{-1} was performed just after mix both compounds, after 4 h and again after 24 h. The FTIR spectra show (see Figure 4.11A, c) that once mixed, two bands appeared in the fingerprint region at 1219 cm^{-1} and at 771 cm^{-1}, respectively (Figure 4.12). These bands, however, were not detected after 4 h and 24 h, and the FTIR spectra of the complex were similar to spectra with only oleylamine (Figure 4.12). The formation of this secondary amine was also observed in MS spectra (Figure 4.13).

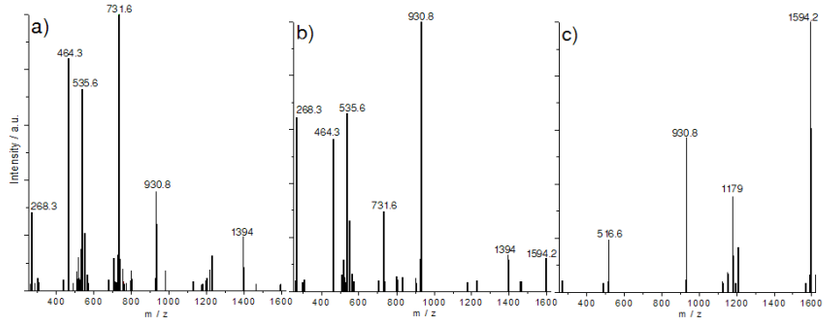

Figure 4.13. Mass spectra for $[Au(OA)]^+$ complex at different times. a) Once mixed, b) after 4h, and c) after 24h.

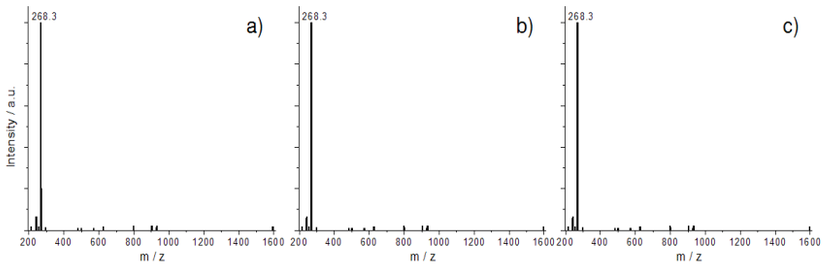

Figure 4.14. Mass spectra for oleylamine only at different times. a) Once mixed, b) after 4h, and c) after 24h.

The main peaks of $[Au(oleylamine)]^+$ complex just after mixed were at m/z: 268.3 for oleylamine, 464.3 for $[Au^I(oleylamine)]^+$, 535.6 for a dioleylamine $[C_8H_{17}\text{-}CH{=}CH\text{-}(CH_2)_8\text{-}NH\text{-}C_8H_{17}\text{-}CH{=}CH\text{-}(CH_2)_8\text{-}NH_2]^+$ with a secondary amine group, 549.6 for $[(dioleylamine)\text{-}CH_2]^+$, 731.6 for $[Au(dioleylamine)]^+$, 930.8 for $[Au^I_2(oleylamine)_2]^+$, and 1394 for $[Au^I_3(oleylamine)_3]^+$. After 4 h, the intensity of the peak at m/z: 731.6 drastically decreased. The same occurred for peaks at m/z: 464.3 and 535.6, whereas the peaks at m/z: 268.3 and 930.8 showed an increase. In addition, a new peak at m/z: 1594.2, which was assigned to $[Au^I_4(oleylamine)_3]^+$, was observed. At 24 h, the peaks at m/z: 464.3, 535.6 and 731.6

disappeared, while the intensity of the peak at m/z: 930.8 decreased. At this time, the peak at m/z: 1594.2 showed a significant increase. The analysis of MS spectra of only oleylamine along the time (Figure 4.14), showed a peak at 268.3 that corresponds exactly to the oleylamine molecule. These results confirmed the peaks observed in Figure 4.13 were due to the products described previously. Hence, based on the spectroscopic analysis, the following reaction mechanism for the observed experimental results was proposed.

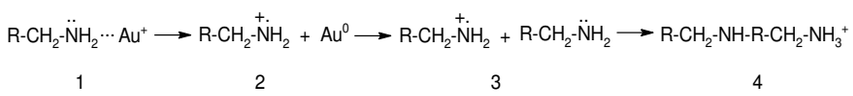

Scheme 4.1. Proposed reaction mechanism for oxidation of amine group of OA by Au(I) species. The OA molecule is represented here as R-CH_2-NH_2.

In other words, the oxidation of the primary amine group of OA and concomitant reduction of Au(I) species (**1**) led to the formation of an aminium radical (**2**) that was unstable and reacted quickly with other OA molecules (**3**) producing secondary amines (**4**). This secondary amine can, when the concentration of Au(I) is relatively low, be detected by both FTIR and MS analysis. If the concentration of Au(I) species is high enough, the rate of electron transfer is also higher and the secondary amines can subsequently be re-oxidized, and this functional group can no longer be detected by FTIR. The product of this new oxidation is still elusive, but one reasonable possibility is related to the peaks of the MS spectra at m/z: 930.8, 1394 and 1594.2, which suggest the oxidative polymerization of oleylamine.[9]

Thus, assuming that the shoulder of absorbance shown in Figure 4.9 was mainly to the complexing of AuCl by the amine group of oleylamine when both compounds were just mixed, the apparent stability constant (K_{sc}) for complexing Au(I) ions can be expressed as follows:

$$K_{sc} = \frac{[Au(C_8H_{17}CH=CH(CH_2)_8NH_2)][Cl]}{[AuCl][(C_8H_{17}CH=CH(CH_2)_8NH_2)]} \qquad \text{Eq. (4.1)}$$

where the square brackets denote the equilibrium concentrations of the species. The pH 7.5 of the solution was not altered throughout the reaction. For a condition of equilibrium, the following equation could be derived from Equation (4.1):

$$\log \frac{A_{max} - A}{A - A_{min}} = \log K_{sc} + n \log[AuCl] \qquad \text{Eq. (4.2)}$$

where A_{max} and A_{min} represent the absorbances at the maximum and minimum absorbance in the range of the AuCl concentration investigated (Figure 4.9), and A is the absorbance at any Au(I) concentration. The whole derivation of Equation 4.2 is given in Appendix C. Plotting the left side of Equation (4.2) versus log [AuCl] (Figure 4.15), an exponential curve that can be divided in two linear parts was obtained. From the interception of the straight lines in these linear parts, two stability constants K_{sc} were obtained for the complex. The values for K_{sc} were found to be 0.5 and 0.003 for low and high AuCl concentrations, respectively. These results indicate that when the concentration of AuCl is relatively low, a complex is obtained with a K_{sc} that is about 170 times higher than when the concentration of AuCl was relatively high.

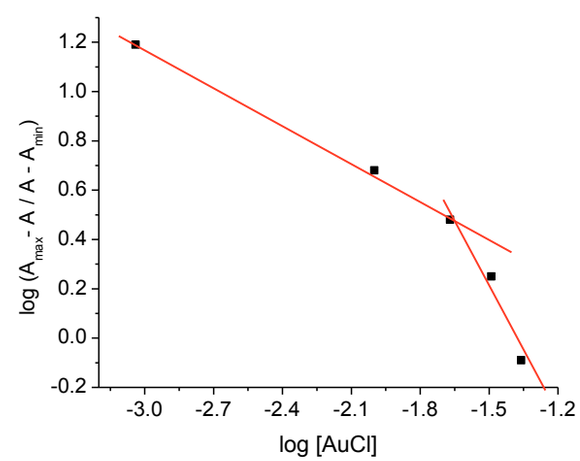

Figure 4.15. Logarithmic ratio of the difference between the absorbance (λ = 384 nm) at a specific concentration of AuCl, and the maximum and minimum absorbance of the $[Au(oleylamine)]^+$ complex as a function of log [AuCl].

These data are also in agreement with the previous results obtained by FTIR and MS analysis, which indicated the formation of an unstable secondary amine when the AuCl concentration was high. In practical terms, this suggests that at relatively low concentration of AuCl, aurophilic bonding can coordinate oleylamine to form supramolecular structures such as polymer chains which could mediate the synthesis of new metallic structures.

In summary, this study showed that the $[Au(OA)]^+$ complex presents two stability constants that were dependent on the concentration of Au(I) species. The calculated stability constant was significantly higher when the concentration of AuCl was lower than 10 mmol L^{-1}. This means that in this condition, the rate of electron transfer due to the electroless reaction between Au(I) and OA is relatively low. Thus, it is expected that oleylamine molecules are less affected by structural changes which could destabilize their supramolecular organization and alter either the final shape or morphology of structures. The findings obtained in this work open the way towards gaining a deeper understanding of the mechanism of formation of Au nanowires/nanoparticles or other structures using aurous halides precursors, for which the chemical reactions has scarcely been exploited. The next Section will present the structural characterization of these products, nanowires and nanoparticles, from the synthesis with oleylamine.

4.3 Structural Characterization

One of the most fundamental parts in the investigation of nanostructured materials is the analysis of their crystallographic structure. In this sense, some relevant points that are often observed in nanomaterials and that can directly influence their properties are, the presence of defects such as dislocations, stacking faults or twins and also the bond contraction in the interatomic distance. Based on these observations, this Section will present and discuss the structural characterization of ultrathin Au nanowires and nanoparticles using a transmission electron microscope and its limitation to analyze such thin structures. A similar version of this Section appeared in Materials Research Society Symposium Proceedings, vol. 1206, M16-29, 2010.

4.3.1 The Role of Oleylamine in the Nanowires Crystal Structure

In order to understand the crystal structure of nanoparticles and nanowires produced, it should be taking into account the role of the ligand shell in the synthesis. Owing to their molecular structure, which is formed by a polar head group (- NH_2) and a hydrophobic tail, oleylamine molecules (Figure 4.16A) as it was demonstrated before can form inverted micelles, where the amine groups can coordinate and consequently reduce the Au ions (Figure 4.16B). It is well known that in synthesis based on solution-phase, these reduced Au ions form small nuclei. After grown until a certain critical size, these nuclei present well-defined crystallographic facets and form crystalline seeds. The seeds can further grow into nanoparticles with several possible shapes, where the final shape of the particles is mainly defined by a minimization of the surface energy.[50,51] Figure 4.16C shows a HRTEM image of an Au nanoparticle produced during the synthesis of Au nanowires. The particle has a diameter of 11 nm and a spherical shape which minimizes the surface area and maintains a low surface energy. Twin boundaries which are indicated by arrows were observed. During the synthesis, the nanoparticles are capped with the oleylamine molecules, but as it is well known, the defects on the surface of the particles make them highly susceptible to localized oxidative etching by O_2/Cl^- (from the air and from the precursor salt, respectively).[50] This localized etching means that the etched face of the

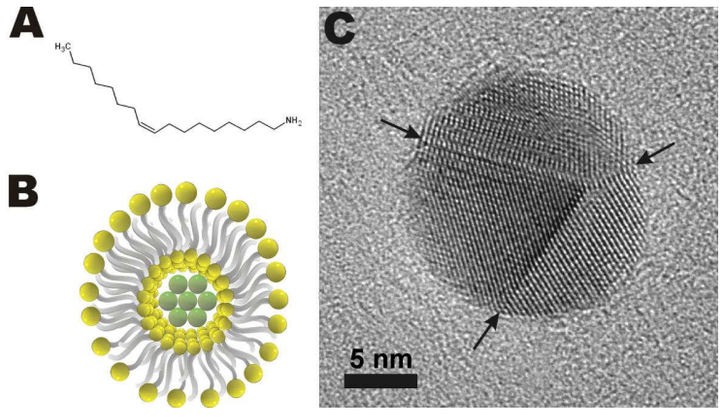

Figure 4.16. A - Molecular structure of oleylamine. **B** - Illustration of the micellar configuration of oleylamine molecules surrounding an Au nuclei (green spheres).Yellow spheres represent the – NH_2 group, while the gray tails represent the hydrophobic chain of the molecule. **C -** HRTEM image of an Au nanoparticle with a spherical shape. Arrows indicate the twin boundaries.

nanoparticle is activated and can consequently grow in one direction producing nanorods and nanowires. Figure 4.17A shows an electron micrograph of a nanoparticle (1) and Au nanowires (2 and 3) at low magnification. Thick Au nanowires of 10—14 nm in diameter (e.g. 2) as well as ultrathin AuNW (3) with a diameter of 1—2 nm were found. The thick nanowire (2) has a length of about 300 nm. The extremities of the thick nanowires often show a characteristic bulging. Figure 4.17B shows an enlarged image of the extremity of the thick Au nanowire in the boxed section of Figure 4.17A. The arrows point at a twin boundary. Figure 4.17C displays a HRTEM image of another Au nanowire extremity showing several twin boundaries (arrows). A HRTEM image of the body of a thick Au nanowire is displayed in Figure 4.17D which shows wavy contrast features. These are due to a bending of the nanowire along its long axis which causes a fluctuation of the high-resolution imaging conditions. Dislocations, stacking faults, twin boundaries or any other defects were not observed. In general we have observed that the main bodies of the thick Au nanowires were defect-free and single crystalline. The observation of defect-free single-crystalline nanowires is in contradiction with investigations by Ravishankar et

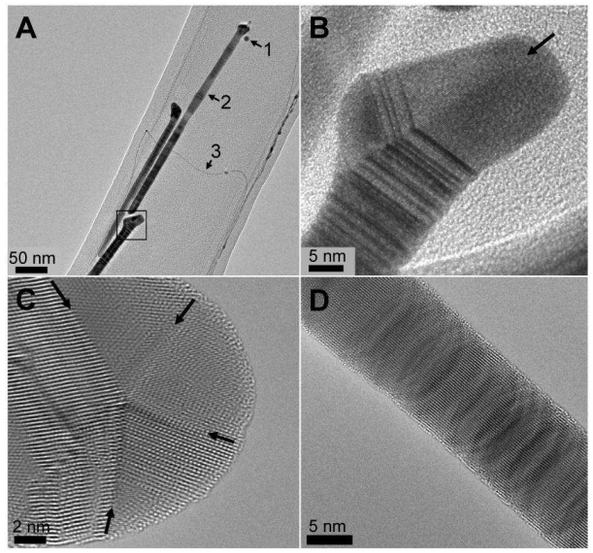

Figure 4.17. A - Electron micrograph of Au nanowires at low magnification. The arrows indicate a nanoparticle (1), a thick (2) and an ultra-thin AuNW (3). **B -** shows an enlarged image of an extremity of a thick Au nanowire which corresponds to the boxed section of A. The arrows point at a twin boundary. **C -** HRTEM image of a Au nanowire extremity showing twin boundaries (arrows). **D -** defect-free body a Au nanowire.

al., who proposed that Au nanowires produced by this micellar approach follows an oriented attachment mechanism of growth.[7] In that case, twin defects were seen along the growth direction of Au nanowires. In fact, the experimental conditions used by Ravishankar et al. involved more chemicals and higher temperatures than those used by us, and are likely the main reasons for the differences observed in the atomic structure of the nanowires. Additionally, in comparison with nanowires produced by hard-matter template approaches, the surface of the wires fabricated here is relatively smoother.

Figure 4.18A displays an electron micrograph taken at low magnification showing a high density of ultra-thin Au nanowires. Often, these nanowires were present as bundles or ribbons

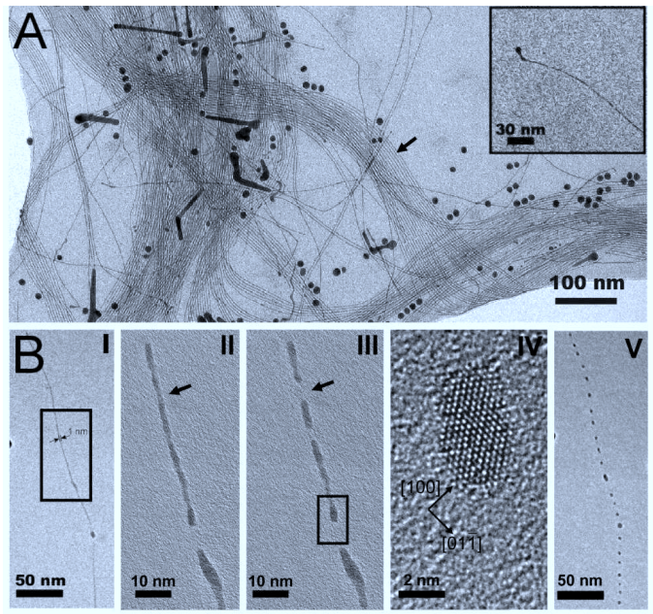

Figure 4.18. (**A**) Micrograph of bundles (arrow) of ultra-thin AuNWs. The inset shows the extremity of an ultra-thin AuNW. (**B**) A sequence of HRTEM images with different magnification which shows the breaking (arrows) of a AuNWs under electron beam irradiation. The images II and III were taken from the boxed region of I. Image IV was taken from the boxed region of III. It shows a fragment of the nanowire at atomic resolution. The fragment is oriented along a [011] direction of the fcc-Au structure. Image V corresponds to image I after exposing the AuNW to the electron beam for about one minute during the HRTEM investigation.

with a mutual distance of about 4 nm. The average diameter of such wires was 1—2 nm and their length was several micrometers. The insert in Figure 4.18A (top right) shows a micrograph of a single thinner Au nanowire. It is clearly seen that the extremity of the ultrathin Au nanowire shows qualitatively the same bulging like the thick Au nanowire. The wires were micrometer long and highly flexible. In solution-phase the wires were stable for months, however, when upon electron irradiation during TEM experiments, the ultrathin Au nanowires quickly degraded and broke up into fractions. Figure 4.18B I—V shows a sequence of micrographs of the same

ultra-thin AuNW taken at different magnifications. The sequence was taken during a time interval of about one minute and shows the degradation of the wire. Arrows in the images II and III, which were taken from the boxed region of I, show a breaking of the wire. Image IV, which was taken from the boxed region of III, shows a fragment of the nanowire at atomic resolution. The fragment was single crystalline and oriented along a [011] direction of its fcc structure. The [100] and [011] directions were indicated by arrows. A spacing of 0.3 nm between atomic columns along the [011] direction was measured, which is in accordance to the [011] lattice spacing of 0.29 nm of the fcc-Au lattice. Image V corresponds to image I after electron irradiation of the ultrathin Au nanowire for about one minute and shows a chain of drop-like fractions of the wire. Taking these observations into account, we consider that the oleylamine molecules with their micellar and tubular configuration have a fundamental impact on the atomic arrangement of the nanostructures observed here. That is, once the small nuclei start form, the shape of the subsequent nanocrystal was controlled by the organic molecule, which acted as both a capping agent and a stabilizer that thermodynamically reduced the surface energy. Thus, the presence of this capping agent could avoid the formation of defects such as twins or stacking faults along the Au nanowires. This is an important observation because the molecular configuration of oleylamine in solution is highly dependent on the presence of other solvents in the reaction. For instance, as demonstrated, when chloroform was used with oleylamine in the synthesis of Au nanowires, only Au nanoparticles were formed. Recently, Bernardi and co-workers showed that Au nanowires produced in a similar way of that employed in our work, have a high density of twin boundaries normal to the growth axis.[117] This result contradicts our observations here, however, it is worth to pointing out that in the synthesis of Bernardi *et al.* they dissolved the Au salt precursor in ethanol. The presence of ethanol, which is a very polar solvent, in the reaction can readily influence the molecular configuration of oleylamine, and thus, influence the crystal structure of the produced nanowires.

4.3.2 Observing Nanowires over Graphene Sheets

As discussed previously, it is difficult to resolve the crystallographic structure of ultrathin nanowires because they tend to melt under the electron beam of HRTEM. We have started in the

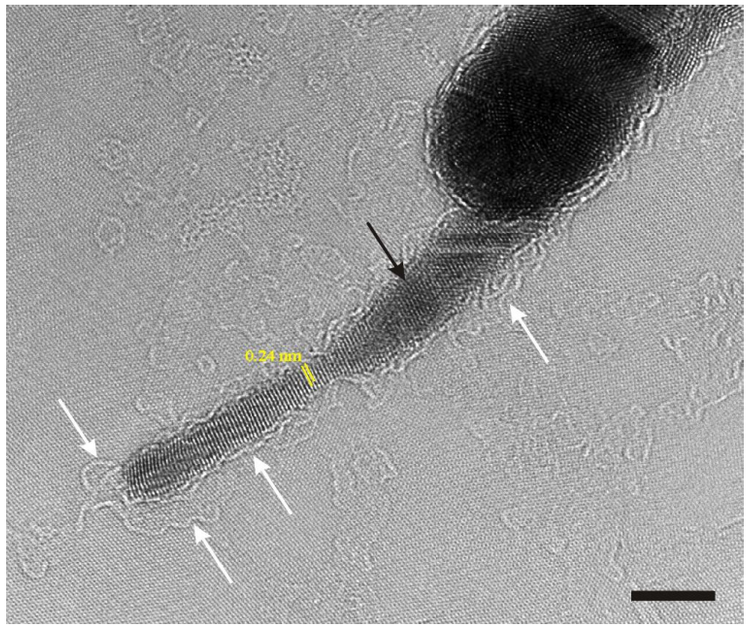

Figure 4.19. HRTEM micrograph of an ultrathin Au nanowire assembled over a graphene sheet. The scale bar is 5 nm.

last part of this thesis working in a new approach to overcome this problem. That is, it has been shown in the literature that aberration-corrected TEMs can resolve the structure of nanomaterials with atomic resolution at low accelerating voltages. However, the main limitation in this case is the support film, which is usually made of an ultrathin amorphous carbon layer that has a thickness of 2–3 nm and thus, it contributes significantly to electron scattering and decreases the contrast of low atomic number specimens. An alternative material that has been applied in the last few years for TEM support is graphene. Graphene is basically a single atomic layer of sp^2-bonded carbon atoms, that is chemically inert and consists of light atoms having a highly and stable ordered structure. In addition, graphene presents a high electrical and thermal conductivity. These fascinating properties have enabled the detection of light atoms, such as carbon and even hydrogen, and consequently also molecular layers on the surface of nanocrystals. Based on these, it was attempted to analyze through HRTEM the crystal structure

of ultrathin nanowires and the molecular layer of oleylamine in their surface using a graphene sheet.

Figure 4.19 shows an HRTEM micrograph of part of an ultrathin Au nanowire (indicated by the black arrow) assembled over a graphene sheet. From this micrograph, some important points can be seen: First, the diameter of this part of the wire is quite variable, presenting an enlarged end (diameter ≈ 3 nm) with a thinner middle part (diameter ≈ 2 nm) followed by another enlarged part having a diameter of about 5 nm. Second, the lattice structure could be resolved and indicated a single-crystalline structure for the wire. The interfringe distances were measured as 0.24 nm, which corresponds to (111) lattice spacing of the fcc structure of Au. Third, the hexagonal lattice of carbon atoms in the graphene support can be clearly seen. Also, the graphene sheet exhibits a much lower contrast variation than the commonly used amorphous carbon film. These aspects are important, because they allowed us to visualize blurred and undulating features (indicated by white arrows) around the nanowire, indicating the presence of oleylamine molecules coating its surface. The visualization of the molecules was only possible due to the difference in contrast between the graphene support and oleylamine coating. The same approach, but to observe citrate molecules covering Au nanoparticles was demonstrated by Lee and co-workers.[118] The oleylamine molecules on the nanowire were found to be 1–2 layers thick, and exhibited a thickness of ≈ 0.22 nm, which was close to the van der Waals radius of carbon atoms. The adsorption of these molecules on the surface of ultrathin Au nanowires was of extremely importance for the electrical characterization of the wires because it represents a significant isolating barrier for electron tunneling during the electrical transport, as it will be presented and discussed in the further sections. Although these are still preliminar attempts, it already demonstrated that it should be possible to analyze the crystallographic structure and molecules adsorption on the surface of Au nanowires with more details. Future research in this direction is very promising and may help to elucidate surface processes that lead to crystal growth with different shapes and properties.

In summary, the atomic arrangement of micrometer long ultrathin flexible Au nanowires was investigated by HRTEM. The Au nanowires observed here have diameters of 1—2 nm and 10—14 nm. Often their extremities showed a characteristic bulging and the presence of twin boundaries (thick Au nanowires). In contradiction with previous works, the bodies of the nanowires observed here are defect-free along the axial direction. Ultrathin Au nanowires were

often found as bundles presenting lengths of few micrometers. Although they were stable in solution for months, they were very sensitive to electron beam irradiation during HRTEM experiments with a tendency to break up into fcc-Au droplets. A hypothesis based on the micellar configuration of oleylamine was proposed to explain the observed atomic arrangement. Additionally, efforts to resolve the lattice structure of ultrathin nanowires and oleylamine molecules coating their surface were performed by using the new graphene support for TEM analysis. Although they were still preliminar analysis, they demonstrated to provide fundamental information of the molecular assembly over the nanostructures. A complementary study of the role of the structure in the growth of the nanowires will be presented in the next Section.

4.4 Growth Mechanism of Ultrathin Au Nanowires

Understanding the synthesis of ultrathin single crystal Au nanowires with high aspect ratio and that are stable in air is one of the main challenges for nanoscience and nanotechnology, and it was also the focus of this Section. It has been shown on literature and also in this thesis that 4 μm long ultrathin Au nanowires can be formed during the synthesis. Despite of the efforts to understand the mechanism of the reaction, an ultimate question concerning the growth of nanowires and the role of oxygen (O_2) during the synthesis remained unclear. In this Section the experimental data and discussion about the role of oxygen in the growth mechanism of nanowires and the oxidation of twin defects on Au nanoparticles formed in the first stage of the reaction will be presented. A similar version of this part of the thesis appeared in Chemistry: A European Journal, 17, 9503-9507, 2011.

4.4.1 The Growth of Nanowires Along the Time

The reaction between Au(I) ions and oleylamine and the consequent formation of Au nanostructures involves in a first step the formation of an [Au(oleylamine)]+ complex, followed by the reduction of Au(I) to Au(0) and subsequent formation of Au nanoparticles, as demonstrated in the previous sections. Although this is a thermodynamically favorable electroless process, at room temperature the reaction is relatively slow. Figures 4.20, 4.21 and 4.22 show transmission electron microscopy images of intermediate products taken at different time intervals during the synthesis of ultrathin Au nanowires. At t=0 h, that is, right after the compounds have been mixed, no products were observed, which indicates that the reduction of Au(I) species by oleylamine was relatively slow at this point. After 24 h, a small number of clusters consisting of smaller nanoparticles was visible (Figure 4.20). Energy-dispersive X-ray (EDX) analysis confirmed that the clusters consisted of Au particles.

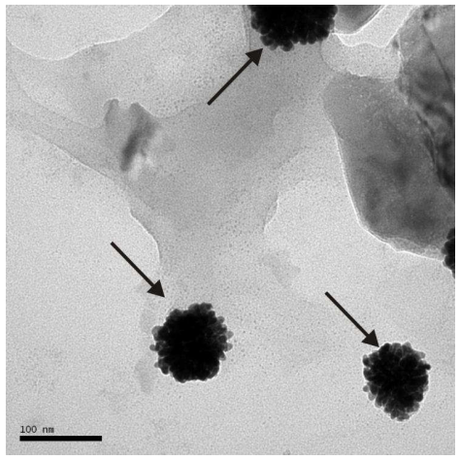

Figure 4.20. TEM image of intermediate product collected during the synthesis of Au nanowires at t = 24 h. The arrows indicate the clusters made of small Au nanoparticles.

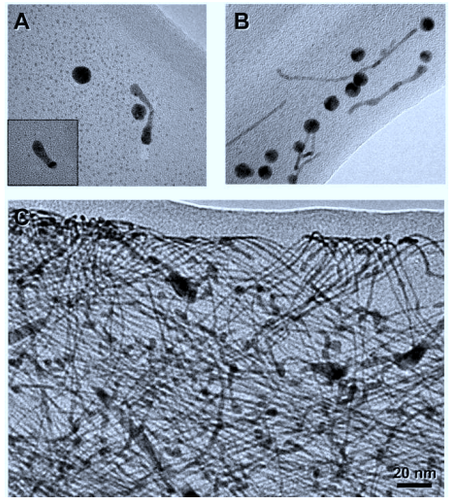

Figure 4.21. TEM images of intermediate products collected during the synthesis of Au nanowires at (**A**) t = 26 h; (**B**) t = 28 h and (**C**) t = 30 h. The inset in (A) shows a single nanorod. The micrographs are all in the same magnification.

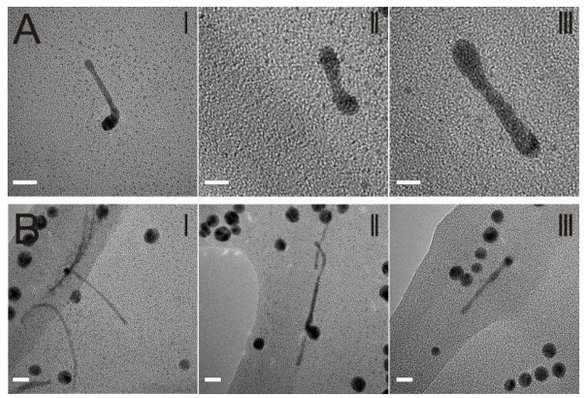

Figure 4.22. TEM images of intermediate products collected during the synthesis of Au nanowires at (**A** - I, II, III) t = 26 h and (**B** – I, II, III) t = 28 h. The scale bar is 20 nm.

Continuing the reaction, after 24 h the solution was heated to 80 °C and at t=26 h some Au nanoparticles and nanorods consisting of a thinner central part and two enlarged ends were observed (Figure 4.21A and Figures 4.22A). During the next 2 h (t=28 h), the amount of Au nanoparticles increased and elongated nanorods became visible (Figure 4.21B and Figures 4.22B). As the reaction was extended to t=30 h, the Au nanorods continued growing and evolved into ultrathin nanowires with an average diameter of 1.8 nm and a length of up to 2 µm (Figure 4.22C and Figure 4.23). A few nanowires with thicker diameters ranging from 10 to 15 nm were observed as well.

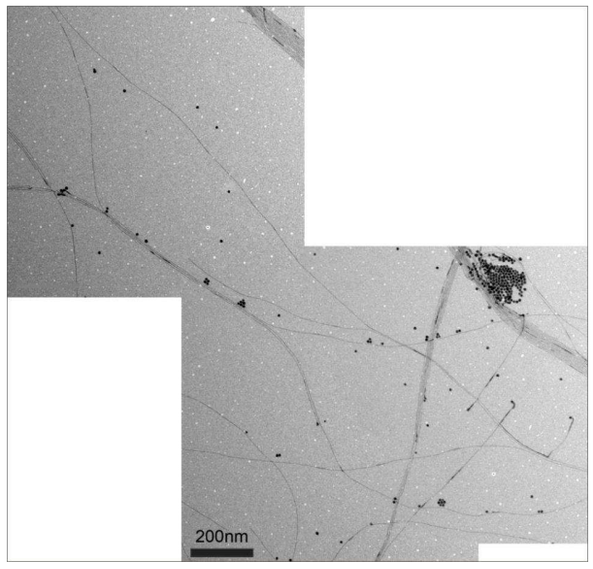

Figure 4.23. TEM images of Au nanowires showing high aspect ratio. This image was obtained by combining two TEM images along the extension of a bundle of nanowires on the TEM grid.

High-resolution TEM (HRTEM) images (Figure 4.24 and Figure 4.25) showed that the nanowires were monocrystalline with an interfringe distance of 0.23 nm, which corresponds to <111> lattice spacing of the face-centered cubic (fcc) Au. Unfortunately, the thin nanowires tend to melt under the HRTEM beam and it was difficult to resolve the crystal structure of such wires with better resolution (Figure 4.25).

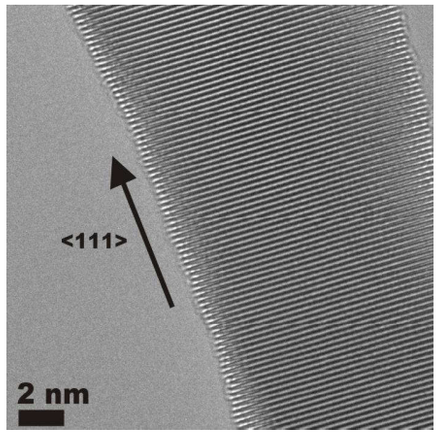

Figure 4.24. HRTEM image showing <111> growth direction for an Au nanowire with a diameter of 13 nm.

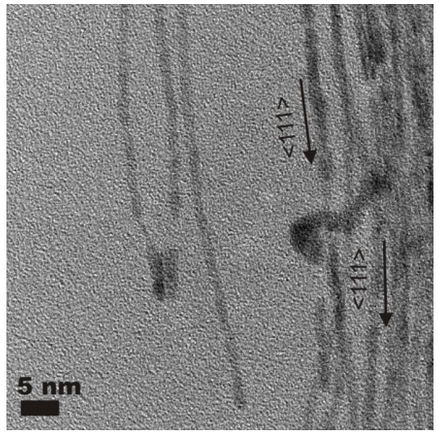

Figure 4.25. HRTEM images of Au nanowires with diameter of 2 nm and <111> growth direction.

The extremities of the wires were found to be enlarged as observed in the rods earlier (Figure 4.26).

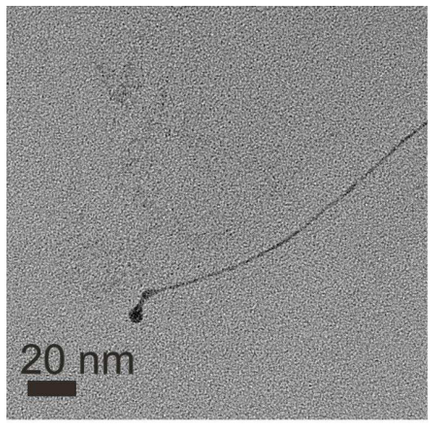

Figure 4.26. TEM image showing the enlarged extremity of a single Au nanowire.

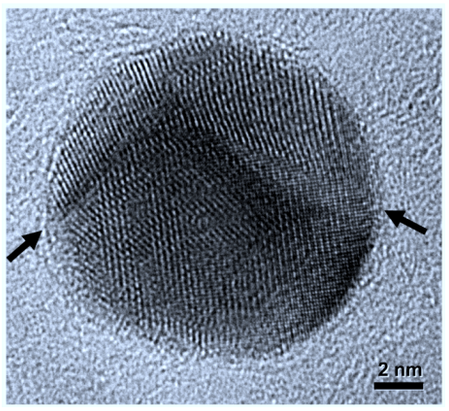

Figure 4.27. HRTEM image of an Au nanoparticle produced during the synthesis of Au nanowires. The arrows indicate the twin defects on the particle.

These characteristics during the synthesis and characterization of ultrathin Au nanorods and nanowires were also observed by others.[9,119] It can be concluded from these observations that the Au nanoparticles, which are produced from the reverse-micelle structure formed by oleylamine, assisted the growth of Au nanorods and nanowires from specific sites on their surface. HRTEM analysis of a representative Au nanoparticle demonstrated that the nanoparticle presents twin boundaries (Figure 4.27). The presence of such defects strongly suggests that these metal nanoparticles are more reactive on these sites and thus, more susceptible to oxidative etching commonly promoted by O_2/Cl^- etchant.[50,120–123] In fact, for relatively small nanoparticles the reactivity toward oxidation is expected to be higher.[124]

4.4.2 Oxidative Etching

To investigate the possible influence of oxidative etching, we carried out the same reaction as previously described using an inert atmosphere of N_2. In this way, new experiments employing AuCl and another one using Au_2S only, which was chosen to verify the influence of Cl^- ions, were performed. Figure 4.28A shows that when AuCl was used under an inert atmosphere, only spherical Au nanoparticles with a diameter ranging from 3 to 6 nm were observed at the end of the reaction. These particles presented a more heterogeneous average size distribution than the same reaction performed in air. These observations from experiments with AuCl alone imply that O_2 plays a fundamental role in the synthesis of ultrathin Au nanowires, while Cl^- species have negligible or no influence on their formation. When Au_2S is applied as a precursor, the sulfur species strongly bind to Au, and thus block its surface.[125] In this way, the binding of S^{2-} ions at specific crystal faces of Au nanoparticles could greatly reduce the growth rate along one direction and no nanowires would be formed. This observation was corroborated through Figure 4.28B, which shows that only Au nanoparticles with twin boundaries and larger sizes (≈12 nm) were formed when Au_2S mediated the reaction under N_2. The control experiments using Au_2S in air also showed that only Au nanoparticles, albeit larger, were produced (Figure 4.29). This difference between the size of nanoparticles produced using Au_2S in the absence and in the presence of O_2 also confirmed that O_2 should play a significant role in the growth of nanowires. For instance, the synthesis of larger particles when the reaction of Au_2S

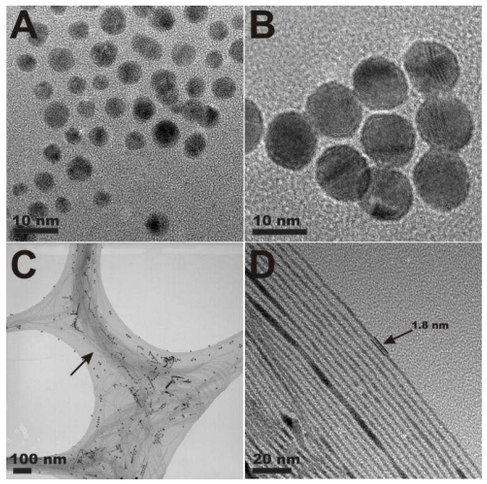

Figure 4.28. TEM images of Au nanoparticles obtained when the reaction was conducted under an inert atmosphere in (**A**) AuCl and (**B**) Au_2S. (**C**) and (**D**) TEM images of Au nanowires synthesized when O_2 was introduced into the solution during the last 6 h of the reaction using AuCl. The arrow in (**C**) indicates the nanowires.

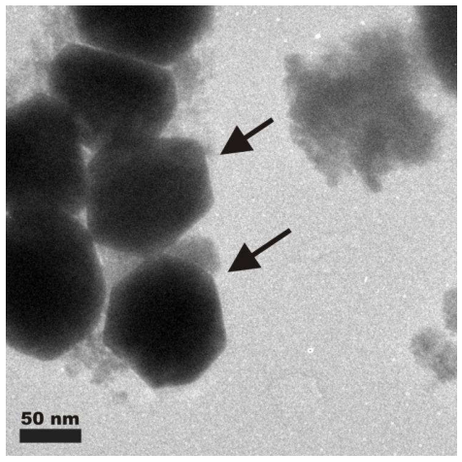

Figure 4.29. TEM image of Au nanoparticles obtained during the reaction between Au_2S and oleylamine in air. The arrows indicate the nanoparticles.

was performed in air can be attributed to the oxidative dissolution promoted by O_2, which can easily diffuse through the S^{2-} species bound to Au nanoparticles, followed by a higher rate of re-deposition of Au species. In fact, S^{2-} species are also strong reducers and could enhance the rate of this re-deposition of Au ions.[15] To confirm that O_2 played a fundamental role in the synthesis of ultrathin nanowires, we performed the reaction in the presence of AuCl and introduced O_2 into the solution during the last 6 h when the reaction was heated to 80 °C. In contrast to observations during the reaction under N_2, a huge amount of ultrathin Au nanowires with an estimated yield of approximately 80% was obtained (Figure 4.28C,D). The nanowires had an average diameter of 1.8 nm and a length of up to 8 µm (Figure 4.28D and 4.30A,B), which yielded an aspect ratio of approximately 4000. These findings confirmed that the presence of O_2 was mainly responsible for the growth of Au nanowires. By taking into account the oxidative-etching model, the twinned defects of the nanoparticles can provide active sites for localized oxidative etching that could induce in a subsequent step an anisotropic growth of the nanowires.[50]

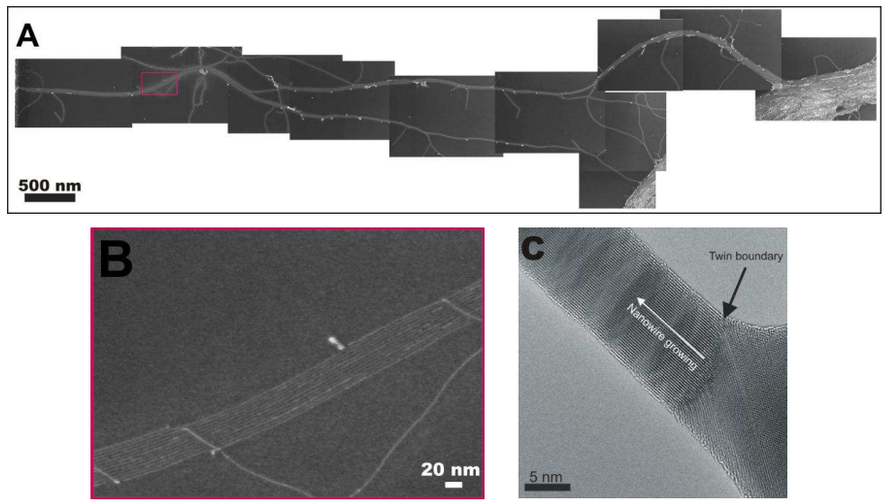

Figure 4.30. Scanning electron microscopy (SEM) images of Au nanowires obtained when O_2 was bubbled into the reaction with AuCl. (**A**) A series of 11 SEM images showing a bundle of Au nanowires that are 8 µm long. (**B**) Shows a higher magnification SEM image of the red framed region showed in A. (**C**) HRTEM micrograph showing the growth of an Au nanowire from a twin boundary in a nanoparticle.

Indeed, anisotropic reactivity and oxidative etching of Au spheroids assisted by O_2 has already been reported.[122,123] A similar mechanism to the growth of nanowires of other noble fcc metals, such as silver, has also been widely demonstrated in the literature.[119,126-129] In the present case, the surface of Au nanoparticles, which have a multiply twinned structure, was stabilized by adsorbed oleylamine molecules. This stabilization means that oleylamine molecules controlled the approach of metal ions from the solution to the surface of the nanoparticles and can greatly reduce or enhance the growth rate along one direction only. However, for anisotropic growth, one of the faces of the crystal has to be activated by removing the organic molecules. Due to highly reactive defect sites (twin defects) and the low energy of {111} facets, oleylamine molecules can selectively be removed from these faces during oxidative etching. During this etching of the twinned regions, Au would be oxidized to Au(I) or Au(III) species. As the reaction proceeds, Au(I/III) ions, which can be confined by the oleylamine molecules assembled over the particles, can be reduced and deposited onto the etched sites in a faster rate than the dissolution of atoms caused by etching.[51] Continuous etching and deposition eventually reshape and elongate the nanoparticles into ultrathin nanowires, which are more stable due to their defect-free structure along the axial direction.

Using a similar approach, Feng et al. showed that the yield of ultrathin Au nanowires can also be increased by adding a reducing agent during the synthesis.[12] In this case, it could be expected that the yield of the reaction should be higher, because the synthesis was carried out in air, in the presence of O_2, and was sped up by the reducing agent. The reducing agent accelerated the deposition of Au(I/III) ions on the low-energy facets of Au particles, which can be activated by O_2, and thus contributed to the faster formation of the nanowires. However, in this work the maximum length reached for the nanowires was 2 μm.[12] This difference in length in comparison to our results can be attributed to the initial stage of the reaction, which involved the formation of a $[Au(oleylamine)]^+$ complex that can form linear polymeric chains.[9] During the synthesis, this polymer was well characterized by the appearance of a whitish gel (see Sections 4.1 and 4.2). In fact, longer nanowires (≈ 4 μm) have been produced when this whitish gel that represents the polymeric chains of the $[Au(oleylamine)]^+$ complex was formed.[9-11] The presence of this whitish polymer in the work of Feng et al. was not mentioned.[12] The mechanism that we propose here is additionally supported by Figure 4.30C, which shows a representative micrograph of the growth of an Au nanowire through a twin boundary in a nanoparticle. Due to the instability of thinner

wires under the HRTEM electron beam, the micrograph was taken from a thicker wire. An example of growing Au nanorods from multiple twinned particles in a surfactant based solution was demonstrated by Gai and Harmer, although the oxidative etching was not mentioned in that case.[130] Additionally, Wang et al. showed in a similar synthesis that ultrathin Au nanowires can also grow in a single-crystal way from different defects such as dislocations and grain boundaries.[131] In particular, Wang and co-workers found that these defects appeared in kinked structures that were formed when the solution was stirred. While the authors did not discuss the role of O_2 in the dynamics of stirring, we believe that oxidative etching was responsible for the kinked structures found, once we observed the same kinks in some wires produced in our experiments (Figure 4.31). Yet, the effect of mechanical disturbance has to be better understood.

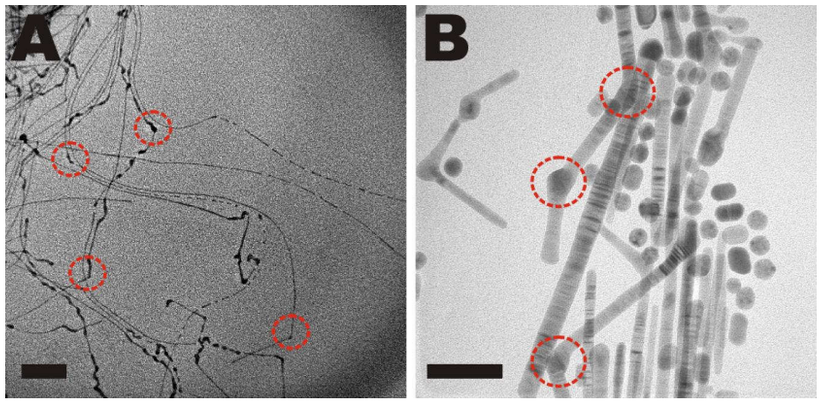

Figure 4.31. TEM image of (**A**) ultrathin and (**B**) thicker Au nanowires presenting kinked structures. The kinks are identified through the red dashed circles. The nanowires were synthesized as those described in Fig. 4.28C. The scale bar is 50 nm.

In summary, it was shown that oxidative etching promoted mainly by O_2 was crucial to the growth of ultrathin Au nanowires. It was found that saturating the reaction solution with O_2 led to both a more effective production of nanowires and an increase in their length. This is attributed to a growth mechanism based on an enhanced oxidation of twin defects on Au nanoparticles. Moreover, understanding the role of oxidative etching was crucial to significantly increase the yield of nanowires without adding any other reducing agent or nanostructure to the

solution as previously shown.[7,9,12] This simple O_2-assisted process was a new promising route for the rapid large-scale production of ultrathin single crystal Au nanowires and its findings opened the possibility to interconnect several device arrays in a single nanowire. Specifically, in this thesis the synthesis of long ultrathin nanowires was important because it enabled us to analyze their uniformity in terms of electrical properties in different points (lengths), which will be discussed in the next Section.

4.5 Assembly, Electrical Characterization and Surface Modification

The previous sections demonstrated that ultrathin Au nanowires presenting an aspect ratio of ≈ 4,000 could be obtained. The production of such ultralong nanowires was important for their electrical characterization because as it will be showed in the following Sections, it enabled the fabrication of devices based on resistors with different lengths. The results about assembly and the fabrication of these devices and their electrical characterization at room and at cryogenic temperatures are the next topics of the followings Sections. Furthermore, surface modification of Au nanowires with alkanethiol molecules and their electrical characterization in solution will be showed and discussed from Section 4.5.6. The findings of these data had an important contribution on the understanding of the electric transport in such ultrathin nanowires.

4.5.1 Assembling Nanowires

The investigation of the fundamental electrical properties of ultrathin Au nanowires as well as their technological application demands these structures to be organized with well-controlled orientation and density. Several methods have been developed in the rational organization of one dimensional nanostructures including shear force assisted assembly, electric field assisted assembly and also DNA template assisted assembly.[132-134] However, one of the main limitations is the scaling of these techniques to produce a large and mass production assembly of nanowires or nanotubes. Yu *et al.* demonstrated that a blown bubble film approach can overcome this limitation and semiconductor nanowires and carbon nanotubes could be assembled over large scaled silicon wafers and flexible plastic substrates.[135] Yet, the assembly of such nanostructures over specific positions on a substrate without cover other areas is difficult. To address this issue, Freer and co-workers employed a dielectrophoretic technique and showed that single semiconductor nanowires were highly and precisely assembled over 16,000 patterned electrodes sites.[136] The approach demonstrated by Freer *et al.* is certainly very promising, but relies on the suspension of nanowires in solutions with high dielectric constant such as aqueous media. It has been shown along this thesis that the surface of ultrathin Au nanowires was covered by a thin layer of oleylamine molecules remained from the synthesis, thus, implying that the nanowires presented a hydrophobic surface that makes them difficult to be dispersed in aqueous

solution. Surface modification of nanowires with other chemicals such as carboxyl or amino terminated alkanethiols would make the surface of nanowires more hydrophilic, however, the electrical properties of wires can strongly be affected and compromise their further application.

4.5.2 Assembly of Au Nanowires

Based on these observations, one alternative method for assembling nanowires is the shear force assisted assembly through a microfluidic approach.[137,138] Shear force is an internal force created in a material when an external force acts in the perpendicular direction to the longitudinal axis of the material.[139] It is a process commonly observed on nature when for example woods fall in a river and their alignment in the river's surface is driven by the river's stream. This basic idea was applied combining a microfluidic alignment with a surface patterning technique to assembly semiconductor nanowires that were suspended in ethanol solution on a silicon/silicon oxide platform.[138] In this thesis, it was employed a similar approach using a microfluidic channel to assembly the ultrathin Au nanowires that were dispersed in a hexane solution over a silicon/silicon oxide surface. This technique is relatively simple in comparison to other based on electric field assisted assembly and could be reliable applied to positioning the nanowires in certain positions on the substrate, as it will be shown and discussed ahead. The basic steps of experimental details are described in Section 3.3.

Figure 4.32A shows an illustration of the PDMS microfluidic channel for flow assembly of nanowires. The assembling process was performed by flowing a nanowires dispersion solution inside the channel. A representative SEM image showing the assembly and the alignment of Au nanowires along the flow direction is demonstrated through Figure 4.32B. From this micrograph some important features could be observed. First, it shows that the flow approach not only drives the alignment of nanowires, but also helps until a certain extension to individually separate the wires from each other. In fact, the strong van der Waals interaction among the nanowires precludes their total splitting. Second, some nanowires exhibit a misalignment with a small deviation with respect to the flow direction. This misalignment was mainly observed in ropes of wires that were not totally separate from each other, and it could be caused due to the splitting of wires from the ropes.

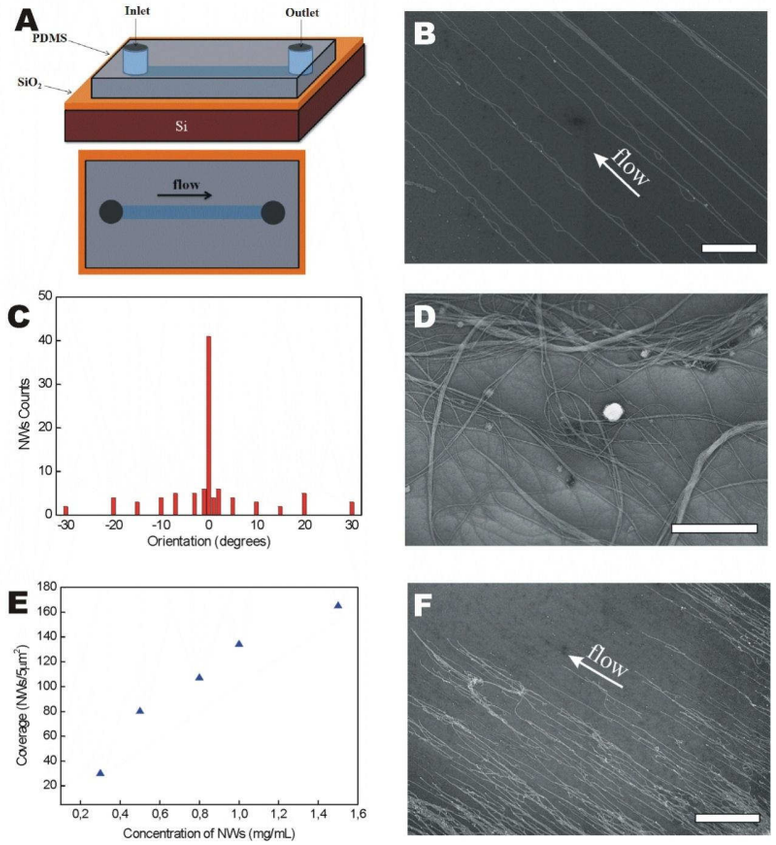

Figure 4.32. A – Illustration representing the fluidic channel structure used for flow assembly. The diagram in the top shows how the PDMS mold with the channel was brought in contact with a flat substrate and how the nanowires were assembled by flowing a nanowires suspension inside the channel. The diagram in the bottom illustrates a top view of the flow direction. B – SEM image of parallel arrays of Au nanowires aligned by channel flow. Scale bar is 1 μm. C – Histogram of nanowire angular distribution. D – A bundle of Au nanowires only dropped in the substrate. Scale bar is 1 μm. E – Coverage density of nanowires per 5 μm^2 as a function of nanowire concentration in the suspension. The coverage density was determined by counting the number of nanowires at areas of 5 μm^2 in the central part of the channel. F – SEM image of assembling of a high density of Au nanowires using the channel approach. Scale bar is 5 μm.

Thus, it suggests that a continuous flow of nanowires could even help to improve their splitting. Figure 4.32C depicts a histogram showing that most of nanowires straightly followed the orientation of the flow direction and the angular spread was relatively narrow. As a comparison to demonstrate the successful of the microfluidic approach to assembly the nanowires, Figure 4.32D shows an SEM micrograph of a bundle of ultrathin Au nanowires that were taken from nanowires solution used in the fluidic approach and only dropped over the substrate. The micrograph clearly shows that the wires overlap each other and form a random network on the substrate, thus, indicating that the flow approach can readily help to align the nanowires and separate them in organized parallel arrays. It was attempted to analyze also the density of nanowires covering the surface by flowing nanowire solutions with different concentrations. Figure 4.32E demonstrates that the density of nanowires assembled on the surface systematically increases with the increase of nanowires concentration in solution. Using high concentrated solutions, density of 160 nanowires/5 μm^2 could be achieved. Figure 4.32F shows a micrograph of a high density of Au nanowires assembled and aligned with respect to the flow direction. We note that for relatively high concentrated solutions of nanowires the density of coverage demonstrated through Figure 4.32E can together with the alignment of nanowires, be extended over the whole length of the microchannel.

4.5.3 Assembly Assisted Au Nanowires Device Fabrication

These results presented in Section 4.5.2, especially those regarding the high degree of alignment of nanowires and the possibility to split them from each other suggested that the microfluidic approach could enable the fabrication of devices such as resistors in a relative large scale. To demonstrate this, the flow approach was applied to assemble Au nanowires over the leads of the fabricated chips described in Section 3.3.1. Through the alignment of the microfluidic channel over the interdigitated leads, a high density of nanowires could be assembled over the leads following the flow direction, as demonstrated in Figures 4.33A and B. This assembly of nanowires resembles the typical crossbar devices used for switching application, where each bar (wire) represents an input connecting multiple bars (wires), which act as outputs.[140] As it has been demonstrated through Figure 4.32D, the density of assembled

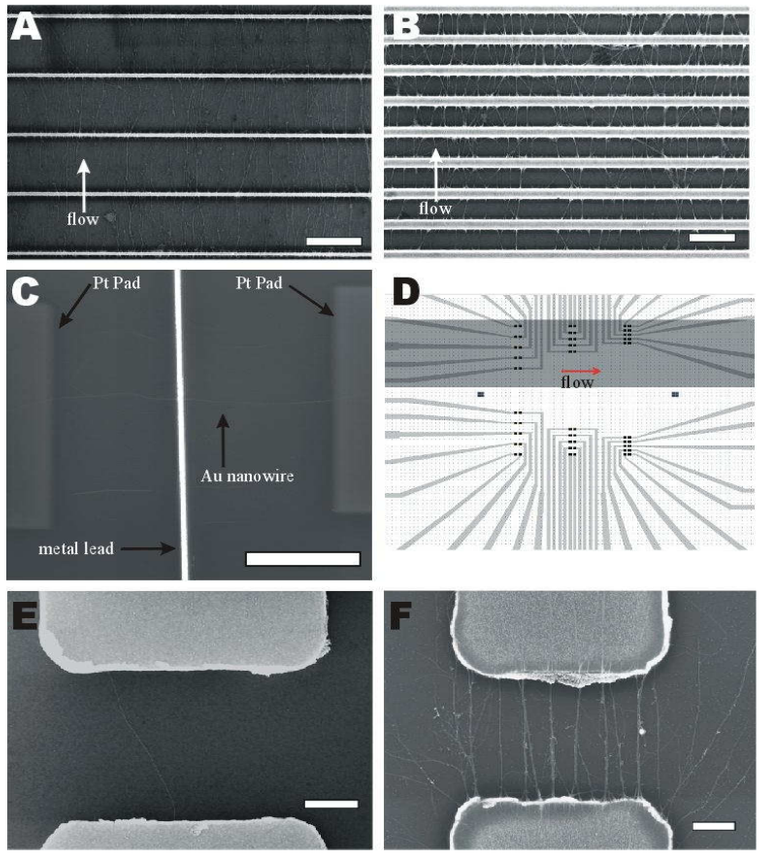

Figure 4.33. A and B– SEM micrographs of Au nanowires assembled over arrays of metal electrodes separated from each other by 5 µm and 1 µm, respectively. The flow directions are indicated by the arrows. The scale bars are 5 µm and 2 µm, respectively. C – SEM image of a Au nanowire crossing a single metal electrode and being connected by Pt pads in each side. The scale bar is 5 µm. D – Representation of microchannel arrangement over electrodes produced as described in Section 3.4.1, and the flow direction for alignment of Au nanowires. E and F –SEM images of a single and an array of Au nanowires assembled over the electrodes separated by 3 µm, respectively. Scale bars are 1 µm.

nanowires can be controlled by employing different concentrations of nanowire solutions. Figure 4.33C depicts a single Au nanowire connected by contact pads in the extremities and assembled over a lead, when a relatively low concentrated nanowires solution was applied in the flow channel. Although the electrical characteristics of this single hybrid crossbar was not measured, it demonstrates that more complex crossed devices can be produced using this simple and efficient approach.

The same methodology was also applied to assembly nanowires over the devices fabricated as described in Section 3.4.1. In this case, the microchannel was aligned over the area where the contact electrodes were produced as illustrated through Figure 4.33D. Figures 4.33E and F show two typical SEM micrographs of nanowires assembled on the contact electrodes, and as it can be observed until a certain extension the nanowires could specifically be assembled over the electrodes by following the flow direction. As it was already discussed, depending on the concentration of nanowires solution, different densities of nanowires and/or ropes of nanowires could be assembled on the electrodes. We note that the nanowires not only assembled over the electrodes, but also strongly adhered to them and could not be easily washed out. Indeed, most but not all nanowires could be removed from the electrodes after assembling, when the chip was dipped in chloroform, which was the solvent that could better wash out most of nanowires. This ability of chloroform to remove out the nanowires from the contact electrodes is attributed to its interaction with oleylamine molecules capping the nanowires as demonstrated in Section 4.1.1. This interaction could reduce the adhesion forces between nanowires and metal contacts and consequently move out the wires from the electrodes. It is worth pointing that during the flowing process, nanowires were also assembled over the leads, however, as the separation distance between parallel leads is longer than the length of nanowires, no cross-talking between the leads was observed. The process of assembling and alignment of nanowires over these electrodes as showed in Figures 4.33A, B, E and F assisted the fabrication of devices that could now be electrically characterized and further applied for sensing, as it will be demonstrated in the next Sections.

4.5.4 Electric Characterization of Au Nanowires at Room Temperature

Based on the findings that the flow approach helps to split the wires from each other, it was attempted to characterize the electrical transport from single ultrathin Au nanowires by assembling them individually over arrays of electrodes as those shown in Figures 4.33A and B and also over electrodes produced by microcontact printing.[141] A single ultrathin nanowire exhibiting a diameter of 5 nm and assembled over an array of Au electrodes produced by microcontact printing is shown in Figure 4.34A. Electrical characterization of this nanowire was performed by measuring two-point probe current–voltage curves starting from the two first electrodes from left to right. Figure 4.34B demonstrates that the I–V curve of nanowire exhibits a typical ohmic behavior. The resistance of the nanowire was calculated from the least square method and the value found was 2.23 kΩ (R^2=1). Considering that the nanowire has a cylindrical shape and exhibits a diameter of 5 nm and a length of 154 nm between the two electrodes, the correspondent electrical resistivity calculated was 284 Ω.nm. These values are in satisfactory agreement with those already reported on literature for ultrathin Au nanowires produced in a similar manner (Table 4.3).

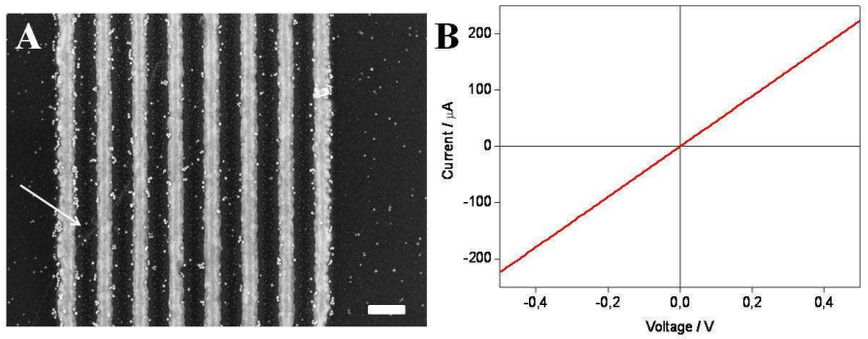

Figure 4.34. A – SEM image of an ultrathin Au nanowire (indicated by the arrow) assembled over an array of Au electrodes (leads). The scale bar is 200 nm. B – Current versus voltage characteristic of the respective nanowire showed in A.

Table 4.3. Comparison between the electrical resistance of nanowires measured in this work and other produced in the same way and reported in literature.

Nanowire Diameter (nm)	Length (nm)	Resistivity (Ω.nm)	Reference
9	450	260	8
7	150	290	142
5	154	284	Measured in this work

Taking into account that in all the cases exhibited in Table 4.3, the resistivity of nanowires was calculated from two-point probe measurements and the contact resistance was not corrected, this relatively small difference observed in the resistivities can be mainly attributed to the measurement approaches employed in each case. For example, Wang et al. (ref. 8) used electron beam lithography to deposit the leads on top of a Au nanowire assembled on a Si/SiO_2 substrate, whereas Lu and co-workers (ref. 142) performed the cold welding of two ultrathin Au nanowires inside of a TEM and sequentially measured the current–voltage characteristics. In our case, the nanowire was assembled on top of the leads. As it has been introduced in Section 2.4, the resistance of nanowires tends to exponentially increase decreasing the nanowires diameter, and in fact as observed through Table 4.3, we measured a nanowire with the smallest diameter and the highest resistivity. However, it is difficult to compare size effects in the electrical properties of Au nanowires because the measurement approaches employed in each case were different, and as it will be discussed ahead contact resistance plays an important role in the intrinsic electrical transport of these nanowires.

During electric measurements, a non-linear behavior in the I–V curves of some wires was observed (Figure 4.35A). We could turn this behavior from non-linear to linear by biasing the nanowires with relatively high voltages (from -5 V to 5 V) as demonstrated through Figure 4.35B. The same non-linear behavior in the electric characteristics of polycrystalline Au nanowires was reported by Lilley and Huang, who associated it with impurities adsorbed on the surfaces of wires.[143] In our case, it was shown and discussed in Section 4.3 that oleylamine molecules are difficult to be removed and stay adsorbed on the surface of Au nanowires. The adsorption of these molecules could also be observed from scanning tunneling microscopy (STM) analysis, which was conducted in a constant current mode and demonstrated a voltage drop when the tip scanned the surface of a nanowire (Figure 4.35C). This voltage drop also indicates that the surface of the nanowire was covered by non-conductive species. Indeed, as

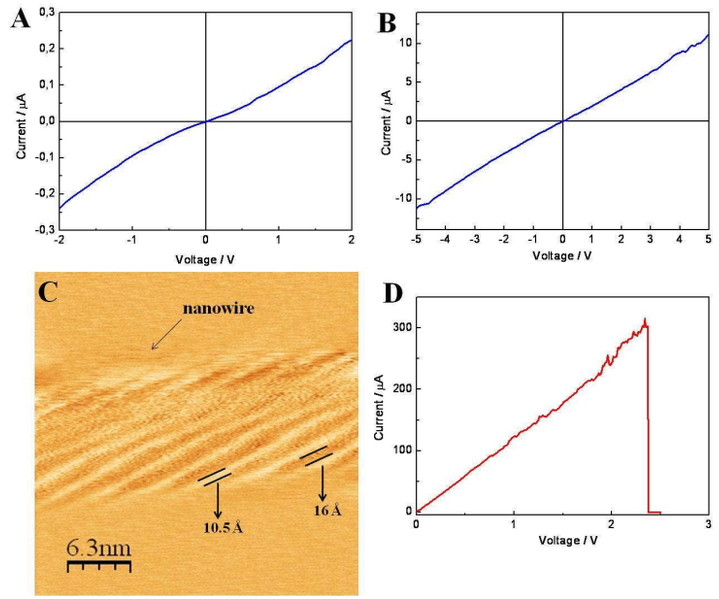

Figure 4.35. Room temperature electric characteristics of ultrathin Au nanowires presenting non-linear (A) and linear I–V behavior (B) after biasing at relatively high voltages. C – STM image of an Au nanowire recorded in a constant current mode. D – Breakdown I–V characteristic of the 5 nm diameter Au nanowire.

demonstrated through Figure 4.35C some patterns exhibiting widths of ≈10.5 Å and ≈16 Å and that are thought to be the oleylamine molecules, were observed. These values were very close to those found for x-ray analysis of the whitish gel reported in Table 4.2. This finding strongly supports the idea that the non-linear I–V characteristic observed for some of our nanowires was due to the thin layer of oleylamine molecules that were assembled on the surface of the nanowires. The adsorption of these molecules can generate a strong barrier for electrons tunneling between the leads and the nanowires, thus, resulting in a relatively high contact resistance that can lead to the non-linear I–V behavior observed. By applying high voltages from the contacts, the Joule heating could help to remove the organic molecules from the junction areas and electrons could easily tunnel between the leads and the nanowires.

Relatively high voltages could be applied to the nanowires as long as the current level did not exceed about 300 μA, which was the limit where the current usually brokedown (Figure 4.35D). For the nanowire presenting a 5 nm diameter and analyzed previously, this level of current yielded a failure current density of approximately 10^{13} A/m^2. This value is much higher than those found for bulk metals, which the current densities are usually in the order of $10^7 - 10^8$ A/m^2.[144] Also, it is higher than in polycrystalline Au nanowires that were produced from either lithography or DNA template and exhibited diameters from 60 to 800 nm and had breakdown current densities of 1 x 10^{12} A/m^2.[145,146] Additionally, this measured value is higher than that of 3.5 x 10^{12} A/m^2 reported by Wang *et al.* for a 9 nm diameter ultrathin Au nanowire.[8] Breakdown currents are often associated with the phenomenon of electromigration, which is a thermally-assisted process for moving ions under the influence of an electric field. When a relatively high electrical current pass through a wire, it heats up the wire and the metal atoms become more mobile and can move in the opposite direction of the current flow (electron wind).[144] Taking into account that the external circuitry connecting the wire is significantly larger than the wire, the current density in it is much smaller than in the wire, thus, less heating occurs at the contacts and they act as heat "sinks". As a consequence, the atoms that move along the wire are not replaced at the ends at the same rates as they leave, and voids form at the negative end, where the thermal gradient is a maximum. This void eventually merges and current failure occurs. This mechanism of breakdown current can usually be applied to explain failures in polycrystalline nanowires, which present grain boundaries.[147] However, in our case the ultrathin nanowires are free of grain boundaries and void diffusion, so that the mechanism of electromigration can be ruled out. Size effects could instead be considered to explain the high failure current density observed here. For example, decreasing the diameter of the nanowire increases its surface-to-volume ratio and consequently increases also its contact area, which helps the nanowire to dissipate the heat from the electrical stress more efficiently and carry high current densities. Another factor that should be considered is the electron-phonon scattering length that is of the order of 170 nm in Au.[147] For nanowires with diameter much less than 170 nm, the excitation of lateral phonons to wire axis is inefficient and the lattice heating is reduced. This reduction means that the electron-phonon scattering is also reduced and failure currents should occur at higher current densities. These effects could help to explain the high current density observed, but further experimental investigation and explanation to elucidate the mechanism of failure current is needed.

4.5.4.1 Contact Resistance of Au Nanowires

We attempted also to investigate the resistance of nanowires as a function of their length. For this purpose, ultrathin Au nanowires were assembled over an array of 8 electrodes separated by equal distances in a way such that the same wires were in contact with all the eight electrodes simultaneously (Figure 4.36A). In this manner, I–V characterization with different distances for the nanowires was performed and the resistance for each distance could be obtained. Figure 4.36B depicts the dependence of the electrical resistance as a role of the length for a rope of nanowires assembled over the electrodes. For short distances until 1.3 µm, the resistance of the nanowires exhibited a small increase with a linear dependence on the length. Although a small group of wires instead of a single nanowire was measured, we note that the resistance for nanowires between parallel electrodes was significantly similar to that measured for a single nanowire. The resistance for nanowire devices as that demonstrated in Figure 4.33F with distances larger than 2 µm was also measured and it was observed that the resistance systematically and drastically increased with the length, Figure 4.36C. Depending on the number of wires in the rope, electrical resistance in the order of a few megaohms could also be observed. This small increase in the electrical resistance of nanowires with the increase of length indicates that the contact resistance has a significant contribution in the total resistance measured. In fact, the total resistance (R_T) in a 2-probe configuration can be expressed as:

$$R_T = R_{cr} + R_i \qquad \text{(Eq. 4.3)}$$

where R_{cr} represents the contact resistance and R_i is the intrinsic resistance of the nanowires. By extrapolating the linear portion of the lengths to the resistance axis in the Figure 4.36B, we obtained the value of 1.64 kΩ for the contact resistance. Considering that the total resistance measured for parallel electrodes was 2.23 kΩ, using the equation 4.3 we could calculate the intrinsic resistance of the nanowires as 590 Ω. Assuming that this resistance is similar for a single 5 nm diameter nanowire with a length of 154 nm, the calculated intrinsic resistivity for this nanowire is 7.5 µΩ.cm. This value is about 3.4 times higher than that for the resistivity of bulk Au (2.2 µΩ.cm).[148] Several numerical models, including the one from Chamber and also the one from Sondheimer have made approximation for an exponential increase in the resistance of

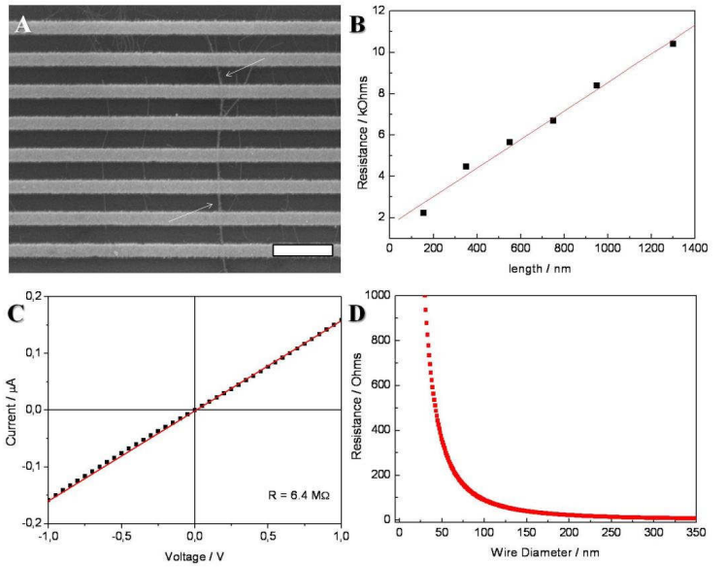

Figure 4.36. A – SEM image showing the assembly of a rope of Au nanowires (indicated by the arrows) crossing an array metal electrodes. Scale bar is 500 nm. B – Electrical resistance as function of the length for the respective rope of nanowires showed in A. C – I–V characteristic for a rope of nanowires assembled over electrodes separated by 3 μm, as that showed in Figure 4.33F. D – Calculated resistance increase versus shrinking diameter of a Au nanowire having a bulk resistivity of 2.2 μΩ.cm.

metals with the decrease of their diameter.[149] It was calculated the change in resistance with shrinking the diameter of a Au nanowire presenting a length of 32 μm and having a bulk resistivity of 2.2 μΩ.cm, as demonstrated through Figure 4.36D. These data clearly exhibits the exponential and pronounced increase in the resistance of nanowire when its diameter is decreased, just as described through the models of Chamber and Sondheimer and in several other works.[147,149] From this calculated data it can be observed that the intrinsic resistance (590 Ω) found from our experimental data should correspond for a nanowire of 39 nm of diameter. This observation is consistent with our SEM analysis for the diameter of the rope of nanowires crossing the electrodes. For a 5 nm diameter Au nanowire, as it was showed before, the

resistance using these data should be much higher. However, it is important to point out that the calculated data correspond for polycrystalline nanowires, which the resistance as discussed previously are higher than that found for our single-crystal nanowires.

This exponential increase in resistance with decreasing the diameter of nanowires that are free of grain boundaries is mainly attributed to the effects of electron scattering on the surface. As the surface-to-volume ratio increases to nanowires with small diameters, the electrical conduction in the nanowires is dominated by surface atoms. If the nanowire presents a diameter much shorter than the mean free path of electrons (for Au, ≈ 80 nm) in the metal, the effects of surface scattering due to electron diffusion and/or adsorption of impurities become dominant and the resistance is drastically affected.[62]

The findings pointed in this Section revealed that some intrinsic electrical properties of ultrathin Au nanowires were limited by contributions of contact resistance. As the physics of contacts represents an important barrier for further fundamentals studies of such ultrathin nanowires as well as their technological applications, it was essential to analyze the electrical characteristics of these nanowires at a low range of temperatures, as it will be described in the next Section.

4.5.5 Electric Characterization of Au Nanowires at Low Temperatures

In order to investigate the influence of contact resistance in the electrical transport of ultrathin Au nanowires, I–V characterization from low to near room temperature (from 0.55 K to 200 K) range employing samples prepared as described in Section 3.3.1 (Figure 4.37A) and presenting a relatively high contact resistance was performed. Figure 4.37B exhibits I–V curves of a representative bundle of Au nanowires measured at different temperatures using a two-probe method. The linear ohmic behavior for nanowires having a resistance of ≈ 9 MΩ is clearly visible at room temperature. When the temperature was reduced a transition from quasi-linear to non-linear I–V characteristics was observed. This change in electrical behavior with the decrease of the temperature markedly implies in a strong potential barrier imposed by the contact resistance. The insert of Figure 4.37B demonstrates an example of an Arrhenius curve (log conductance versus 1/temperature (T^{-1})) plotted for the nanowires biased at 0.1 V.

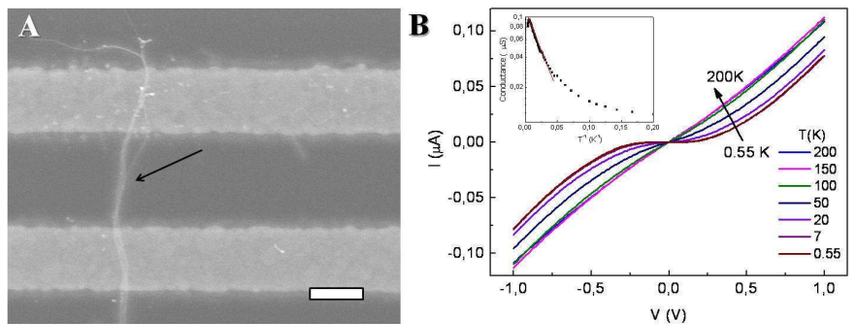

Figure 4.37. A – SEM image of a rope of Au nanowires (indicated by the arrow) crossing an array of Au electrodes. The scale bar is 200 nm. B – Current versus voltage behavior of Au nanowires in different ranges of temperatures. The inserted Figure shows a plot of log conductance as a function of T^{-1} for the nanowires biased at 0.1 V. The straight line indicates the thermal activation conduction.

An enhancement in the conduction of the structure near room temperature is clearly visible and indicates a thermally activated transport mechanism above the junction barrier. For temperatures below 10K, a characteristic transition from activated transport to temperature-independent behavior is observed. The tunneling of electrons into and out of the nanowires in such system was already introduced in Section 2.4.1 and can be described through a metal-insulator-metal (MIM) model as illustrated in Figure 4.38.

The tunneling rate across a MIM junction depends exponentially on the insulating barrier thickness (w), the zero field barrier height (φ_o) and the small surface area (A_J) of the junction. This tunnel junction can also be interpreted as a parallel-plate capacitor with a capacitance described as $C_J = \varepsilon_r\varepsilon_0 A_J/w$, where ε_r corresponds to the dielectric constant of the insulating barrier and ε_0 is the vacuum permittivity. Under biasing, the barrier potential across the junction is a sum of $V_J + V_T$, where V_J is the voltage across the junction due to the applied voltage and V_T is the voltage fluctuation (also called thermal noise) due to random thermal motion of electrons in the conducting regions.[64,150]

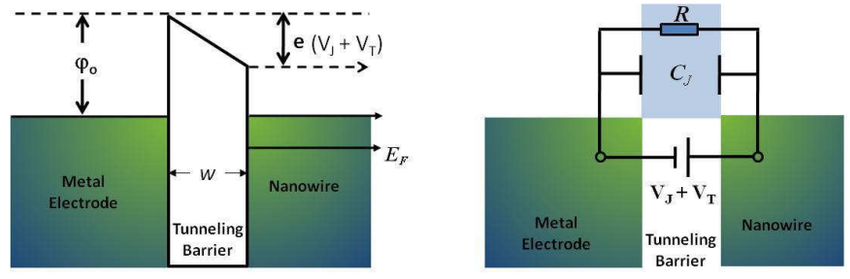

Figure 4.38. Representation of energy diagram for electrons tunneling a barrier potential under a bias $V_J + V_T$ (left Figure) and an equivalent *RC* circuit of the junction (right Figure).

Because the total capacitance of the metal contacts is much larger than C_J, the thermal voltage fluctuation can be approximated by $V_T^2=\kappa_B T/C_J$, where κ_B is Boltzmann's constant and T the absolute temperature. From these considerations and as expected from the nanowire-metal contact junction, it is implicit that C_J is very small, and thus, thermal fluctuations in the density of free electrons near the junction induce strong voltage fluctuations across it.

Fluctuation induced tunneling (FIT) in junctions presenting a small C_J is correlated with a strong deviation of conductivity from the Ohm's law at temperatures under the thermal energy ($\kappa_B T$).[150,151] At temperatures where $\kappa_B T$ exceeds the charging transfer energy per electron, V_T can increase the tunneling currents with temperature by reducing the thickness and height of the barrier due to the superposition of applied and thermally generated electric fields. This thermally activated conduction process was described by Sheng and co-workers, who proposed that conductivity (σ) dependent on temperature for junctions where C_J is small can be given by[152]

$$\sigma(T) = \sigma_0 exp^{\frac{-T_1}{T_o+T}} \qquad \text{(Eq. 4.4)}$$

where σ_0 can be treated as a constant that weakly depends on temperature, while T_1 and T_o are two new characteristic parameters that correspond to the energy required for an electron to cross the barrier and the temperature well below which thermal fluctuation effects become insignificant. Both can be defined as

$$T_1 = \frac{8\varepsilon_o}{e^2\kappa_B}\left(\frac{A_J\varphi_o^2}{w}\right) \quad \text{(Eq. 4.5)}$$

and

$$T_o = \frac{16\varepsilon_o\hbar}{\pi(2m)^{1/2}e^2\kappa_B}\left(\frac{A_J\varphi_o^{3/2}}{w^2}\right) \quad \text{(Eq. 4.6)}$$

where ħ is Planck's constant and m is the mass of the electron. The FIT model described by Sheng and *et al.* was first applied to explain the tunneling conduction in disordered granular carbon-polyvinylchloride composites.[150,152] Recently, it was also employed by Lin and co-workers to describe the electron transport from metallic nanowires through an insulating contact barrier separating the nanowires from the metal contacts, which is a reasonable situation for FIT due to the small capacitance formed in the junction.[151]

To analyze this transport mechanism of nanowires/metal electrodes, differential conductivity as a function of the applied bias voltage was used (Eq. 4.7).

$$\sigma = \frac{dI}{dV} \quad \text{(Eq. 4.7)}$$

where I is the current through the sample and V is the bias voltage applied to the sample. Differential conductivity was derived from I-V curves using standard numeric curve differentiation. The differential conductivity versus voltage curves plotted for different temperatures (Figure 4.39A) for the same rope of nanowires showed in Figure 4.37A exhibit a suppressed tunneling at around 0 V. At relatively high bias in different temperatures all the curves fall onto a single curve. Figure 4.39B shows the differential conductivity plotted as a function of temperature at different bias voltages. It can be clearly seen, that in these curves three regions with different temperature behavior can be found. Below these regions will be described in detail. At low-temperatures (in the range from 0.55K to 7K), the first region shows weak dependence of the conductivity on temperature which reflects the elastic tunneling mechanism of conductivity. The second region in the range from 7K to 100K (Figure 4B) demonstrates a strong temperature dependence. The third temperature region (Figure 4B), above 100K, demonstrates non-monotonous behavior. At least two competing mechanisms of conductivity can be considered. At higher temperature range, the decrease of conductivity with increasing temperature reflects a metallic type of conductivity.

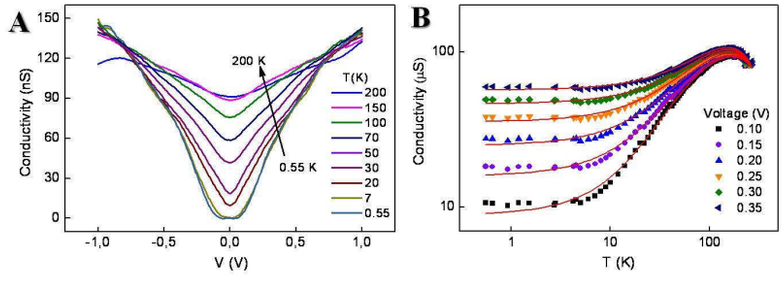

Figure 4.39 A – Conductivity of the sample derived from Figure 3B. B – Sample conductivity plotted versus temperature at different bias voltages. The symbols correspond to the experimental data, whereas the solid curves are the least-squares fits to Equation 4.8.

In the lower temperature range, with the FIT mechanism the conductivity increases with increasing temperature. These two mechanisms compete in the third temperature region. As can be seen, in the Figure 4B at a temperature of about 100K these two mechanisms result in a well-resolved maximum in the characteristics. Thus, to fit the measured dependences of the conductivity on temperature we used the FIT model (Eq. 4.8) and modified it by taking into account the contribution of the metallic conductivity, which causes a quasi-linear decrease of the conductivity with increasing temperature:

$$\sigma(T) = \sigma_0 e^{\frac{-T_1}{T_0+T}} - \beta T \qquad \text{(Eq. 4.8)}$$

in this case, β is a certain temperature coefficient, which plays the role of a fitting parameter in the model. The parameters extracted from the fitting of the curves shown in Figure 4.39B by Equation 4.8 and the values of the effective barrier thickness and height calculated using the system of Equations 4.5 and 4.6 are listed in Table 4.4.

Table 4.4. Parameters extracted from the least-squares fits to Equation 4.8 in curves shown in Figure 4.39B and also calculated from Equations 4.5 and 4.6.

Voltage / V	σ_0 / µS	T_1 / K	T_0 / K	T_1/T_0	*w* / nm	φ_o/ meV	β / nS/K
0.1	0.32±0.01	116±3	32±1	3.63	4.9±0.5	33±3	0.51±0.02
0.15	0.35±0.02	130±3	42±1	3.1	4.3±0.5	33±3	0.57±0.02
0.2	0.4±0.03	148±4	53±1	2.79	3.8±0.4	33±3	0.65±0.03
0.25	0.48±0.03	175±5	67±1	2.61	3.5±0.4	35±4	0.76±0.03
0.3	0.6±0.03	212±6	83±1	2.55	3.3±0.4	37±4	0.92±0.04
0.35	0.75±0.04	251±6	97±1	2.59	3.2±0.3	40±4	1.1±0.05

The obtained data showed that the ratio T_1/T_0 decreased in sequence with the increase of voltage applied during the measurements. This observation is in agreement with the FIT theory, which predicted that the probability of electron tunneling through a barrier increases by increasing the externally applied electric field.[150,152] Thus, it means that a larger ratio T_1/T_0 implies a stronger temperature behavior of the contact resistance. These data reflected also in the fitted values of *w* and φ_o. In the case of barrier width, the values of *w* decrease with increasing bias voltage, which can be explained by the changing shape of the potential barrier under the influence of the applied field (Poole-Frenkel effect, mirror effects[153]).

It should be noted that the determined values of *w* are slightly larger than the observed thickness imposed by oleylamine molecules adsorbed on the surface of nanowires. Moreover, the values of φ_o were also several tenths of meV as is usual for barrier heights. These values found for *w* and φ_o are consistent with parameters of molecules physisorbed on the surface of Au nanowires.[154] In this case, van-der-Waals forces are responsible for the intermolecular and Au nanowires/molecules interactions. Although these interactions are relatively weak, they have a significant influence on molecular self-assembly of organic molecules presenting long alkane chains.

One important parameter to be taken into account is the junction area. In our calculations we used the value of the effective contact area, A_J. The maximal value of this parameter, estimated from the SEM image (Figure 4.37A) is about 4000 nm^2. However, owing to the round

shape of the nanowires and their surface non-uniformity due to adsorbed organic molecules the effective contact area is considerably smaller. Concerning this problem, Kogut et al. showed that due to the roughness and the fractal nature of the surface, the real contact junction area can be much smaller, sometimes only ≈1% of the apparent calculated contact area.[155] Taking into account the small dimensions, the flexibility and shape of the Au nanowires, these observations about the real contact junction demonstrate that they can vary from those observed on the in-plane micrograph and it should be always taken into account in the investigation of transport in bottom-up processed nanostructures. Therefore, the effective junction area in this case is about A_J=100 nm^2. At the same time, the effective junction area A_J has quite a weak influence on the magnitude of the values of *w* and φ_o. The estimations show that variations in the value of A_J from 100 nm^2 to the maximum possible value of $A_J \approx 2000$ nm^2 taken from the SEM picture affect the magnitude of thickness of the insulating barrier as well as the zero field barrier height in such a way that they may change their magnitude no more than twofold. Concerning the barrier height, its value is about the value of k_BT at a temperature of 270K. This fact allows realization of quasi-linear I-V characteristics, which is in good agreement with measured data.

In summary, it was found that in the electronic contacts at the interface between Au nanowires and metal electrodes, where the contact resistance has a significant influence in the electronic transport, the physics of contacts could be satisfactorily explained in terms of the thermal fluctuation induced tunneling theory. The results indicated that the contact junction areas play a strong influence in the potential barrier of tunneling, suggesting that for electrical characterization of these wires in solution and their further application as chemical sensors, the contact areas should be isolated and protected from the liquid. Based on these findings, the next Sections will present the results about electrical behavior of Au nanowires in salted solution and after chemical modification of their surface with alkanethiols.

4.5.6 Probing Electrical Characteristics of Au Nanowires in Solution

It was demonstrated through Sections 4.5.4 and 4.5.5 that the contact resistance plays a dominant role in the electric characteristics of ultrathin Au nanowires. Thus, in order to investigate the electrical behavior of devices based on Au nanowires in solution and avoid the interference of further effects on the contact junctions, the feed lines and the contact areas with

the Au nanowires devices were passivated with PMMA, leaving only a fraction of nanowires and the external contact pads exposed to the air. The preparation of such devices was described in Section 3.4.1. The following section will describe the electrical behavior of nanowires in salted solutions.

4.5.6.1 The Effect of Ionic Strength on Surface Charging of Au Nanowires

The electrical characteristics of bundles of Au nanowires devices were analyzed in solutions with different concentrations of NaCl. Table 4.5 exhibits the employed concentrations, as well as their ionic strength and the correspondent Debye length calculated using Equation 2.8 for each solution. As NaCl is an ionic binary compound where each ion is monovalent, the ionic strength of its solution has a direct relation of 1:1with the concentration of the solution. Figure 4.40A shows I – V curves of Au nanowires device submerged in different concentrations of NaCl. For clarity, only the curves measured in water (measured before salted solutions), NaCl 10 µmol L^{-1} and NaCl 10 mmol L^{-1} were depicted. In general, two main features can clearly be observed from this Figure. First, the I – V curves presented a NaCl concentration-dependent hysteresis, and second, under salted solutions the curves became non-linear and the resistance of nanowires increased in comparison to those measurements performed in water only.

Table 4.5. Concentration of NaCl used to analyze the electric behavior of Au nanowires in salted solution and the correspondent ionic strength and Debye length.

Concentration / mmol L^{-1}	Ionic Strength / mmol L^{-1}	Debye length / nm
0.01	0.01	75.4
0.1	0.1	23.9
1	1	7.7
5	5	3.4
10	10	2.4

The observed hysteresis was more pronounced increasing the NaCl concentration and its origin is associated with the adsorption and rearrangement of ions in the electrical double layer formed on the interface with the nanowires, as introduced in Section 2.5.1. The adsorption of ionic species on the surface of nanowires, specially Cl^- ions because cations such as Na^+ are more

easily hydrated and are retained in solution, results in a capacitance due to the electric double layer and a resistance due to the charge transfer resistance in each ion-metal interface, as illustrated in Figure 4.40B. Li and co-workers analyzed the interactions of Cl^- ions (from NaCl) on a platinum electrode and observed that the capacitance of the electrode was proportional to the Cl^- ions concentration.[156] Because of the larger surface-to-volume ratio, this increase in the capacitance of the double layer due to ions adsorption can readily be enhanced in nanostructures.

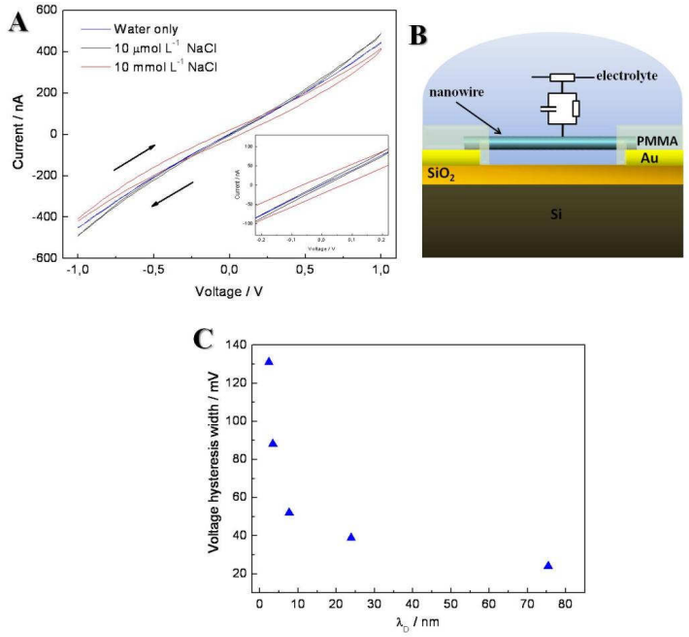

Figure 4.40. A – Current versus voltage for a rope of Au nanowires submerged in solutions of NaCl with different concentrations. The inserted Figure shows a zoomed image of the I–V behavior near 0 V. B – Equivalent circuit model for adsorption of ions on the surface of Au nanowires. Between the electrolyte and each conducting element there is a capacitor due to the electric double layer and a resistor due to the charge transfer barrier. C – Voltage hysteresis width of the I–V curves showed in A versus Debye length generated for each concentration of NaCl.

Figure 4.40C shows a plot of the hysteresis width in voltage as a role of the Debye length for each concentration of NaCl employed. It could clearly be observed that the hysteresis increased exponentially decreasing the Debye length and this tendency was more evident when the Debye length reached a value comparable to the diameter of the ultrathin nanowires. This effect is well known and it is attributed to the compression of the double layer and increase of the electrical potential gradient with the increase of the ionic concentration.[66,67]

These observations imply that the adsorption of small ionic species on the surface of nanowires can directly influence their surface charging, and this effect is more pronounced in electrolyte solutions with relative high ionic strength, where the Debye length is comparable to the dimensions of the nanowires. These results instigate a question regarding the effect of a more complex situation in the electrical characteristics of nanowires, that is, the adsorption of molecules with different charges on their surface. This question is the topic of the next Section.

4.5.6.2 The Effect of Surface Modification of Au Nanowires in their Electrical Properties

In Section 2.5.2 it was introduced how the electron transport properties of ultrathin metal nanowires can be affected due to the adsorption of molecular species on their surface. Covalent immobilization of organic ligands on the nanowire surface provides a mean to further tune the properties of this one-dimensional nanosystems. In the previous Section, it was demonstrated that the adsorption of different concentrations of ionic species on ultrathin Au nanowires can charge their surface and consequently change their electrical resistance. In this Section, this part of the work focused in the investigation of the effect of immobilizing alkanethiol molecules with different functional groups on Au nanowires and their electrical characteristics in aqueous media. The samples used in these experiments were also prepared as described in Section 3.4.1, with the contact areas where the nanowires were assembled in the pad electrodes passivated with PMMA to avoid influence of contact junctions.

The chosen molecules for immobilizing on Au nanowires were thiolpropane (TP), cysteamine (CA) and mercapto-propionic acid (MPA). The chemical structures of these molecules are depicted in Figure 4.41A.

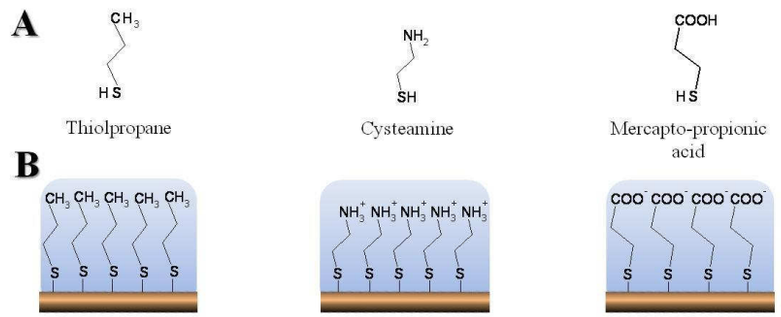

Figure 4.41. A – Chemical structure of the alkanethiol molecules used for immobilizing on the surface of Au nanowires. B – The respective molecules immobilized on Au nanowires and their correspondent expected ionization in aqueous solution with pH near 7.

The experimental conditions for their immobilization on the surface of Au nanowires were described in Section 3.5.2. The choice of these molecules was firstly based on the thermodynamically favorable covalent interaction of thiol functional group with Au and consequent formation of self-assembled monolayers (SAMs) on its surface.[157] Secondly, due to their short and similar lengths that are in the range of 4–6 Å, and also due to the charge of their functional groups when the molecules are in aqueous media near pH 7.0.[158,159] In this case, the immobilization of MPA molecules on Au nanowires could generate a net of negative charges due to deprotonation of their carboxyl groups, while on the other hand CA could yield a positively charged surface due to protonation of their primary amine groups and TP would serve as a non-charged or neutral molecule (Figure 4.41B).

Figure 4.42A shows a representative SEM micrograph of a typical rope of Au nanowires device employed in these experiments. Before the surface modification, the devices exhibited a linear ohmic behavior with an initial electrical resistance in water of 5–10 MΩ (measured in 2 probe method with contact resistance not corrected). After immobilization of alkanethiol molecules on Au nanowires using ethanolic solutions with different concentrations of these

species, I – V curves of the devices submerged in pure Milli-Q water (18 MΩ, pH 6.7) were recorded in a sweeping mode and are depicted through Figures 4.42B-D.

The measured curves for these three cases show some common general aspects. For instance, in all the cases the nanowire devices presented a systematical increase in the electrical resistance with increasing the concentration of alkanethiols solution. This effect was observed even when concentrations as low as 10 µmol L^{-1} were employed. Another remarkable common aspect observed was the transition from linear to non-linear I – V curves when alkanethiols were immobilized on the nanowires surface. Also, as already observed before when the nanowires were exposed to salted solutions, the measured curves after the immobilization of the molecules exhibited hysteresis. The hysteric effect was more pronounced on those nanowire devices where MPA was immobilized. Previously, it was shown that the surface of ultrathin Au nanowires analyzed in this thesis was covered by oleylamine molecules remaining from the synthesis and their removal was difficult to be performed. On the other hand, these observations about the change in electrical resistance when the nanowires were exposed to alkanethiol solutions strongly indicated the binding of these thiol molecules on the surface of Au nanowires. From this pre-overview, three fundamental questions could be raised:

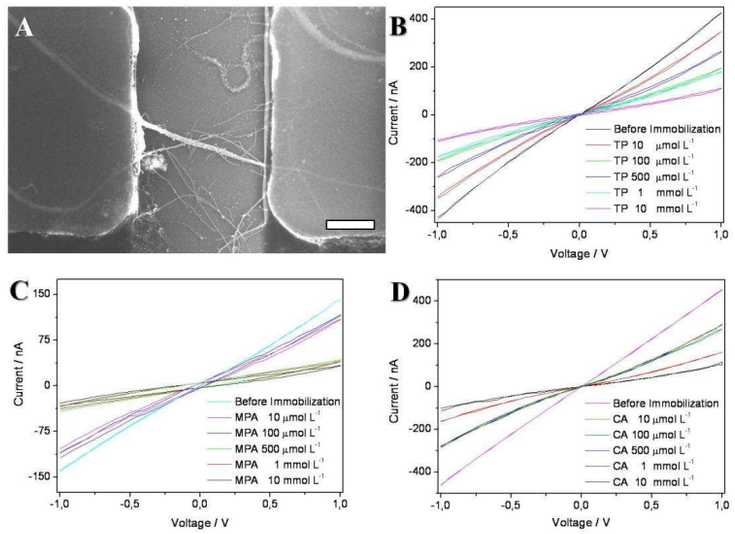

Figure 4.42. A – SEM image of a representative passivated Au nanowires device employed for immobilizing alkanethiol molecules. Scale bar is 1 µm. B – D, I–V characteristics in aqueous solution of Au nanowires devices before and after their surface modification with variable concentrations of thiolpropane (TP), mercapto-propionic acid (MPA) and cysteamine (CA), respectively.

1) How the binding of thiols contributed to the increase in the electrical resistance of the nanowires ? 2) Was there any relation between the increase of resistance and the charges from the functional groups of the immobilized molecules ? 3) Why the I – V curves changed from linear to non-linear with the binding of alkanethiol molecules ?

The change in resistance of ultrathin metal films was introduced in Section 2.4 and the same mechanism was also extended to ultrathin metal nanowires. In the case of nanowires, specially those that are ultrathin, most of atoms are on the surface and as their lateral dimensions are much smaller than the mean free path of conduction electrons (for Au, ≈ 80 nm), their surface contributed significantly to the electron scattering and to the nanowires resistance. It means that the adsorption or the binding of molecules to the surface of such nanowires can drastically affect the conduction electrons, increasing their scattering and consequently also their electrical resistance, as it was observed in Figures 4.41 and 4.42B-D. This description helped

partly to explain the observed results based on the first raised question, but still needs further complements, specially regarding the second question. A more complete model to describe the effect of adsorbates onto a thin metal film was developed by Persson, who reported the diffuse scattering of carriers on surfaces which invoked the electronic structure of the adsorbate and metal in a natural way.[160] Persson proposed that the resistance increase ($\Delta\rho$) due to adsorption of species on thin metal surfaces can be given by:

$$\Delta\rho = \frac{M\, n_a}{n^2 e^2\, d\tau} \qquad \text{(Eq. 4.9)}$$

where M and n_a are the adsorbate mass and number density, respectively, n correspond to the electron number density in the film, while e is the electron charge. The parameters *d* and $1/\tau$ are the film thickness and the adsorbate vibrational damping rate due to excitation of electron-hole pairs, respectively.[160] In this model, the critical parameter is the adsorbate density of states at the Fermi energy, $N(E_F)$, which is linearly related to the damping rate through[158,159]

$$\frac{1}{\tau} = \frac{2m\omega_F\Gamma}{M} N(E_F)\langle\sin^2\theta\rangle \qquad \text{(Eq. 4.10)}$$

in this case m corresponds to the electron mass, $\hbar\omega_F = E_F$ is the Fermi energy, whereas Γ is the width of the adsorbate density of states, and $\langle\sin^2\theta\rangle$ is a geometrical factor that depends on the orbital symmetry of the adsorbate molecular orbital near E_F. Combining Equations 4.9 and 4.10 yields an expression in which increasing the adsorbate density of states at the Fermi energy produces a larger change in resistivity.[161] This explains why thiols molecules, which strongly adsorb on Au surface are able to cause a significant decrease in the conductivity of the metal in comparison to other molecules such as pyridine that weakly interact with the metal surface, as observed by Tao and co-workers.[162-164] In this way, it is important to note that the electronic character of the adsorbate plays a central role. For example, the binding of alkanethiol molecules with different chain lengths on Au produce the same change in resistivity because the Au-binding moiety is the same and the orbitals near the HOMO-LUMO gap were not influenced by other constituents of the molecule. This has been widely observed on literature through x-ray photoelectron spectroscopy (XPS) experiments, which showed that the energy binding of thiol moiety from different thiolate molecules on Au surface was the same.[165] Additionally, Bohn's

group demonstrated through a series of experiments employing alkanethiols with different lengths that the change in resistivity due to adsorption of molecules on ultrathin films of Au was independent of the length of the molecules.[161,166,167]

Figures 4.43A-C show the I – V curves in air of the Au nanowire devices modified with alkanethiols and showed in Figures 4.42B-D. As already observed with the measurements in water, in all the three cases the devices presented a systematic increase in the resistance by increasing the concentration of alkanethiol solutions. However, this increase is not so pronounced as that observed with measurements in water and it is independent of the immobilized molecule. Moreover, no hysteresis was observed in the measured curves. A summary of the results for variation in electrical resistance of nanowires before and after immobilization of molecules showed in Figures 4.43A-C is presented in Table 4.6.

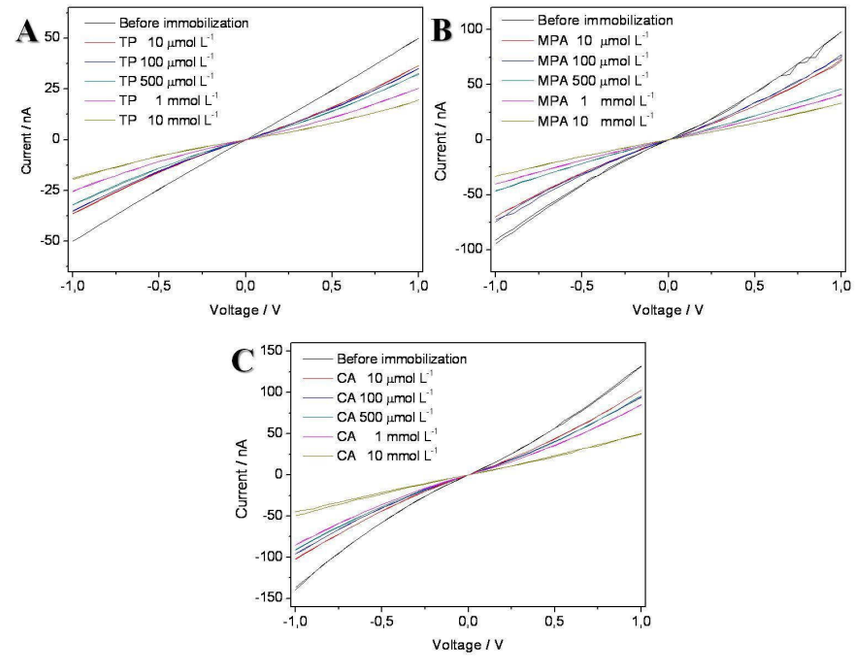

Figure 4.43. Electrical characteristics in air of Au nanowires devices before and after their surface modification with variable concentrations of thiolpropane (A), mercapto-propionic acid (B) and cysteamine (C), respectively.

Table 4.6. Variation in electrical resistance (ΔR) of Au nanowire devices measured in air after their exposure to alkanethiol solutions with different concentrations. The values of ΔR were calculated from the expression $\Delta R = (R_{mea}\text{-}R_{bi}/ R_{bi}) \times 100$, where R_{bi} and R_{mea} are the resistance of nanowires before and after immobilization of alkanethiol molecules, respectively. The variation in the values of ΔR correspond to the standard deviation of the mean with n=3 measurements.

	Thiolpropane	**Mercapto-propionic Acid**	**Cysteamine**
Concentration / mmol L^{-1}		**ΔR / %**	
0.01	37.5 ± 6	37.5 ± 5	30.1 ± 7
0.1	44.4± 8	42 ± 12	22.4 ± 5
0.5	52.2± 12	55.7± 7	94.7 ± 9
1	62.5± 11	99.2 ± 10	126 ± 10
10	209.7± 10	163 ± 13	177.5 ± 11

It is clear from these observations that the I – V characteristics of chemically modified nanowires is very different in water based measurements, and this must have an influence from the acid-base properties of the functional groups of the molecules immobilized on Au nanowires. As it was pointed out before, one of the main aspects observed in the I – V curves measured in water was the hysteric effect seen especially on those devices modified with MPA. Figures 4.44A-C show the zoomed I – V curves near 0 V of Au nanowire devices modified with 10 μmol L^{-1} of TP, CA and MPA in comparison with their non-modified surface, respectively. It is evident as already mentioned that the hysteric effect in the voltage scale is more pronounced on nanowires surface modified with MPA, which exhibited a voltage hysteresis width of 75 mV in comparison to 20.1 mV and 15.7 mV presented by TP and CA, respectively. Comparing these results with that observed in Section 4.5.6.1 for salted solutions, it suggested that the charge of the functional groups of immobilized molecules contributed to the hysteresis observed in the I – V curves. The pK_a values for the carboxyl groups from MPA and primary amine groups from CA are 4.8 and 8.35, respectively, what means that in the pH range that the experiments were carried out both functional groups of the molecules should be ionized.[168] In this case, as the immobilized molecules have a short length, the surface charge imposed by their acid-base properties could directly affect the electrons scattering on the surface of nanowires during electrical measurements.

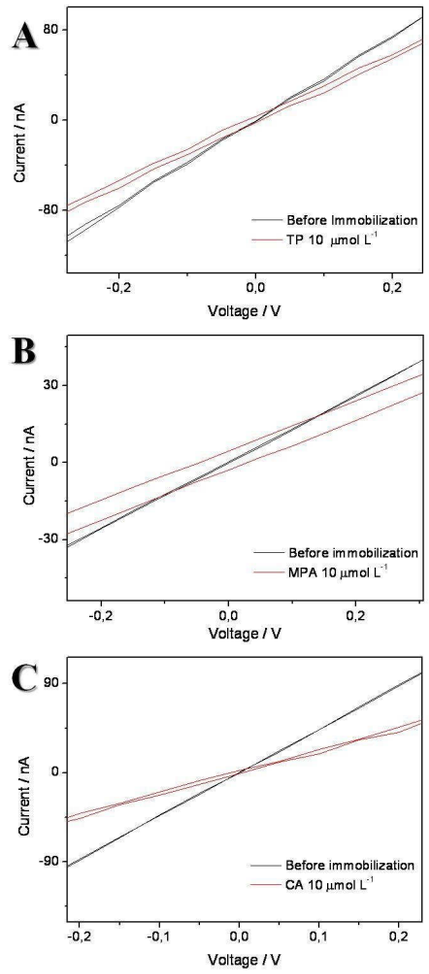

Figure 4.44. I – V behavior of Au nanowire devices measured in water before and after their surface modification with 10 μmol L^{-1} of TP (A), MPA (B) and CA (C).

The fact that a largest hysteresis in the voltage scale was observed for surfaces modified with MPA, but not with that modified with CA can be associated to the fraction of ionized functional groups. It is well known that in solutions the primary amine group of cysteamine is completely

protonated when pH < 8.35. However, this situation can be totally different when these molecules are immobilized on surfaces due to their relative dense packing arrangement. In this case, once a surface amine group is protonated, its positive charge can suppress the protonation of neighboring groups. The poor solvation and bridging between neighboring charged groups would also suppress further protonation. In the case of MPA, the carboxyl groups have a higher volume and their negative charge in pH > 4.8 can be stabilized by formation of dimmers on the surface. Indeed, this is consistent with several reports on literature showing that the fraction of protonated amine groups of molecules immobilized on different surfaces in pH ≈ 7 was very low, and just could be increased for at least 50 % in pH ≈ 1.[169-171] On the other hand, immobilized carboxylated molecules could present a relatively higher fraction of ionization. The presence of these charges on the surface has a direct relation with the surface potential, and can be probed by zeta potential measurements.[172] Nevertheless, as it would be difficult to measure the zeta potential on the surface of nanowire devices, an approximation experiment to measure it was performed by immobilizing 10 mmol L^{-1} of MPA and CA on ultrathin Au nanowires dispersed in solution (for experimental details see Section 3.5.2.1). The results of these analyzes demonstrated that in pH 6.7 the surface potential of carboxylated nanowires was - 40 ± 8.9 mV (negative due to the deprotonation), whereas those modified with cysteamine was only + 6 ± 6.5 mV (positive due to the protonation), thereby, corroborating our previous observations about the ionization of these functional groups. According to the Grahame equation the surface charge density (σ) can be determined by:[67]

$$\sigma = \sqrt{8\varepsilon\varepsilon_0 kTn_0}\ sinh\left(\frac{\psi_s}{2V_{th}}\right) \qquad \text{(Eq. 4.11)}$$

where V_{th} is the thermal voltage, ε is the dielectric constant of the medium, ε_0 is the dielectric permittivity of vacuum and n_0 corresponds to the bulk ions concentration (in this case 1 µmol L^{-1}).[173] The other terms had their meaning already defined in the text. The surface charge density value found for CA was 14 nC cm^{-2}, which was consistent with the idea that the fraction of ionized amine groups was low. On the other hand, for MPA, a value of 102 nC cm^{-2} for surface charge density could be measured. In the case of immobilization of TP molecules, which form a hydrophobic surface without ionizable groups, it was observed that the zeta potential exhibited as expected a low magnitude (-5 ± 6.9 mV), and in the range of negative

potential. As the measurements were performed only in deionized water, this negative value for the zeta potential could be attributed to the adsorption of hydroxide ions generated from the self-ionization of water:

$$2H_2O \longleftrightarrow H_3O^+ + OH^- \qquad K_w = 10^{-14}\ mol^2\ L^{-2}$$

To estimate the surface coverage and correlate it with the fraction of ionized functional groups, the Persson's relation (Eq. 4.9), which states that the resistance increase is linearly proportional to the coverage density was applied. Thus, by taking the respective kinetic model described by Jung *et al.* for adsorption of alkanethiols on Au[174]

$$\theta_S = \theta_{S_{max}} \left[1 - \exp\left(-\frac{S_o C v t}{\theta_{S_{max}}}\right)\right] \qquad \text{(Eq. 4.12)}$$

where θ_S is the coverage density, t is the time, S_o is the probability that a molecule will adsorb upon its collision with the surface of the metal, $\theta_{S_{max}}$ is the total surface coverage per unit area, C is concentration and v is molecular velocity. The following relation with Persson's model could be established based on the change of electrical resistance (ΔR)[175]

$$\frac{\Delta R}{R} = \left(\frac{\Delta R}{R}\right)_{max} \left[1 - \exp\left(-\frac{S_o C v t}{\theta_{S_{max}}}\right)\right] \qquad \text{(Eq. 4.13)}$$

plots of ΔR/R versus *C* (Figure 4.45A-C) for all three molecules employed showed an increase in the resistance of nanowires while increasing the density of adsorbates on their surfaces, as it was predicted by Persson's model. Applying the least square method, these measured data could be fitted with Equation 4.13 adjusting t = 600 s (time that the nanowire devices were submerged in the alkanethiol solutions) and the total surface coverage per unit area for each surface could be determined and is exhibited in Table 4.7. From these data, it was possible to see that the maximum coverage density presents a small difference for all three molecules employed for immobilization on nanowires. Based on the results of surface charge density calculated before and the total surface coverage found from the fitted data, the fraction of ionized molecules could be approximately estimated as 0.6 % and 0.04 %, for MPA and CA, respectively.

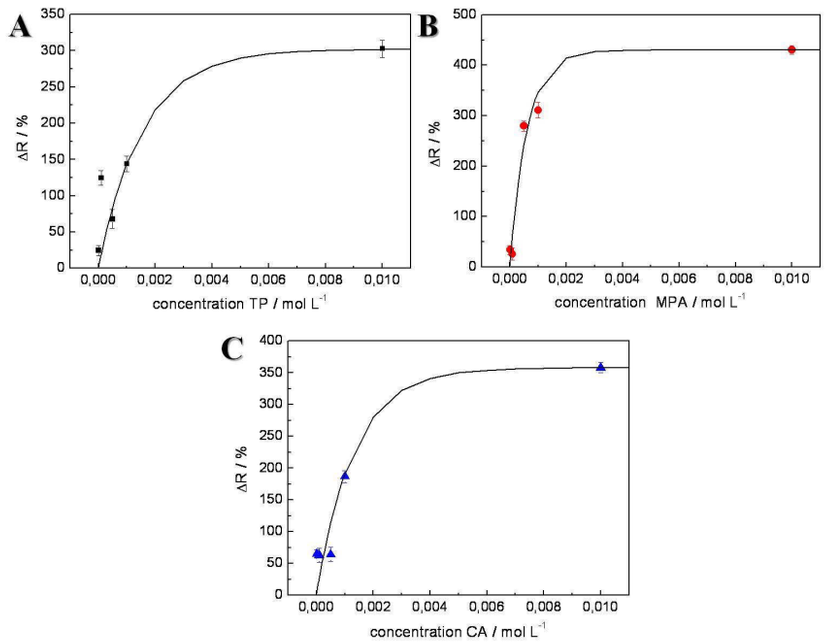

Figure 4.45. Plots of ΔR as function of alkanethiols concentration employed for immobilizing on Au nanowire devices. The dots correspond to the experimental data, whereas the solid lines are the fits of Equation 4.13 for adsorption of thiolpropane (A), mercapto-propionic acid (B) and cysteamine (C), respectively. The error bars correspond to the standard deviation in the values of ΔR for the mean with n=3 measurements.

Overall, these values demonstrate that even a small fraction of ionized species on the surface of nanowires is able to cause a surface charging that can influence the electron transport of Au nanowires in solution. Although Persson's model do not explain how this combined effect of thiol binding and surface charge of immobilized molecules can influence the electron transport on metal surfaces in solution, these results clearly showed that the electrical resistance of ultrathin Au nanowires is extremely sensitive to the effects of molecular adsorption and surface charging.

Another general aspect observed in the data measured in solution and that raised the third question, was the reason for the transition of I – V curves from linear to non-linear. This effect was observed in the measured curves independent of the alkanethiol molecule employed and was also seen during the measurements with solutions of NaCl. Thereby, it indicated that this phenomenon is a general aspect for adsorbates onto Au nanowires. Previously, it was reported that the adsorption of impurities from the air on polycrystalline Au nanowires surface can strongly affect the linear electrical behavior of nanowires.[143] Recently, Jiang and co-workers also showed through theoretical investigation employing density functional theory that linear chains of Au icosahedra fused by either vertex or face sharing can present a competitive electrical behavior between metallic and semiconductor when thiolated molecules are adsorbed on their surfaces.[176] The authors found that adsorption of thiols on the configuration of face sharing does not alter the electric behavior of Au and it is always metallic. On the other hand, vertex sharing presents a dependence on its charged and no charged energy states to be semiconductor or metallic. These observations from literature are all important, but they are restricted to specific cases and it is difficult to generalize them for our measured data. This implies that more intrinsic investigation in the electronic states and possibly also in the crystallographic structure of these ultrathin nanowires analyzed in this thesis is needed to understand the effect of adsorbates in their electric properties, so that this question is still opened.

Table 4.7. Total surface coverage of Au nanowire devices modified with different alkanethiol molecules.

Molecule	Total Surface Coverage / molecules cm^{-2}
thiolpropane	2.78×10^{14}
mercapto-propionic acid	1.10×10^{14}
cysteamine	2.36×10^{14}

In summary, the results based on the acid-base properties of immobilized molecules showed in this section, suggested that these ultrathin nanowires could be employed as highly sensitive sensors to probe readily low concentration of specific analytes that are able to interact electrostatically with the functional groups of immobilized molecules. Further processes of

molecular adsorption and the effect of ionizable functional groups on electrical resistance of nanowires could be exploited using the technique showed here. The next Section will present the results of the application of Au nanowires as sensors to monitor the electrical activity of neuronal cells.

4.6 Sensing Cellular Biology

In Section 4.5, the assembly and the electrical properties of ultrathin Au nanowires were described as well as their sensitivity to surface scattering due to ion and molecule adsorption and consequently changes in their electrical resistance. It was demonstrated that, due to their small dimensions, Coulomb interactions on the surface of the wires can strongly affect their electrical properties. In this section, the ability of the nanowires to stimulate and record the electrical activity of neuronal cells will be demonstrated. Employing one-dimensional nanostructures to sense biological species represents an important step towards investigating and understanding such systems with very high spatial resolution. Through proof-of-principle experiments, this section describes the cellular growth over nanowires devices, their interaction and, finally, electrophysiological measurements using Au nanowires devices.

4.6.1 Nanowires Interacting with Cell Membrane

The interface between the cell membrane and nanowires represents the mainway that a nanowire can sense a cell, or more specifically, what kind of transient voltages (extra- or intracellular) a nanowire can detect. In this context, the hydrophobicity of thesurface of the wire plays an important role in this hybrid interaction. For instance, McEuen's group demonstrated that supported lipid bilayers, which represent a model for mimicking the cell membrane, can diffuse freely across single-walled carbon nanotubes horizontally assembled in a planar surface.[177] In this case, the surface of the nanotubes was not chemically modified and the main interaction between lipid bilayers and nanotubes was based on van der Waals attraction. In our case, we had a similar feature with ultrathin Au nanowires, which, as demonstrated before, were covered with a thin layer of oleylamine molecules, and, thus, exhibited a hydrophobic surface. Considering a neuronal cell with its axon ideally assembled over an array of Au nanowires (Figure 4.46A), three basic possibilities for the hybrid nanowire/cell configuration could be put forward (Figure 4.46B): The nanowire may be outside the cell (Figure 4.46B-i), it can be in the middle of the lipid bilayer that forms the cell membrane (Figure 4.46B-ii), or the nanowire can even be inside the cell (Figure 4.46B-iii). Because the tails of the lipids that form the cell

membrane are also hydrophobic, the interfacial energy would be lowest if the nanowire was inside the membrane. This is similar to a situation where a hydrophobic object suspended in an aqueous media would interact with a drop of oil added to this media. For the object, it is energetically more favorable to be surrounded by the non-polar molecules of the oil than to be only surrounded by water.

We can analyze this interface more quantitatively by taking into account the fact that the interfacial energy of the oil/water system only is only 35 mJ/m^2.[178] This means that each section of surface area *S* between the object and the water results in an energy $\gamma_{ie}S$, where γ_{ie} is the interfacial energy per square surface. For a 2 µm long nanowire with a diameter of 2 nm that is completely surrounded by water, the interfacial energy is about 10^{-16} J. When a drop of oil of radius R is able to surround the nanowire, this would cause a change in the Helmholtz free energy of

$$\Delta E = \gamma_{ie}\Delta S \qquad \text{(Eq. 4.12)}$$

Considering that the force (F) on the droplet can be defined as F = ΔE/R, it can be roughly estimated as 2 x 10^{-10} N. Thus, this means that the drag force on a droplet of R = 5 µm is only 10^{-11} N, which suggests that it would be very difficult to remove the oil from the object.[178] Additionally, if we consider that the object has a shape such as a cylinder, the oil droplet can lower its interfacial energy even more by eliminating the high curvature regions at the intersection with the object, producing a configuration similar to that shown in Figure 4.46B-ii. It is worth pointing out that for Au nanowire devices such as those shown in Section 4.5, this observation is also true for the non-suspended section of the nanowire, which is usually found in the central part between the pair of leads. In this case, the suspended part of the wire could move into the middle of the membrane, and consequently help the non-suspended part of the wire to overcome its van der Waals attraction to the surface and also move inside the membrane.

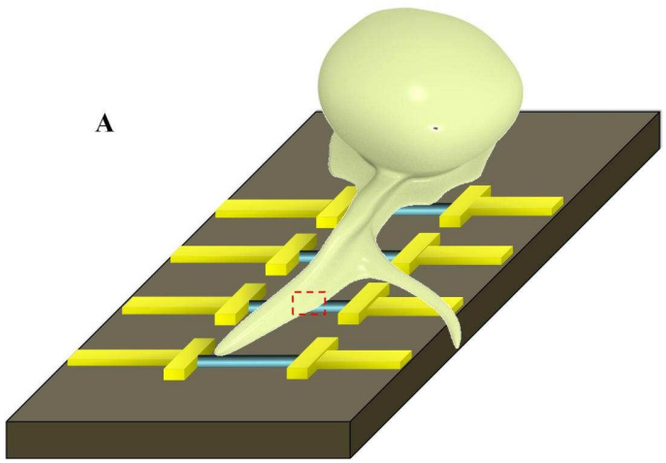

Figure 4.46. A –Diagram illustrating a neuronal cell assembled over a nanowire device array. B –Possible interactions between cell membrane and nanowire. (i) Cell membrane is suspended over the nanowire that is located outside the cell. (ii) Nanowire is between the hydrophobic parts in the middle of the cell membrane. (iii) Nanowire is inside the cell.

These observations are all relevant. However, we still have to consider that prior to the cell plating over the nanowire device array the surface of the devices was covered with a thin layer of poly-l-lysine, the monomerical chemical structure of which is shown in Figure 4.47. Poly-l-lysine is an amino acid polymer which, due to the protonation of its amino groups in physiological pH, is positively charged, and, thus, lends a hydrophilic character to the substrate and the nanowires. The hydrophilicity of the polymer is dependent on the ratio of its molecular conformation, i.e. α-helix and β-sheet, which are known to exist in equilibrium under specific conditions.[179,180] For poly-l-lysine at room temperature, the α-helix configuration is the most predominant shape.[179,180] However, taking into account the fact that our substrate is basically hydrophobic, it would be energetically more favorable for poly-l-lysine to assembly over the

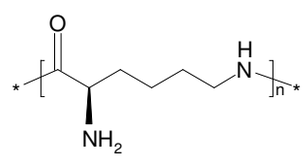

Figure 4.47. Monomeric chemical structure of poly-l-lysine.

substrate with a β- conformation rather than with an α-helix, although it could still maintain poly-cationic behavior. The exact interaction of poly-l-lysine with the substrate is unknown, but these considerations about the hydrophobic and hydrophilic parts of the surface can be useful for interpreting our current results and also for future research employing such wires. Moreover, it is worth mentioning that this step of using poly-l-lysine as a coating agent is extremely important because through the electrostatic interaction between the negatively charged phospholipids of the cell membrane and the positively charged amino groups of the poly-l-lysine, it enables a better cell adhesion to the surface.

We investigated the cell-substrate interaction by using dual-beam focused ion-beam (FIB)/SEM instruments. To observe the cell- substrate interaction using the FIB/SEM system, we plated HL-1 cells over a Au nanowire device array. The experimental details of cell fixation, drying and FIB operation are given Section 3.7.

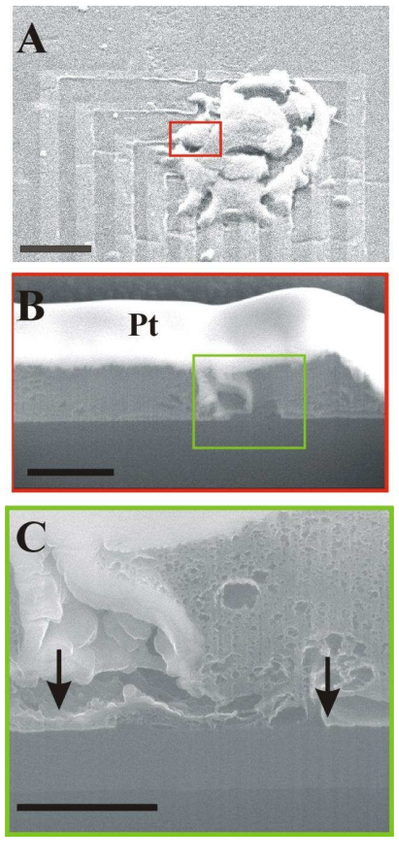

Figure 4.48. A – SEM micrograph of HL-1 cells assembled over an array of nanowire devices. Scale bar is 20 µm. B –Zoomed SEM micrograph of the area highlighted with the red box in (A) showing the assembly of a cell directly over a device. A platinum (Pt) layer (white layer) was deposited on top of the cell. Scale bar is 5 µm. C– Zoomed SEM micrograph of the area highlighted with the green box in (B) exhibiting the tight adhesion of the cell on the contact pads of the nanowires (indicated by arrows) and on the groove. Scale bar is 2 µm.

Figure 4.48A shows an SEM picture of a nonconfluent cell layer assembled on top of a device array. A thick layer of Pt on top of the cells was deposited to protect the cellular structures during FIB processing. Cross-sectioning of the cells by FIB and subsequent SEM micrographs show that the cells were connected tightly to the underlying substrate (Figures 4.48B and C). Figure 4.48C depicts a zoomed image of a pair of leads (indicated by arrows) where Au nanowires should be assembled, but unfortunately none were not observed. On the other hand, the good cell adhesion on top and between the leads is clearly shown. This non-visualization of ultrathin Au nanowires at this point can be attributed to two main reasons, the position of the cross-sectioning (the nanowires are not uniformly distributed over the leads) and the low contrast provided by the thin wires that makes them hardly distinguishable from other materials. Unfortunately, this lack of visualization prevented us from gaining further information from these images.

4.6.2 Neuronal Morphology

Neurons are primary cells that are very sensitive to growth conditions as well as to the plating substrate. As discussed in the previous sections, this step in the growth and adhesion of cells on device arrays is critical because it is directly related to the electrical stimuli and recording from the cells. In practical terms, it is an important issue for biosolid nanodevices intended to be applied in neurological implants. The process describing the culturing of neurons in the Au nanowire devices is described in Section 3.6.2. Figures 4.49A and B show optical images of the neuronal morphology on the surface of Au nanowire devices. The images were taken after 8 – 10 DIV of cell culturing, and they clearly show that healthy cortical neurons adhered and grew on the substrate exhibiting typical cell body morphology and size. It is worth pointing out that the surface of the devices was passivated with PMMA, which has the

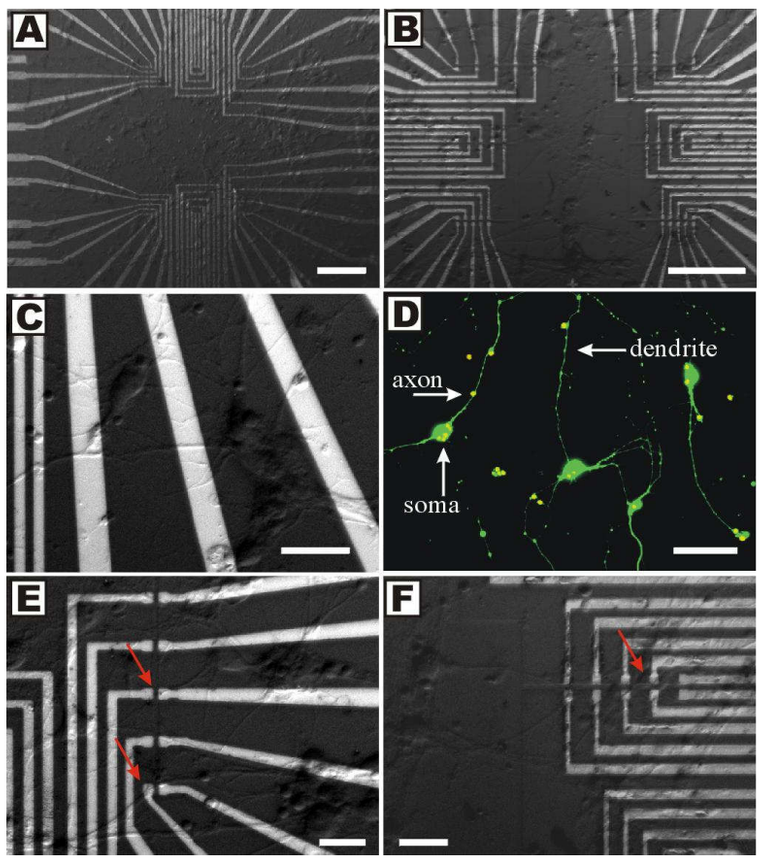

Figure 4.49. A and B – Differential interference contrast (DIC) microscopy images of cultured cortical neurons (10 days) on Au nanowire devices. Scale bar is 100 µm.C – Higher magnification DIC image of neurons exhibiting healthy morphology while growing overthe devices. Scale bar is 20 µm.D –Confocal fluorescence image for labeled cortical neurons after 8 days in culture. Scale bar is 50 µm. E and F –DIC images showing the neuronal growth directly on the grooves over the Au nanowires devices (indicated by the red arrows). Scale bar is 25 µm.

advantage of being biocompatible and as demonstrated by Johanssonet al. can also act as a guide to cell growth.[181] Figure 4.49C also shows that neuronal growth was accompanied by a variable degree of neurite extension, similar to that observed for neurons grown on control surfaces and confirmed by immunocytochemistry analysis (4.49D). Moreover, Figures4.49E and F show that the cells grew and tightly interacted with the grooves where the Au nanowires were assembled. Such tight contact is potentially helpful because it establishes a better sealed electrical interface.[82-84] Although not performed here, it is also possible to carry out experiments patterning the surface with poly-l-lysine and consequently guide cell growth, which is a step forward because it could lead the cells to grow directly over the wires as shown schematically in Figure 4.46A.

4.6.3 Signal Recording

In Section 2.5.1, the basic concepts about the interface electrode/electrolyte were introduced, and appropriate models to describe the signal transduction were showed in Section 2.6.4. In this section, the principle of these models was applied to determine how a biological signal would be transduced into an electrical signal that can be amplified and processed by external circuitry. To detect the electrical signals from the cells, the electrical resistance of the nanowires must be much lower than the resistance of the cell membrane, which is usually between 100 – 500 MΩ.[77] Thus, in order to check the quality of the devices, we measured the electrical resistance (two-point probe) of each device immediately after each step of the fabrication process. Figure 4.50 exhibits a representative I – V curve of a Au nanowire device just before cell culturing. The histogram in the upper left part of Figure 4.50 demonstrates that the electrical resistance of 65 devices of Au nanowires at this last step was around 1 – 10 MΩ, with a predominance of wires having a resistance of 1.3 MΩ. These values are comparable to the resistance of patch pipettes and microelectrode arrays, which are often employed to recordion currents from the cells, thus suggesting that the nanowires were sensitive enough to record the same cellular electrical activity. The electrical stability of nanowires in PBS solution was also checked along the time axis.

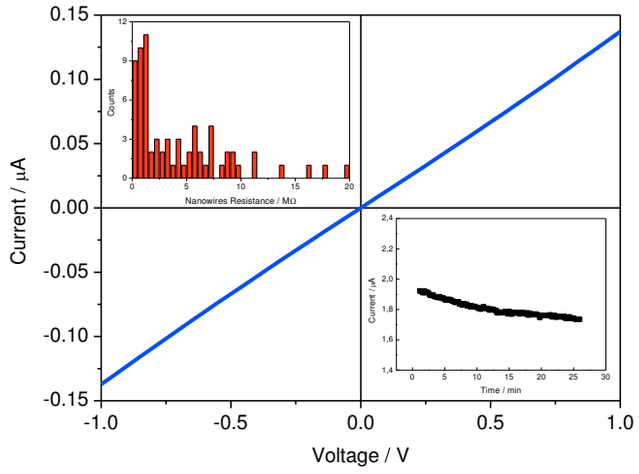

Figure 4.50. Current vs voltage of a Au nanowire device having an electrical resistance of ≈ 7.7 MΩ. The inset in the upper left part shows a histogram of electrical resistance values of 65 nanowire devices. The inset in the bottom right part demonstrates a current vs time curve of a representative device submerged in 10 mmol/L PBS and biased at 500 mV for 26 min.

The current vs time curve depicted in the bottom right part of Figure 4.50 demonstrates that the Au nanowires display constant electrical current when biased at 500 mV for 26 min, thus showing that Au nanowires present relatively long-term stability in solution.

We attempted to stimulate and measure the electrical signals from neuronal cells grown on Au nanowire devices by biasing the nanowires and recording the electrical current along the time, similar to a voltage-clamp experiment. Figure 4.51A illustrates the device configuration during the measurements. In order to avoid high voltages, which could possibly lead to redox reactions, the nanowires were biased to a maximum of 300 mV versus Ag/AgAgCl. Figure 4.51B shows three representative curves of current versus time for the same nanowire device at different biases recording the electrical activity of the neurons shown in Figure 4.49F. Although the noise level from the background current is relatively high, a series of spikes in the current trace along the time could be observed at the three different potentials applied.

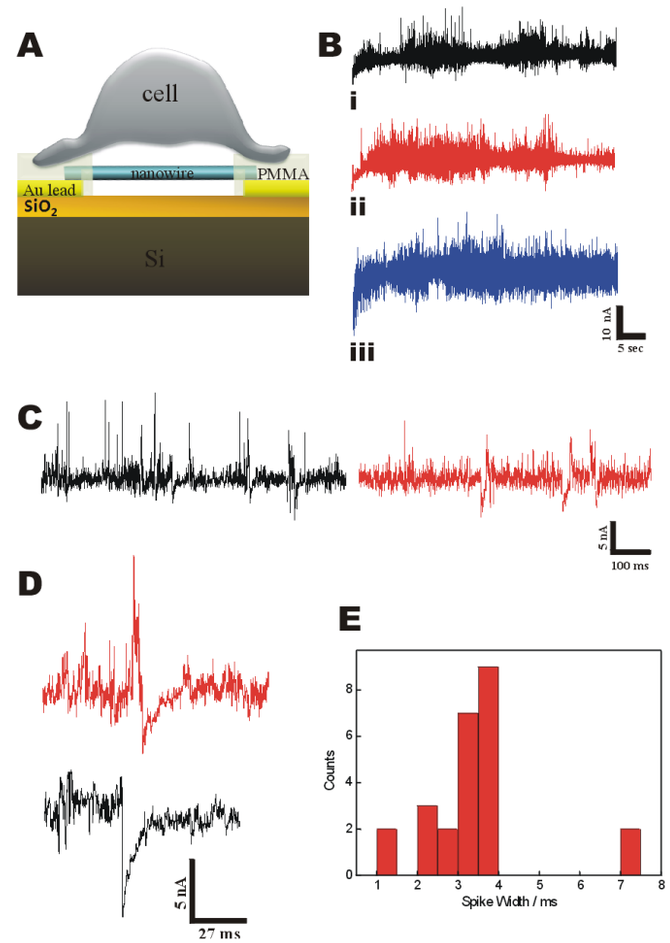

Figure 4.51. (A) Schematic illustrating the experimental configuration for measuring the electrical activity of a cell. (B) Three representative current traces over time for nanowire devices biased at 100 mV (i), 200 mV (ii) and 300 mV vs Ag/AgCl (iii). The same device was used to record all the curves. (C) Expanded plots of current traces of nanowire devices biased at 100 mV (left) and 200 mV vs Ag/AgCl (right) shown in (B). (D) Zoomed plot of two predominant kinds of spikes observed in the measurements. (E) Histogram of down-spike width values observed in all three curves shown in (B).

Expanded plots of curves showed in Figures 4.51B(i) and (ii) are depicted in Figure 4.51C. These plots show that the observed spikes exhibited shapes characteristic of capacitive stimulus and fast inward ion currents into the cells. Two predominant kinds of spikes were observed in all the recorded curves and are shown in Figure 4.51D. The shapes of the signals resemble those extracellular action potentials recorded using microelectrode arrays and can be understood on the basis of the respective considerations. In the case of the curve shown in the upper part of Figure 4.51D, initially a fast up-spike is caused by a stimulus current from the capacitive coupling of the cell-nanowire device junction. Because the resistance of the cell membrane is relatively high (100 – 500 MΩ), a small current is enough to change its potential, consequently leading to a displacement of gating charges and opening of ion channels, and thus causing the depolarization of the cell membrane. Sequentially, the observed fast down-spike is related to the fast inward Na^+ currents, which are typically characterized by the negative deflections in the current trace over time.[182-185]For the case of the curve shown in the bottom part of Figure 4.51D, only the negative overshooting spike caused by the fast inward Na^+ currents could be observed. These different extracellular signal shapes of the same cell are mainly attributed to the dimensions of the nanowire device, which is smaller than the cell fraction analyzed.[185] Other factors such as inhomogeneous distribution of ionic conductances and coupling of the nerve cell to the device can also be considered.[84] The analysis of 29 fast down-spikes indicated that the mean spike width was 3.5 ms (Figure 4.51E), which is consistent with that obtained from signals recorded using microelectrode arrays and voltage-clamp experiments (Figures 4.52A and B).

Several control experiments were performed in order to confirm the observed results. Figures 4.53A and B show the current trace over time for devices submerged in culture media but without cells, and devices with cells on top but without Au nanowires contacting the pads, respectively. In both curves the electrodes were biased at 200 mV versus Ag/AgCl, and although the noise level is relatively high, no peaks or spikes could be observed. These results confirmed that no redox reactions involving chemicals of the culture media or further processes related to instrumental noise occur during the cellular recordings previously shown. This implies that the spikes displayed in Figure 4.51 were directly correlated to the electrical activity of cells coupled to the Au nanowire device.

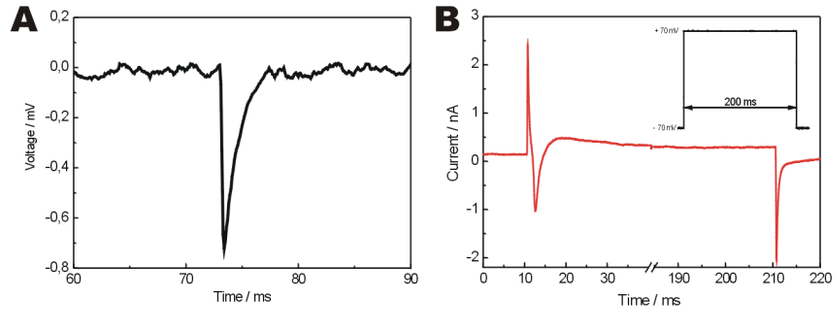

Figure 4.52. (A) Spontaneous extracellular voltage transient versus time recorded for a neuron-microelectrode junction. (B) Elicited membrane current versus time recorded in the whole-cell voltage clamp configuration during stimulation with a pipette electrode. The duration of the voltage pulse applied for stimulation was 200 ms starting from a holding voltage of -70 mV (inset). The recorded current trace exhibits an initial pipette-electrode artifact due to the applied voltage pulse from the holding potential, followed by a fast negative inward current. Afterwards, the measured current reaches a plateau that is dominated by ohmic leak currents due to the open channels, followed by another spike artifact related to the release of the holding voltage.

Apart from these experiments, we also tested the interference of some easily oxidized cellular chemicals such as the neurotransmitters γ-aminobutyric acid (GABA), glutamic acid and dopamine (Figure 4.53C). However, as demonstrated in Figure 4.53C none of these neurotransmitters was found to be electroactive when the Au nanowire device was biased at 200 mV vs Ag/AgCl. In fact, the oxidation of these molecules should result in up-spikes (monophasic spikes). For dopamine oxidation in gold electrodes using a Ag/AgCl as reference electrode, it is known that the oxidation potential is higher than 400 mV.[186] The oxidation of dopamine at higher biasesis possible, but in our experiments with the cells it can be ruled out because the neuronal cells employed were non-dopaminergic cells.

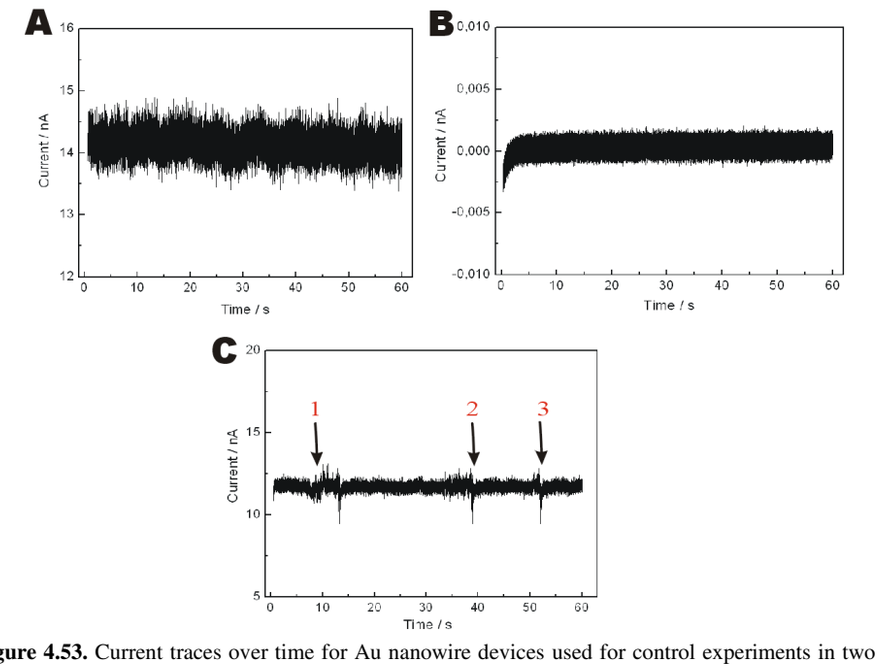

Figure 4.53. Current traces over time for Au nanowire devices used for control experiments in two different situations: (A) Device with Au nanowires but without cells on top, (B) device without nanowires but with neuronal cells grown on its surface. In both cases the devices were biased at 200 mV vs Ag/AgCl. (C) Current versus time data recorded for a Au nanowire device without cells on top and biased at 200 mV vs Ag/AgCl during addition of different neurotransmitter solutions to the culture media. The numbers indicated by the arrows correspond to times when solutions of (1) 50 µmol/L GABA, (2) 50 µmol/L glutamic acid and (3) 50 µmol/L dopamine were added to the solution on top of the nanowires.

These results present strong evidence of the electrical response of the cells to excitation through the voltage applied to the Au nanowire device, and demonstrated that such devices can be used to electrically stimulate and record significant ion conductances in neuronal cells. The transduction of the recorded signals is correlated with the description reported in Section 2.6.4 and, to a certain extent, it is similar to the excitation by extrinsic current flow elicited by extracellular carbon-based electrodes.[187] A similar approach using carbon nanotubes to evoke membrane depolarization of neuronal cells was employed by Gheith et al.[188] However, in our

case the main advantage in comparison to the approach reported by Gheith and co-workers was the assembly of organized arrays of nanowire devices that could be used for stimulating and recording the ionic conductance of the cells with better spatial resolution than the detection of signals from multiple randomly distributed neurons. Previously, Patolsky et al. showed that an array of silicon nanowires based on field effect transistors could be employed to detect the spontaneous electrical activity of neuronal cells and/or that evoked by electric stimulation.[189] Although this approach appears very promising for analyzing neural networks with high spatial resolution, it cannot perform the electrochemical detection of electroactive neurotransmitters such as dopamine. In our case, the ultrathin Au nanowires also have the advantage that they can be used to electrochemically detect those neurotransmitters by simply applying relatively high voltages. Although only three nanowire devices could be used simultaneously during the measurements, it should be pointed out that this limit was only due to the available measurement electronics and in future work more sophisticated multi-connected devices could be developed.

Through the proof-of-principle experiments, it was shown that devices made of ultrathin Au nanowirescan be used to electrically stimulate and record ion conductances from neuronal cells. The neurons were grown over nanowire devices exhibiting typical healthy cell body morphology and size.Although it was not possible to determine the exact interaction between Au nanowires and cell membrane, a tight connection and good cell adhesion to the substrate where nanowires were assembled was observed by FIB/SEM experiments. Electrophysiological recordings demonstrated a clear signature of the electrical excitation of neuron when the nanowires device was biased up to 300 mV. The shapes of the recorded signals were associated with a capacitive stimulus and opening of voltage-activated ion channels, resembling those signals recorded with microelectrode arrays and voltage-clamp experiments. The electrical responses that were observed from Au nanowire devices interacting with individual cells is an important step in the nanoscale electrical probing of biological systems with high local spatial resolution. More advanced studies concerning the cellular chemistry and behavior would be performed after the development of more sophisticated electronics connecting the devices and guiding the cell growth.

Chapter 5

Conclusions and Future Directions

Advances have been made recently in the chemical synthesis of ultrathin Au nanowires with diameters of ~ 2 nm. These one-dimensional nanostructures are considered essential building blocks that can be used to construct nanoelectronic devices for applications in sensors, photonics, and waveguides. Although efforts have been made towards understanding their synthesis and their electrical characteristics, several questions remain open concerning the production of such nanowires as well as their intrinsic electric properties. The work for this thesis focused on improving the understanding of the chemical processes related to the formation of ultrathin Au nanowires and their electrical characteristics in air and in aqueous solutions. Owing to their possible technological applications as sensors for chemical and biological species, this last aspect was important because it contributes to the knowledge of how the electrical resistance of wires can be influenced by the adsorption of ionic and molecular species on their surfaces.

The ultrathin nanowires were synthesized employing a relatively simple wet chemical approach using the organic molecule cis-oleylamine and AuCl as a metal precursor. The organic molecule (cis-oleylamine) acted as a surfactant, and as a stabilizing and reducing agent of Au(I) ions. This avoided the addition of further chemicals to the reaction. The synthesis of Au nanowires involved the formation of a $[Au(oleylamine)]^+$ complex. The complexing of Au(I) ions by oleylamine molecules was shown to be influenced by aurophilic interactions, which induced the molecular organization of oleylamine in solution and this organization assisted the formation of Au nanowires with diameters of about 2 nm. The chemical analysis of the $[Au(oleylamine)]^+$ complex demonstrated that this complex presented two stability constants that were dependent on the concentration of Au(I) species. It was found that for relatively low concentrations of Au(I) ions, the oleylamine molecules were less affected by structural changes which could destabilize their supramolecular organization and alter either the final shape or the morphology of structures.

The structural characterization of Au nanowires revealed that nanowires with diameters of 1—2 nm and 10—14 nm were produced. Often their extremities showed a characteristic bulging and the presence of twin boundaries (thick Au nanowires). In contrast to previous work, the bodies of the nanowires observed here were defect-free along the axial direction. Due to the instability of the ultrathin Au nanowires to electron beam irradiation during HRTEM experiments, it was difficult to resolve their structural characteristics more precisely. Additional efforts to resolve the lattice structure of nanowires and oleylamine molecules coating their surface were performed by using the new graphene support for TEM analysis. The preliminary analysis provided fundamental information on the molecular assembly over the nanostructures. These observations are very significant because they showed new possibilities for studying the molecular adsorption in specific crystallographic planes of crystalline nanostructures.

The observations from the structural characterization of the Au nanowires and nanoparticles produced showed interesting features that facilitated the understanding of the mechanism for producing Au nanowires with a much higher aspect ratio than previously shown in the literature. By saturating the reaction solution with O_2, a more effective production of nanowires and an increase in their length was observed. The nanowires presented an average diameter of 1.8 nm and a length of up to 8 μm, yielding an aspect ratio of approximately 4000. This was attributed to a growth mechanism based on an enhanced oxidation of twin defects on Au nanoparticles that were always first produced during the synthesis of nanowires. This simple O_2-assisted process is also a promising new route for the rapid large-scale production of ultrathin single crystal Au nanowires and its discovery made it possible to produce nanowire devices with different lengths.

To investigate the electrical properties of these long ultrathin Au nanowires they were assembled using a microfluidic approach over metal electrodes. Two-point probe measurements at room temperature were carried out and showed that these ultrathin Au nanowires exhibited an increase in their electrical resistance predicted by the decrease in their diameter. A high current density of approximately 10^{13} A/m^{2}wasalso observed and was attributed mainly to the free-grain boundary structure of nanowires. In addition, the results demonstrated that some intrinsic electrical properties of ultrathin Au nanowires were limited by contributions of contact resistance. In order to understand the role of the physics of contacts in the electrical transport of nanowires, we probed the I–V behavior of nanowires at energy scales above the charging energy

and level spacing. Electrical measurements at cryogenic temperatures demonstrated that the electronic contacts at the interface between Au nanowires and metal electrodes, where the contact resistance has a significant influence on electronic transport, could be satisfactorily explained in terms of the thermal fluctuation induced tunneling theory. The results indicated that the contact junction areas had a strong influence on the potential barriers of electron tunneling. These observations were important for further technological applications of Au nanowires as interconnections because they clearly showed that the contact resistance is an important aspect to consider when probing intrinsic electrical transport of nanowires. This opens up the possibility for further work on overcoming this limitation for producing electronic devices based on ultrathin Au nanowires.

Electrical characterization of nanowires in solution and their surface modification with alkanethiol molecules demonstrated that the adsorption of ions and molecules on the surface of nanowires strongly influenced their electronic surface scattering. It was found that the binding of alkanethiols and their acid-base properties can cause different re-arrangements in the electric double layer on the surface of nanowires, and these differences generated variable effects that were not totally understood in the electrical resistance of Au nanowires. Further processes of molecular adsorption and the effect of ionizable functional groups on electrical resistance of nanowires could be exploited using the technique described here.

Finally, proof-of-principle experiments showed that devices made of ultrathin Au nanowires could be used to electrically stimulate and record ion conductances from neuronal cells. The electrical responses that were observed from Au nanowire devices interacting with individual cells were an important step in the nanoscale electrical probing of biological systems with high local spatial resolution. Further development of sophisticated electronics connecting the devices and guiding cell growth could enable more advanced studies to be carried concerning signal processing in neuronal networks.

In conclusion, ultrathin Au nanowires constitute a nearly perfect one-dimensional system for studying electronic transport in metals and the effects of the adsorption of ionic and chemical species on their electrical resistance. The findings discussed in this thesis are just a small bridge showing how the phenomena in a microscale world can be related to a macroscale world. Future work will undoubtedly further explore the fascinating properties of Au as a metal precursor for the synthesis of other structures and their applications.

Appendix A

Fabrication of Microfluidic Channel

To produce a microfluidic channel, a positive structure was first fabricated into a metallic master. A schematic illustration showing the metallic master is depicted in Figures A.1 A and B. The master was made of aluminum and was fabricated by polishing the surface of the metal. As showed through Figures A.1 A and B, it presented two positive cylindrical structures connected to each other by a rectangular and also positive line.

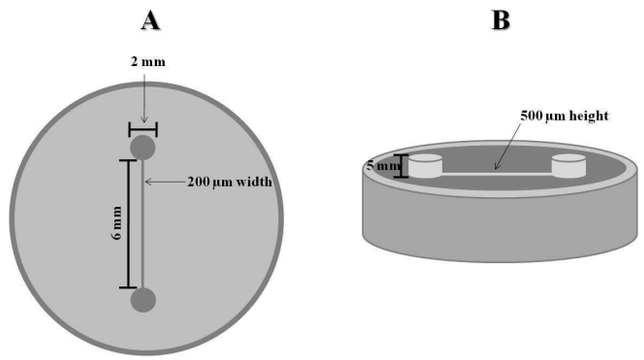

Figure A.1. Illustration of the metallic master used to produce the microchannel. A- top and B side view of the master .

The production of the microfluidic channel using the respective master is described below:

1. Firstly, the master was cleaned with ethanol (70%) and sequentially dried with a stream of N_2.
2. PDMS mixed in a 5 : 1 ratio of base to curing agent (Sylgard 184) was added onto the master and cured overnight in the oven at 60 °C.
3. In the last step, the PDMS layer with the microchannel was stripped off from the master.

Appendix B

Cell Culture - Cortical Neurons

B.1 Cell Isolation

Rat embryonic cortical neurons were obtained as described by Brewer et al.[190] with slight modifications. Briefly, embryos were dissected from pregnant Wistar rats at 18 days gestation following the steps below:

1. Dissect cortices from the embryonic brains.

2. Mechanically dissociate cells by trituration in ice cold Hank's balanced salt solution (HBSS) (without Ca^{2+} and Mg^{2+}), 0.035% sodium bicarbonate, 1 mM sodium pyruvate, 10 mM HEPES, 20 mM glucose, pH 7.4 with a repolished, silanised Pasteur pipette.

3. Add two volumes ice cold HBSS (with Ca^{2+} and Mg^{2+} 0.035% sodium bicarbonate, 1 mM pyruvate, 10 mM HEPES, 20 mM glucose, pH 7.4).

4. Allow non-dispersed tissue to settle for 3min.

5. Centrifuge the top half of the supernatant at 200 g for 2min.

6. Resuspend the pellet in 1ml of Neurobasal Medium, 1% B27, 0.5 mM L-Glutamine per hemisphere isolated.

7. Count cells. Dilute small fraction 1:2 with trypan blue and count dye-excluding cells in a Neubauer counting chamber.

8. Dilute the remaining cells in supplemented Neurobasal medium (see Table B.1).

9. Plate the cells onto the substrates at a density of 60000 cells per cm^2.

10. Exchange half of the medium every 2-3 days.

Table B.1 – Composition of supplemented neurobasal medium

	Amount	Final concentration
Neurobasal medium	49 ml	103
B-27	0.5 mL	1 %
L-Glutamine	125 µL	0.5 mM

Appendix C

Deriving the Equation for Spectrophotometric Determination of the Stability Constant

This appendix will show how the Equation 4.2 used in Section 4.2.3 to determine the apparent stability constant for complexing Au(I) ions was derived.

The chemical equation to describe the complexing of Au(I) ions by oleylamine (OA) is given by:

$$AuCl + OA \rightleftharpoons [Au(OA)]^{+} + Cl^{-}$$

the apparent stability constant (K_{sc}) for this equation can be expressed as follows (for simplicity, the charges were omitted) :

$$K_{sc} = \frac{[Au(OA)][Cl]}{[AuCl][(OA)]} \qquad \text{Eq. (C.1)}$$

As the reaction occurs in solution phase, it is convenient to rearrange Eq. C.1 to Eq. C.2 and take the logarithm in both sides :

$$\log K_{sc} = \log \frac{[Au(OA)][Cl]}{[OA]} - \log[AuCl] \qquad \text{Eq. (C.2)}$$

Considering that the absorbance of the complex comes from the left term in the right side of Eq. C.2, we isolated this term rearranging the Eq. C.2 to :

$$\log \frac{[Au(OA)][Cl]}{[OA]} = \log K_{sc} + \log[AuCl] \qquad \text{Eq. (C.3)}$$

In the next step, we take into account the Beer's law showed in Eq. C.4, where we see that the absorbance at a specific wavelength (A_λ) is directly proportional to the concentration (C_c) of the complex. In this Equation, the terms ε_m and b represent the molar absorptivity of the complex and the cell pathlength, respectively.

$$A_\lambda = \varepsilon_m . b . C_c \qquad \text{Eq. (C.4)}$$

The absorbance of the complex can be defined as a ratio between its maximum (A_{max}) and minimum (A_{min}) absorbance at a specific wavelength. In this case, the term A_{max} refers to the condition where all Au(I) ions were complexed by OA. The ratio A_{max}/A_{min} should still be corrected by subtraction of the absorbance A, which correspondents to the absorbance at the equilibrium number of moles for different concentrations of AuCl. Thus, the term in the left side of Eq. C.3 can be correlated with the absorbance of the complex by:

$$\frac{[Au(OA)][Cl]}{[OA]} = \frac{A_{max} - A}{A - A_{min}} \qquad \text{Eq. (C.5)}$$

By substituting the right term of Eq. C.5 in Eq. C.3, the following expression for spectrophotometric determination of the stability constant is obtained:

$$\log \frac{A_{max} - A}{A - A_{min}} = \log K_{sc} + \log [AuCl] \qquad \text{Eq. (C.6)}$$

Bibliography

[1] Y. Peidong, *Dalton Trans.*, 4387 (**2008**).

[2] F. Patolsky, C. M. Lieber, *Materials Today 8*, 20 (**2005**).

[3] Y. Huang, X. Duan, C.M. Lieber, *Small 1*, 142 (**2005**).

[4] L. M. Peter, *Phys. Chem. Chem. Phys.*, *9*, 2630 (**2007**).

[5] C. M. Lieber, *MRS Bull. 28*, 486 (**2003**).

[6] L. Cademartiri, G. A. Ozin, *Adv. Mater. 21*, 1013 (**2009**).

[7] A. Halder, N. Ravishankar, *Adv. Mater. 19*, 1854 (**2007**).

[8] C. Wang, C. Hu, C. M. Lieber, S. Sun, *J. Am. Chem. Soc. 130*, 8902 (**2008**).

[9] X. Lu, M. S. Yavuz, H. –Y. Tuan, B. A. Korgel, Y. Xia, *J. Am. Chem. Soc. 130*, 8900 (**2008**).

[10] Z. Huo, Z. K. Tsung, W. Huang, X. Zhang, P. Yang, *Nano Lett. 8*, 2041 (**2008**).

[11] N. Pazos-Pérez, D. Baranov, S. Irsen, M. Hilgendorff, L. M. Liz-Marzán, M. Giersig, *Langmuir, 24*, 9855 (**2008**).

[12] Feng, H.; Yang, Y.; You, Y.; Li, G.; Guo, J.; Yu, T.; Shen, Z.; Wu, T.; Xing, B. Chem. Commun. *15*, 1984 (**2009**).

[13] B. Hammer, J. K. Norskov, *Nature 376*, 238 (**1995**).

[14] J. K. Norskov, *J. Chem. Phys. 90*, 7461 (**1989**).

[15] R. J. Puddephatt, The Chemistry of Gold, Elsevier, Amsterdam, **1978**.

[16] H. Schmidbaur, S. Cronje, B. Djordjevic, O. Schuster, *Chem. Phys. 311*, 151 (**2005**).

[17] E. Pyykko, *Chem. Rev. 88*, 563 (**1988**).

[18] H. Schmidbaur, *Gold Bull. 23*, 11 (**1990**).

[19] H. Schmidbaur, A. Schier. *Chem. Soc. Rev. 37*, 1931 (**2008**).

[20] G. J. Hutchings, M. Brust, H. Schmidbaur, *Chem. Soc. Rev. 37*, 1759 (**2008**).

[21] P. G. Jones, *Gold Bull. 14*, 102 (**1981**).

[22] P. G. Jones, *Gold Bull. 14*, 159 (**1981**).

[23] P. G. Jones, *Gold Bull. 16*, 114 (**1983**).

[24] P. G. Jones, *Gold Bull. 19*, 46 (**1986**).

[25] M. J. Irwin, J. J. Vittal, G. P. A. Yap, R. J. Puddephatt, *J. Am Chem. Soc. 118*, 13101 (**1996**).

[26] W. J. Hunks, M. C. Jennings, R. J. Puddephatt, *Inorg. Chem. 41*, 4590 (**2002**).

[27] C. A. Wheaton, R. J. Puddephatt, *Angew. Chem. 46*, 4461 (**2007**).

[28] M. J. Katz, K. Sakai, D. B. Leznoff, *Chem. Soc. Rev. 37*, 1884 (**2008**).

[29] M. J. Katz, P. M. Aguiar, R. J. Batchelor, A. A. Bokov, Z.-G. Ye, S. Kroeker, D. B. Leznoff, *J. Am. Chem. Soc. 128*, 3669 (**2006**).

[30] P. Espinet, *Gold Bull. 32*, 127 (**1999**).

[31] R. E. Bachman, M. S. Fioritto, S. K. Fetics, T. M. Cocker, *J. Am. Chem. Soc. 123*, 5376 (**2001**).

[32] R. M. Penner, C. R. Martin, *Anal. Chem. 59*, 2625 (**1987**).

[33] V. P. Menon, C. R. Martin, *Anal. Chem. 67*, 1920 (**1995**).

[34] Y. Kobayashi, C. R. Martin, *Anal. Chem. 71*, 3665 (**1999**).

[35] J. Choi, G. Sauer, K. Nielsch, R. B. Wehrspohn, U. Gösele, *Chem. Mater. 15*, 776 (**2003**).

[36] J. L. Coffer, S. R. Bigham, X. Li, R. F. Pinizzotto, Y. G. Rho, R. M. Pirtle, I. L. Pirtle, *Appl. Phys. Lett. 69*, 3851 (**1996**).

[37] E. Braun, Y. Eichen, U. Sivan, G. Ben-Yoseph, *Nature 391*, 775 (**1998**).

[38] Y. Zhang, H. J. Dai, *Appl. Phys. Lett. 77*, 3015 (**2000**).

[39] E. Kapon, K. Kash, E. M. Clausen Jr., D. M. Hwang, E. Colas, *Phys. Phys. Lett. 60*, 477 (**1992**).

[40] J. C. Hulteen, C. R. Martin, *J. Mater. Res. 7*, 1075 (**1997**).

[41] B. Z. Tang, H. Xu, *Macromolecules 32*, 2569 (**1999**).

[42] H. Masuda, K. Fukuda, *Science*, *268*, 466 (**1995**).

[43] A. P. Li, F. Müller, A. Birner, K. Nielsch, U. Gösele, *J. Appl. Phys. 84*, 6023 (**1998**).

[44] B. Xu, H. He, N. J. Tao, *J. Am. Chem. Soc. 124*, 13568 (**2002**).

[45] A. Bogozi, O. Lam, H. He, C. Li, N. J. Tao, L. A. Nagahara, I. Amlani, R. Tsui, *J. Am. Chem. Soc. 123*, 4585 (**2001**).

[46] C. Z. Li, H. X. He, A. Bogozi, J. S. Bunch, N. J. Tao, *Appl. Phys. Lett. 76*, 1333 (**2000**).

[47] Y. Xia, P. Yang, Y. Sun, Y. Wu, B. Mayers, B. Gates, Y. Yin, F. Kim, H. Yan, *Adv. Mater. 15*, 353 (**2003**).

[48] Y. –Y. Yu, S. S. Chang, C. –L. Lee, C. R. C. Wang, *J. Phys. Chem. B 101*, 6661 (**1997**).

[49] C. J. Murphy, N. R. Jana, *Adv. Mater. 14*, 80 (**2002**).

[50] Y. Xiong, Y. Xia, *Adv. Mater. 19*, 3385 (**2007**).

[51] Y. Xia, Y. Xiong, B. Lim, S. E. Skrabalak, *Angew. Chem. Int. Ed. 48*, 60 (**2009**).

[52] Z. L.Wang, *J. Phys. Chem. B 104,*1153 (**2000**).

[53] G. Wulff, *Zeits F. Kristallog. 34*, 449 (**1901**).

[54] L. D. Marks, *Rep. Prog. Phys. 57*, 603 (**1994**).

[55] Y. Sun, B. Mayers, T. Herricks, Y. Xia, *Nano Lett. 3*, 955 (**2003**).

[56] A. Henglein, *J. Phys. Chem. 97*, 5457 (**1993**).

[57] P. L. Rossiter, *The Electrical Resisitivity of Metals and Alloys* (Cambridge Univ. Press, Cambridge, 1987).

[58] J. Voit, *Rep. Prog. Phys. 57*, 977 (**1994**).

[59] C. A. Stafford, *Phys. stat. sol.* (b) *230*, 481 (**2002**).

[60] T. J. Counts, *Electrical Conduction in Thin Metal Films* (Elsevier Scientific Publishing Company), Amsterdam (**1974**).

[61] K. Fuchs, *Proceed. Camb. Phil. Soc. 34*, 100, (**1938**).

[62] E. H. Sondheimer, *Adv. Phys. 1*, 1 (**1952**).

[63] R. G. Chambers, *Proceed. Camb. Phil. Soc., 202*, 378, (**1950**).

[64] K. K. Likharev, *IBM J. Res. Develop. 32*, 144 (**1988**).

[65] J. O. Bockris, M. A. Devanathan, and K. Müller, *Proc. R. Soc. 55*, A274 (**1963**).

[66] J.O. Bockris, A. K. N. Reddy, *Modern electrochemistry*, Plenum Press, New York (**1970**).

[67] A. J. Bard and L. R. Faulkner. Electrochemical Methods, Fundamentals and Applications. John Wiley & Sons, New York, NY, 2nd ed. (**2001**).

[68] E. Stern, R. Wagner, F. J. Sigworth, R. Breaker, T. M. Fahmy, M. A. Reed, *Nano Lett. 7*, 3405 (**2007**).

[69] J. D. Norton, H. S. White, S. W. Feldberg, *J. Phys. Chem. 94*, 6772 (**1990**).

[70] R. He, S. Chen, F. Yang, B. Wu, *J. Phys.Chem. B 110*, 3262 (**2006**).

[71] Y. Sun, Y. Liu, Z. Liang, L. Xiong, A. Wang, S. Chen, *J. Phys. Chem. C 113*, 9878 (**2009**).

[72] Y. Liu, R. He, Q. Zhang, S. Chen, *J. Phys. Chem. C 114*, 10812 (**2010**).

[73] S. Chen, A. Kucernak, *J. Phys. Chem. B 106*, 9396 (**2002**).

[74] H. Ogawa, M. Nishikawa, A. Abe, *J. Appl. Phys. 53*, 4448 (**1982**).

[75] R. E. Kandel, J. H. Schwartz, and T. M. Jessel. "Nerve Cells and Behavior." In "Principles of Neural Science," book chapter 2, pp. 24–25. McGraw-Hill Companies, 4th ed. (**2000**).

[76] N. A. Campbell, J. B. Reece, "Nervous System." In "Biology," pp. 1012–1043. Pearson Education Inc, (**2005**).

[77] J. Huguenard, D. A. McCormick, Electrophysiology of the neuron - An interactive tutorial. Oxford University Press, Inc., New York (**1994**).

[78] A. L. Hodgkin, A. F. Huxley, *J. Phys.*, *116*, 473 (**1952**).

[79] A. L. Hodgkin, A. F. Huxley. *J. Phys.*, *117*, 500 (**1952**).

[80] B. P. Bean, *Nature Rev. 8*, 451 (**2007**).

[81] L. A. Geddes, K. S. Foster, J. Reilly, W. D. Voorhees, J. D. Bourland, T. Ragheb, N. E. Fearnot, *IEEE Trans. Biomed. Eng.*, BME *34*, 669 (**1987**).

[82] R. Weis, P. Fromherz, *Phys. Rev. E 55*, 877 (**1997**).

[83] R. Weis, B. Müller, P. Fromherz, *Phys. Rev. Lett. 76*, 327 (**1996**).

[84] P. Fromherz, *Phys. E 16*, 24 (**2003**).

[85] L. J. Breckenridge, R. J. A. Wilson, P. Connolly, A. S. G. Curtis, J. A. T. Dow, S. E. Blackshaw, C. D. W. Wilkinson, *J. Neurosci. Res. 42*, 266 (**1995**).

[86] M. Grattarola, S. Martinoia, *IEEE Trans. Biom. Eng. 40*, 35 (**1993**).

[87] R. Lind, P. Connolly, C. D. W. Wilkinson, *Sens. Act. B 3*, 23 (**1991**).

[88] Z. L. Wang, Transmission Electron Microscopy and Spectroscopy of Nanoparticles in Characterization of nanophase materials. Wiley-VCH Verlag GmbH, (**2000**).

[89] C. L. Jia, M. Lentzen, K. Urban, *Science 299*, 870 (**2003**).

[90] M. Lentzen, *Microscopy and Microanalysis 12*, 191 (**2006**).

[91] V. A. Mikheev, *Cryogenics - US patent*, n. 5.829.270, Date 03 nov. (**1998**).

[92] W. C. Claycomb, N. A. Lanson Jr., B. S. Stallworth, D. B. Egeland, J. B. Delcarpio, A. Bahinski, N. J. Izzo Jr., *Proceed. Nat. Acad. Sci. 95*, 2979, (**1998**).

[93] N. A. Hampson, J. B. Lee, J. R. Morleya, B. Scanlo, *Can. J. Chem. 47*, 3729 (**1969**).

[94] T. Luczak, *J. Appl. Electrochem. 37*, 269 (**2007**).

[95] M. Iwahashi, Y. Yamaguchi, T. Kato, T. Horiuchi, I. Sakurai, M. Suzuki, *J. Phys. Chem. 95*, 445 (**1991**).

[96] P. Tandon, G. Förster, R. Neubert, S. Wartewig, *J. Mol. Struct. 524*, 201 (**2000**).

[97] W. L. Bragg, *Proceed. Camb. Phil. Soc. 17*, 43 (**1913**).

[98] M. Iwahashi, Y. Kasahara, H. Matsuzawa, K. Yagi, K. Nomura, H. Terauchi, Y. Ozaki, M. Suzuki, *J. Phys. Chem. B 104*, 6186 (**2000**).

[99] J. Muñiz, C. Wang, P. Pyykko, *Chem. Eur. J. 17*, 368 (**2011**).

[100] M. Goto, E. Ashida, *Bull. Chem. Soc. Jpn. 51*, 70 (**1978**).

[101] 10.07.2011, URL http://en.wikipedia.org/wiki/File:LiquidCrystal-MesogenOrder-SmecticPhases.jpg

[102] X. Lu, H. –Y. Tuan, B. A. Korgel, Y. Xia, *Chem. Eur. J. 14*, 1584 (**2008**).

[103] P. Alivisatos, *Nat. Biotechnol. 22*, 47 (**2004**).

[104] T. Dadosh, Y. Gordin Y, R. Krahne, I. Khivrich, D. Mahalu, V. Frydman, J. Sperling, A. Yacoby, I. Bar-Joseph, *Nature 436*, 677 (**2005**).

[105] R. J. Tseng, J. X. Huang, J. Ouyang, R. B. Kaner, Y. Yang, *Nano Lett. 5*, 1077 (**2005**).

[106] J. Turkevich, P. C. Stevenson, J. Hillier, *Discuss. Faraday Soc. 11*, 55 (**1951**).

[107] T. Huang, F. Meng, L. Qi, *J. Phys. Chem. C 113*, 13636 (**2009**).

[108] J. -P. Sylvestre, S. Poulin, A. V. Kabashin, E. Sacher, M. Meunier, J. H. T. Luong, *J. Phys. Chem. B 108*, 16864 (**2004**).

[109] A. Halder, N. Ravishankar, *J. Phys. Chem. B 110*, 6595 (**2006**).

[110] F. Mohr, M. C. Jennings, R. J. Puddephatt, *Angew. Chem. Int. Ed. 43,* 969 (**2004**).

[111] A. Dawson, P. V. Kamat, *J. Phys. Chem. B 104***,** 11842 (**2000**).

[112] C. Subramaniam, R. T. Tom, T. Pradeep, *J. Nanopart. Res. 7*, 209 (**2005**).

[113] X. Sun, S. Dong, E. Wang, *Mater. Chem. Phys. 96*, 29 (**2006**).

[114] M. E. Kuehne, T. C. Hall, *J. Org. Chem. 41*, 2742 (**1976**).

[115] B. C. Smith, *Infrared Spectral Interpretation: A Systematic Approach*; CRC Press, (**1999**).

[116] V. Gutmann, *Electrochim. Acta 21*, 661 (**1976**).

[117] M. Bernardi, S. N. Raja, S. K. Lim, *Nanotechnology 21*, 285607 (**2010**).

[118] Z. Lee, K.-J. Jeon, A. Dato, R. Erni, T. J. Richardson, M. Frenklach, V. Radmilovic, *Nano Lett. 9*, 3365 (**2009**).

[119] Z. Li, J. Tao, X. Lu, Y. Zhu, Y. Xia, *Nano Lett. 8*, 3052 (**2008**).

[120] B. Wiley, T. Herricks, Y. Sun, Y. Xia, *Nano Lett. 4*, 1733 (**2004**).

[121] H. Hofmeister, S. A. Nepijko, D. N. Levlev, W. Schulze, G. Ertl, *J. Cryst. Growth 234*, 773 (**2002**).

[122] N. R. Jana, L. Gearheart, S. O. Obare, C. J. Murphy, *Langmuir 18*, 922 (**2002**).

[123] J. Rodriguez-Fernendez, J. Perez-Juste, P. Mulvaney, L. M. Liz-Marzan, *J. Phys. Chem. B 109*, 14257 (**2005**).

[124] A. Henglein, *J. Phys. Chem. 97*, 5457 (**1993**).

[125] A. Ulman, *Chem. Rev. 96*, 1533 (**1996**).

[126] X. Tang, M. Tsuji, P. Jiang, M. Nishio, S. M. Jang, S.-H. Yoon, *Colloids Surf. A 338*, 33 (**2009**).

[127] B. Wiley, Y. Sun, Y. Xia, *Acc. Chem. Res. 40*, 1067 (**2007**).

[128] M. Tsuji, M. Hashimoto, Y. Nishizawa, M. Kubokawa, T. Tsuji, *Chem. Eur. J. 11*, 440 (**2005**).

[129] L. Gou, M. Chipara, J. M. Zaleski, *Chem. Mater. 19*, 1755 (**2007**).

[130] P. L. Gai, M. A. Harmer, *Nano Lett. 2*, 771 (**2002**).

[131] C. Wang, Y. Wei, H. Jiang, S. Sun, *Nano Lett. 10*, 2121 (**2010**).

[132] Y. Min, M. Akbulut, N. Belman, Y. Golan, J. Zasadzinski, J. Israelachvili, *Nano Lett. 8*, 246 (**2008**).

[133] P. A. Smith, C. D. Nordquist, T. N. Jackson, T. S. Mayer, B. R. Martin, J. Mbindyo, T. E. Mallouk, *Appl. Phys. Lett. 77*, 1399 (**2000**).

[134] J. Lee, A. A. Wang, Y. Rheem, B. Yoo, A. Mulchandani, W. Chen, N. V. Myunga, *Electroanalysis 19*, 2287 (**2007**).

[135] G. Yu, A. Cao, C. M. Lieber, *Nat. Nanotechnol. 2*, 372 (**2007**).

[136] E. M. Freer, O. Grachev, D. P. Stumbo, *Nat. Nanotech. 5*, 525 (**2010**).

[137] Y. Huang, X. Duan, Q. Wei, C.M. Lieber, *Science 291*, 630 (**2001**).

[138] Y. Li, J. –J. Delaunay, "Progress Toward Nanowire Device Assembly Technology" in Nanowires, edit. P. Prete, INTECH, Croatia, march (**2010**).

[139] R. Holm, D. Söderberg, *Rheol. Acta 46*,721 (**2007**).

[140] Z. Zhong, D. Wang, Y. Cui, M.W. Bockrath, C. M. Lieber, *Science 302*, 1377 (**2003**).

[141] D. C. J. W. Schwaab, Surface patterning by means of Soft Lithography for Molecular and Bio-Electronics, PhD Thesis, RWTH Aachen (**2007**).

[142] Y. Lu, J. Y. Huang, C. Wang, S. Sun, J. Lou, *Nat. Nanotechnol. 5*, 218 (**2010**).

[143] C. M. Lilley, Q. Huang, *Appl. Phys. Lett. 89*, 203114 (**2006**).

[144] P. S. Ho, T. Kwok, *Rep. Prog. Phys. 52*, 301 (**1989**).

[145] C. Durkan, M. A. Schneider, M. E. Welland, *J. Appl. Phys. 86*, 1280 (**1999**).

[146] D. Aherne, A. Satti, D. Fitzmaurice, *Nanotechnology 18*, 125205 (**2007**).

[147] S. Karim, K. Maaz, G. Ali, W. Ensinger, *J. Phys. D: Appl. Phys. 42*, 185403 (**2009**).

[148] P. L. Rossiter: *The Electrical Resisitivity of Metals and Alloys* (Cambridge Univ. Press, Cambridge) **1987**.

[149] C. M. Lilley, Q. Huang, "Electrical Properties of Metallic Nanowires for Nanoelectronic Applications" in Nanoelectronics: Nanowires, molecular electronics and nanodevices, ed. by K. Iniewski, New York, McGraw-Hill (**2011**).

[150] P. Sheng, *Phys. Rev. B 21*, 2180 (**1980**).

[151] Y. -H. Lin, S. –P. Chiu, J. –J. Lin, *Nanotechnology 19*, 365201 (**2008**).

[152] P. Sheng, E. K. Sichel, J. I. Gittleman, *Phys. Rev. Lett. 40*, 1197 (**1978**).

[153] J. G. Simmons, *J. Appl. Phys. 34*, 1793 (**1963**).

[154] A. Kühnle, *Curr. Opin. Colloid Interface Sci. 14*, 157 (**2009**).

[155] L. Kogut, K. Komvopoulos *J. Appl. Phys. 94*, 3153 (**2003**).

[156] F. -B. Li, A. R. Hillman, S. D. Lubetkin. *Electrochimica Acta*, *37*, 2715 (**1992**).

[157] J. C. Love, L. A. Estroff, J. K. Kriebel, R. G. Nuzzo, G. M. Whitesides, *Chem. Rev. 105*, 1103 (**2005**).

[158] W. Lee, M. Hara, H. Lee, *Mat. Sci. Eng. C 24*, 315 (**2004**).

[159] S. S. Narayanan, S. S. Sinha, P. K. Verma, S. K. Pal, *Chem. Phys. Lett. 463*, 160 (**2008**).

[160] B. N. J. Persson, *Phys. Rev. B 44*, 3277 (**1991**).

[161] B. K. Duan, J. Zhang, P. W. Bohn, *Anal. Chem. 84*, 2 (**2012**).

[162] B. Xu, H. He, N. J. Tao, *J. Am. Chem. Soc. 124*, 13568 (**2002**).

[163] B. Xu, H. X. He, S. Boussaad, N. J. Tao, *Electrochim. Acta*, *48*, 3085 (**2003**).

[164] N. J. Tao, *J. Chem. Educ. 82*, 720 (**2005**).

[165] T. Ishida, N. Choi, W. Mizutani, H. Tokumoto, I. Kojima, H. Azehara, H. Hokari, U. Akiba, M. Fujihira, *Langmuir 15*, 6799 (**1999**).

[166] Y. Zhang, R. H. Terrill, P. W. Bohn, *Anal. Chem. 71*, 119 (**1999**).

[167] Y. Zhang, R. H. Terrill, P. W. Bohn, *J. Am. Chem. Soc. 120*, 9969 (**1998**).

[168] C. E. Housecroft, A. G. Sharpe, *Inorganic Chemistry* (3rd ed.). Prentice Hall. ISBN 978-0131755536. Chapter 6: Acids, Bases and Ions in Aqueous Solution, (**2008**).

[169] W. –C. Lin, S. –H. Lee, M. Karakachian, B. –Y. Yu, Y. –Y. Chen, Y.-C. Lin, C.-H. Kuo, J. –J. Shyue, *Phys. Chem. Chem. Phys. 11*, 6199 (**2009**).

[170] Y.-C. Lin, B. -Y. Yu, W.-C. Lin, S.-H. Lee, C.-H. Kuo, J. -J. Shyue, *J. Colloid Interface Sci. 340*, 126 (**2009**).

[171] J. -J. Shyue, M. R. De Guire, T. Nakanishi, Y. Masuda, K. Koumoto, C. N. Sukenik, *Langmuir*, *20*, 8693 (**2004**).

[172] R. Schweiss, P. B. Welzel, C. Werner, W. Knoll, *Colloids Surf. A: Phys. Eng. Asp. 195*, 97 (**2001**).

[173] H.-J. Butt, K. Graf, and M. Kappl. *Physics and Chemistry of Interfaces.* Wiley-VCH, Berlin (**2003**).

[174] L. S. Jung, C. T. Campbell, *J. Phys. Chem. B 104*, 11168 (**2000**).

[175] H.-Y. Lin, H.-A. Chen, H.-N. Lin, *Anal. Chem. 80*, 1937 (**2008**).

[176] D.-E. Jiang, K. Nobusada, W. Luo, R. L. Whetten, *ACS Nano 3*, 2351 (**2009**).

[177] X. Zhou, J. M. Moran-Mirabal, H. G. Craighead, P. L. McEuen. *Nat. Nanotechnol. 2*, 185 (**2007**).

[178] Y. Lin, H. Skaff, T. Emrick, A. D. Dinsmore, T. P. Russell. *Science 299*, 226 (**2003**).

[179] B. Davidson, G. D. Fasmant, *Biochemistry 6*, 1616 (**1967**).

[180] G. Witz, B. L. Van Duuren, *J. Phys. Chem. 77,* 648 (**1973**).

[181] F. Johansson, P. Carlberg, N. Danielsen, L. Montelius, M. Kanje, *Biomaterials 27*, 1251 (**2006**).

[182] B. Hille, *Biophys. J. 22*, 283 (**1978**).

[183] M. H. Ulbrich, P. Fromherz, *Appl. Phys. A 81*, 887 (**2005**).

[184] M. Schmidtner, P. Fromherz, *Biophys. J. 90*, 183 (**2006**).

[185] C. K. Yeung, F. Sommerhage, G. Wrobel, A. Offenhäusser, M. Chan, S. Ingebrandt, *Anal. Bioanal. Chem. 387*, 2673 (**2007**).

[186] P. Tyagi, D. Postetter, D. L. Saragnese, C. L. Randall, M. A. Mirski, D. H. Gracias, *Anal. Chem. 81*, 9979 (**2009**).

[187] J. M. Armstrong, J. Millar, *J. Neurosci. Meth. 1*, 279 (**1979**).

[188] M. K. Gheith, T. C. Pappas, A. V. Liopo, V. A. Sinani, B. S. Shim, M. Motamedi, J. P. Wicksted, N. A. Kotov, *Adv. Mater. 18*, 2975 (**2006**).

[189] F. Patolsky, B. P. Timko, G. Yu, Y. Fang, A. B. Greytak, G. Zheng, C. M. Lieber, *Science 313*, 1100 (**2006**).

[190] G. J. Brewer, J. R. Torricelli, E. K. Evege, P. J. Price, *J. Neurosci. Res. 5*, 567 (**1993**).

CURRICULUM VITAE

Alexandre Kisner, B.Sc. in Chemistry, M.Sc. in Chemistry

E-mail: kisner.alexandre169@gmail.com

Date of Birth: 6th January, 1982
Place of Birth: Blumenau, SC, Brazil
Nationality: Brazilian
Marital Status: Single

Education

2008 - 2012 PhD at Julich Research Center, RWTH Aachen, Germany. Thesis: Ultrathin Au Nanowires: Chemistry, Electrical Characterization and Application to Sense Cellular Biology

2005 - 2007 MSc, Institute of Chemistry, Campinas State University (UNICAMP), Brazil. Master thesis: Development of a New ISFET Configuration for Highly Sensitive Detection of Chemical and Biological Species.

2000 - 2005 B.A. in Chemistry, Universidade Regional de Blumenau, Brazil

Full List of Publications

1. Arnaldo C. Pereira, Marina R. Aguiar, **Alexandre Kisner**, Denise V. Macedo, Lauro T. Kubota, Amperometric Biosensor for Lactate Dehydrogenase and Meldola Meldola Blue Coimmobilized on Multiwall Carbon Nanotube, *Sensors and Actuators B* **124**, 269 – 276 (2007).

2. Andreas Feuerhack, Mandy Alisch-Mark, **Alexandre Kisner**, Sérgio Henrique Pezzin, Wolfgang Zimmermann, Jürgen Andreaus, Biocatalytic surface modification of knitted fabrics made of poly (ethylene terephthalate) with hydrolytic enzymes from *Thermobifida fusca* KW3b, *Biocatalysis and Biotransformation*, **2008**, *26*, 357-364.

3. **A. KISNER**, M. R. AGUIAR, A. F. VAZ, A. ROJAS, F. A. CAVARSAN, J. A. DINIZ, L. T. KUBOTA, Submicrometer-MOS Capacitor with Ultra High Capacitance biased by Au Nanoelectrodes, *Applied Physics A: Materials Science & Processing*, **2008**, *94*, 831-836. DOI: 10.1007/s00339-008-4860-0.

4. **Alexandre Kisner**, Marina Rodrigues de Aguiar, and Lauro T. Kubota, Giant enhancement of light emission from Au nanocrystals into a porous matrix integrated with silicon platform, *Journal of Nanoscience and Nanotechnology* **2009**, *9*, 2592-2597.

5. **Alexandre Kisner,** Steffi Lenk, Dirk Mayer, Yulia Mourzina, Andreas Offenhaeusser, Determination of the Stability Constant of the Intermediate Complex during the Synthesis of Au Nanoparticles Using Aurous Halide, *Journal of Physical Chemistry C* **2009,** *113,* 20143–20147.

6. **Kisner, A.;** Heggen, M.; Tillmann, K.; Mourzina, Y.; Offenhäusser, A. Synthesis and Structural Characterization of Ultra-thin Flexible Au Nanowires. *Mater. Res. Soc. Symp. Proc.* Vol. 1206, 2010, Materials Research Society. 1206-M16-29.

7. Arnaldo César Pereira, **Alexandre Kisner,** César Ricardo Teixeira Tales, Nelson Duran and Lauro Tatsuo Kubota, Determination of Phenol Compounds Based on Electrodes with HRP Immobilized on Oxidized Multi-Wall Carbon Nanotubes. *Dynamic Biochemistry, Process Biotechnology and Molecular Biology.* **2009**, 3, 75-79.

8. Arnaldo C. Pereira, **Alexandre Kisner**, Nelson Duran, Lauro T. Kubota, The effects of dimensionality on electrochemical sensors based on carbon nanotubes and metallic nanowires. *Journal of Nanoscience and Nanotechnology*, **2010** Feb;10(2):651-67.

9. Arnaldo C. Pereira, **Alexandre Kisner**, César R. T. Tarley, Lauro T. Kubota, Development of a Carbon Paste Electrode for Lactate Detection Based on Meldola's Blue Adsorbed on Silica Gel Modified with Niobium Oxide and Lactate Oxidase. *Electroanalysis*, **2011**, 23, No. 6, 1470 – 1477.

10. Jaydeep Bhattacharya, **Alexandre Kisner**, Andreas Offenhäusser, Bernhard Wolfrum, Microfluidic anodization of aluminum films for the fabrication of nanoporous lipid bilayer support structures. *Beilstein J. Nanotechnol.* **2011,** *2,* 104–109.

11. **Alexandre Kisner**, Marc Heggen, Enrique Fernandez, Steffi Lenk, Dirk Mayer, Ulrich Simon, Andreas Offenhaeusser, Yulia Mourzina, The Role of Oxidative Etching in the Synthesis of Ultrathin Single-Crystalline Au Nanowires. *Chem. Eur. J.* **2011**, *17*, 9503-9507.

12. **Alexandre Kisner**, Regina Stockmann, Michael Jansen, Ugur Yegin, Andreas Offenhäusser, Lauro Tatsuo Kubota, Yulia Mourzina, Sensing Small Neurotransmitter-Enzyme Interaction with Nanoporous Gated Ion-Sensitive Field Effect Transistors. *Biosensors and Bioelectronics.* **2011**, *31*, 157-163.

13. **Alexandre Kisner**, Marc Heggen, Werner Fischer, Karsten Tillmann, Andreas Offenhäusser, Lauro Tatsuo Kubota and Yulia Mourzina, In situ Fabrication of Ultrathin Porous Alumina and its Application for Nanopatterning Au Nanocrystals on the Surface of Ion-sensitive Field-Effect Transistors. *Accepted for publication at Nanotechnology.*

Chapter of Books

1. Arnaldo César Pereira, **Alexandre Kisner,** Nelson Duran and Lauro Tatsuo Kubota, Chapter 5: Functional Low-Scale Electrodes in Electrochemical Systems. Book: *Nanostructured Materials in Electrochemistry.* ISBN-13: 978-3-527-31876-6 - Wiley-VCH, Weinheim.

2. César Ricardo Teixeira Tales, Gustavo Silveira, Bruno Eduardo Lobo Baeta, Vivian Silva Santos, Lucas Rossi Sartori, **Alexandre Kisner**, Arnaldo César Pereira, Lauro Tatsuo Kubota, Carbon Nanotubes: Application of this Nanostructured Material for the Development of Analytical Methods. *Book: Carbon Nanotubes: New Research* - ISBN 978-1-60692-236-1 – Pub. Date 2009 1st quarter, p. 371-406, Nova Science Publishers, Inc.

Patents

1. **Alexandre Kisner**, Martinho Rau, Celso Nicoletti and Lauro Tatsuo Kubota, Alkali treatment and recycling of laminated packaging. INPI – (National Institute of Industrialized Products) PI0706115-3, **2008**.

2. **Alexandre Kisner**, Fabio Aparecido Cavarsan, José Alexandre Diniz and Lauro Tatsuo Kubota, Development of ISFET sensors-based Ag and Au nanoelectrodes. INPI – (National Institute of Industrialized Products) PI 0900537-4 A2, **2011**.

Acknowledgement / Danksagung

It does not matter how alone someone can lead his/her PhD thesis, especially in my case with this PhD work that was only possible due to the generous support I have received throughout the last three/four years in Juelich. Many people contributed to the work presented here and many facts had a strong influence in the encouragement to continue this project. Although mere words cannot express my gratitude, it gives me great pleasure to have this small opportunity to thank everyone who contributed to this work.

Firstly, I thank Prof. Dr. Offenhäusser so much for the opportunity to work and develop research with such friendly and multidisciplinary group. Also, I am very grateful for his financial support with the training group of biointerface in RWTH and the grant provided by the Deutsche Forschungsgemeinschaft (DFG). Apart from these, personally I consider Prof. Dr. Offenhäusser one of the most generous, modest, polite and open minded scientist I have ever met, and due to all of these human qualities, nochmals Ich Danke ihm sehr viel.

I also thank very much Dr. Yulia Mourzina, who was not only my group leader but also a nice friend that was always there when I needed and provided me really deep insights and criticism in analytical chemistry and science in general. Dr. Mourzina was also always very comprehensive, motivated and with a great interdisciplinary background, which summed up with her nice personality helped us to always work together having a good relationship. Spasibo Yu !

Although we met only a couple of times and exchanged a few words and e-mails, I am very grateful for the opportunity to have had Prof. Dr. Simon as my co-supervisor. He always provided me nice advices and transmitted me great motivation with so much positivism. Vielen Dank für alles Prof. Simon.

Two other great scientists and friends that I had the opportunity to work and share a lot of ideas were Dr. Dirk Mayer and Dr. Bernhard Wolfrum. I thank each one so much for every moment spent together, even when we were on the kicker. Their optimism and perseverance are inspiring and always transmitted me good feeling and motivation to walk ahead. Vielen, vielen, vielen Dank Dirk und Bernhard !

I owe a huge debt of gratitude to a lot of other people from the ICS-8/PGI-8 Institute for the friendship and help: Niklas and Philipp, my former and my last officemate, two great

German teachers. Also, Herr Wolters and Herr Otto for technical help with electronics and repair of instruments. My gratitude to all cleanroom's staff as well as to Regina Stockmann (Re du bist super), Marko Banzet, Michael Prömpers and Frau E. Brauweiler-Reuters for help with the cleanroom work and electron microscope recordings. Moreover, moving to the electrophysiological labs I thank so much R. Fricke, B. Hofmann, S. Eick, J. Enscherman and especially V. Maybeck, who I consider a great biologist. Besides the mentioned people, many others as S. Pud, M. Jansen, U. Yegin, M. Huske, S. Gilles, N. Sanetra, J. Brusius, Jaydeep and Dzmitry always gave me a hand when I needed it and for all I thank a lot each help and each moment spent together. I would especially like to thank also two guys that were more than only nice labmates, but were and still are two great friends, Alexey (il Russo) and Jan (my Schnitzel, as he likes to say). Without them, the days would not have the same taste and we would not have the same joy, spasibo and vielen Dank Russo and Jan !

I would also like to thank collaborators from other Institutes at Forschungszentrum Juelich, in special Ruslan Temirov, Dagmawi, Frau Lenki and Dr. Marc Heggen, who helped me with HRTEM analysis and had an essential participation on the walking of this work. To all, I really thank so much for everything.

Outside from the institute, many other people contributed indirectly for constant encouragement and motivation to develop something good to science and our daily life. I feel incredibly lucky to have had the chance to find such good friends as Rosanna, Sandipan, Greta, Giannis, Yan, Rodolfo, Raquel, Shirin, Enrique, Tânia, Dieter, Karolina, Ana, Nicola, Diego, David lo Parcero, Rosanita, Susy, Frau Tamburro, Giulia, Samir, Paulo, Eylem, Lyndi, Robert and many others that together led us to establish the famous *Fantastic Juelich.* My especial gratitude to Peppe Mercurio, who was a real brother to me and one of the most fantastic and optimistic person I have ever met. I am really happy to have had him as a friend during my period in Juelich. Troppo Danke all and I hope that it will be continued…

I would also like to thank so much Mr. Pabst for his nice time spent together and giving me advices in everything. Although he is always alone in his office I suggest everyone when possible, stop there and exchange some words with him and hear his experience of life, it was very inspiring for me, vielen Danke Mr. Pabst ! Also, I have an especial thank to someone that unfortunately left this life so early, Dr. Kristin Michael. She was a mirror of happiness and her smiling was always very friendly and warm. I am very grateful to have met her, she was great at

the lab and helped not only me, but a lot of other people, so that she always will be in our hearts. Thank you for everything Kris, I wish you peace and love wherever you are.

Far away from Germany, I also had influence and contribution from other people. I thank so much Marina for long hours of talking on skype and do not let me alone. It was always very nice to exchange some conversation about everything, thanks for all Marina. In this sense of long distances skype conversation I am also very grateful for my friend Fabricio, who has been with me since our childhood, thank you so much my “Big Brother”.

Also, my especial thanks to my lovely Ceci for her constant love and patience. She is one of the most generous and good-heart person I have ever seen in life, her smile with her endeavors always made me strong and it has been wonderful to have her besides me along these couple of years. Muito obrigado por tudo minha querida !

Finally, my loving thanks to my parents to always give me the freedom to walk on my way, falling and rising, crying and smiling, running and walking and struggling and learning with the diabetes. I believe we are all a genetic combination from the chromosomes of our parents and their feelings and experiences along the life, so that I thank so much my mom for her tears and positivism to never give up, as well as I thank my dad for his efforts with his hard work and dedication to offer his only son the opportunity to study and transform this world in a better place. Aos dois, muito obrigado por sempre acreditar !

Juelich, April 2012

Schriften des Forschungszentrums Jülich
Reihe Information

1. **Ferrocenes as Potential Building Blocks for Molecular Electronics**
Self-Assembly and Tunneling Spectroscopy
by L. Müller-Meskamp (2008), 153 pages
ISBN: 978-3-89336-509-8

2. **Magnetic Proximity Effects in Highly-ordered Transition Metal Oxide Heterosystems studied by Soft x-Ray Photoemission Electron Microscopy**
by I. P. Krug (2008), XX, 180 pages
ISBN: 978-3-89336-521-0

3. **Seltenerd-basierte ternäre Oxide als alternative Gatedielektrika**
von J. M. Roeckerath (2008), 148 Seiten
ISBN: 978-3-89336-543-2

4. **Strominduzierte Magnetisierungsdynamik in einkristallinen Nanosäulen**
von R. Lehndorff (2009), I, 86 Seiten
ISBN: 978-3-89336-564-7

5. **Magnetization Dynamics in Magnetically Coupled Heterostructures**
von A. Kaiser (2009), X, 121 pages
ISBN: 978-3-89336-577-7

6. **Resistive switching in Pt/TiO_2/PT**
by D. S. Jeong (2009), vii, 133 pages
ISBN: 978-3-89336-579-1

7. **Electromechanical Force Microscopy and Tip-Enhanced Raman Spectroscopy for Polar Oxide Nanoparticles**
by S. Röhrig (2009), vi, 114 pages
ISBN: 978-3-89336-600-2

8. **Investigation of resistive switching in barium strontium titanate thin films for memory applications**
by W. Shen (2010), 114 pages
ISBN: 978-3-89336-608-8

9. **Nanostrukturierte Metallelektroden zur funktionalen Kopplung an neuronale Zellen**
von D. Brüggemann (2010), vii, 160 Seiten
ISBN: 978-3-89336-627-9

10. **Integration of resistive switching devices in crossbar structures**
by Chr. Nauenheim (2010), XII, 142 pages
ISBN: 978-3-89336-636-1

11. **Correlation between Raman spectroscopy and electron microscopy on individual carbon nanotubes and peapods**
by C. Spudat (2010). xiv, 125 pages
ISBN: 978-3-89336-648-4

12. **DC and RF Characterization of NiSi Schottky Barrier MOSFETs with Dopant Segregation**
by C. J. Urban (2010), iv, 151 pages
ISBN: 978-3-89336-644-6

13. **Alternative Systems for Molecular Electronics: Functionalized Carboxylic Acids on Structured Surfaces**
by M. C. Lennartz (2010), 183 pages
ISBN: 978-3-89336-667-5

14. **Highly conductive electrodes as diffusion barrier for high temperature applications**
by B. Meši (2010), VII, 138 pages
ISBN: 978-3-89336-670-5

15. **Modeling, Fabrication and Characterization of Silicon Tunnel Field-Effect Transistors**
by C. P. Sandow (2010), XIII, 112 pages
ISBN: 978-3-89336-675-0

16. **Substituted Coronenes for Molecular Electronics: From Supramolecular Structures to Single Molecules**
by P. Kowalzik (2010), ix, 149 pages
ISBN: 978-3-89336-679-8

17. **Resistive switching in TiO2 thin films**
by L. Yang (2011), VII, 117 pages
ISBN: 978-3-89336-707-8

18. **Crystal- and Defect-Chemistry of Fine Grained Thermistor Ceramics on $BaTiO_3$ Basis with BaO-Excess**
by H. Katsu (2011), xxvii, 163 pages
ISBN: 978-3-89336-741-2

19. **Flächenkontakte zu molekularen Schichten in der Bioelektronik**
von N. Sanetra (2012), XIII, 129 Seiten
ISBN: 978-3-89336-776-4

20. **Stacked device structures for resistive memory and logic**
by R. D. Rosezin (2012), 137 pages
ISBN: 978-3-89336-777-1

21. **Optical and electrical addressing in molecule-based logic circuits**
by M. Manheller (2012), XIV, 183 pages
ISBN: 978-3-89336-810-5

22. **Fabrication of Nanogaps and Investigation of Molecular Junctions by Electrochemical Methods**
by Z. Yi (2012), 132 pages
ISBN: 978-3-89336-812-9

23. **Thermal Diffusion in binary Surfactant Systems and Microemulsions**
by B. Arlt (2012), 159, xlvi pages
ISBN: 978-3-89336-819-8

24. **Ultrathin Gold Nanowires - Chemistry, Electrical Characterization and Application to Sense Cellular Biology**
by A. Kisner (2012), 176 pages
ISBN: 978-3-89336-824-2

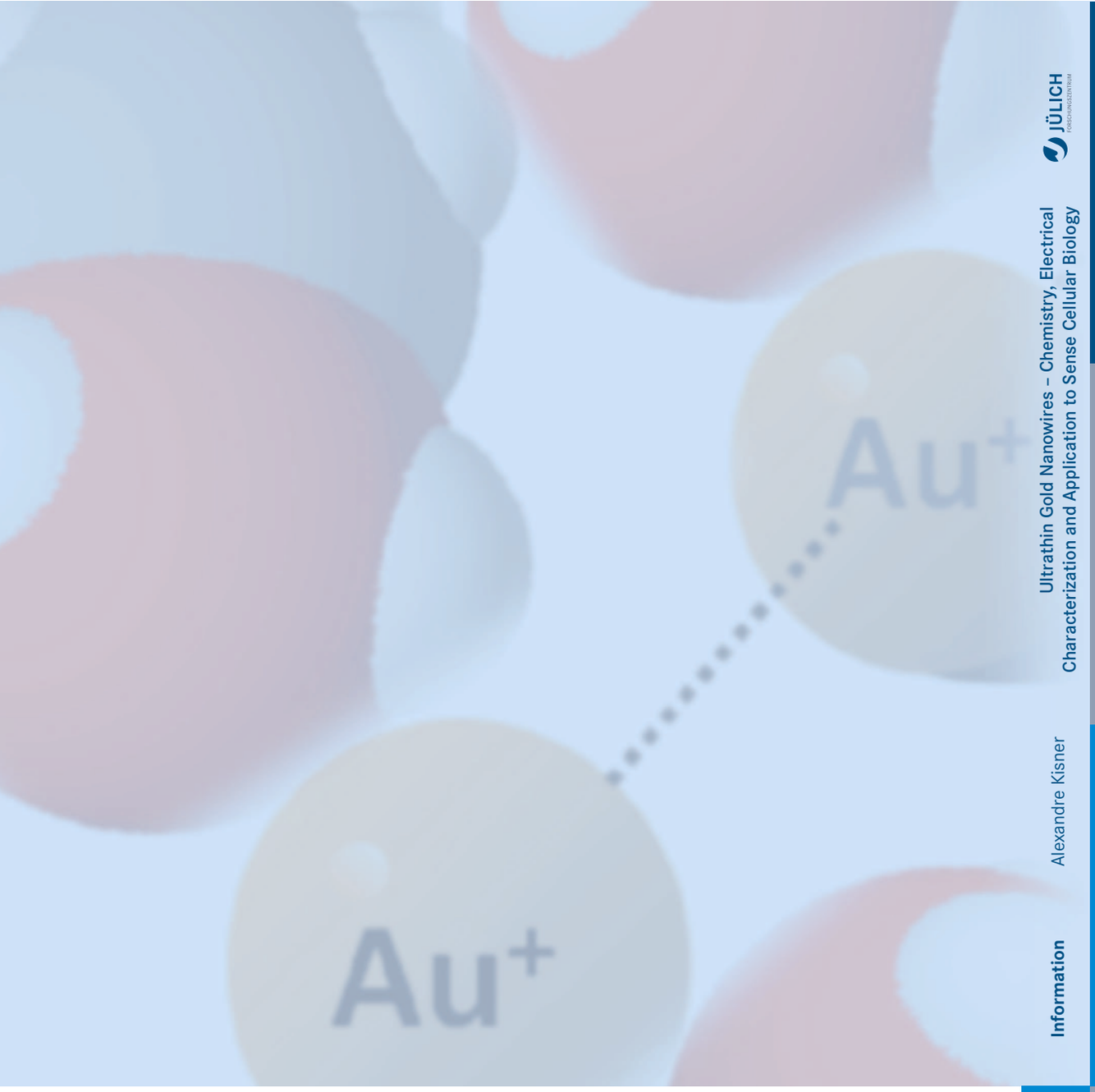

Information / Information
Band / Volume 24
ISBN 978-3-89336-824-2

JÜLICH
FORSCHUNGSZENTRUM

24

Member of the Helmholtz Association

Alexandre Kisner

Information

Ultrathin Gold Nanowires – Chemistry, Electrical Characterization and Application to Sense Cellular Biology

JÜLICH
FORSCHUNGSZENTRUM

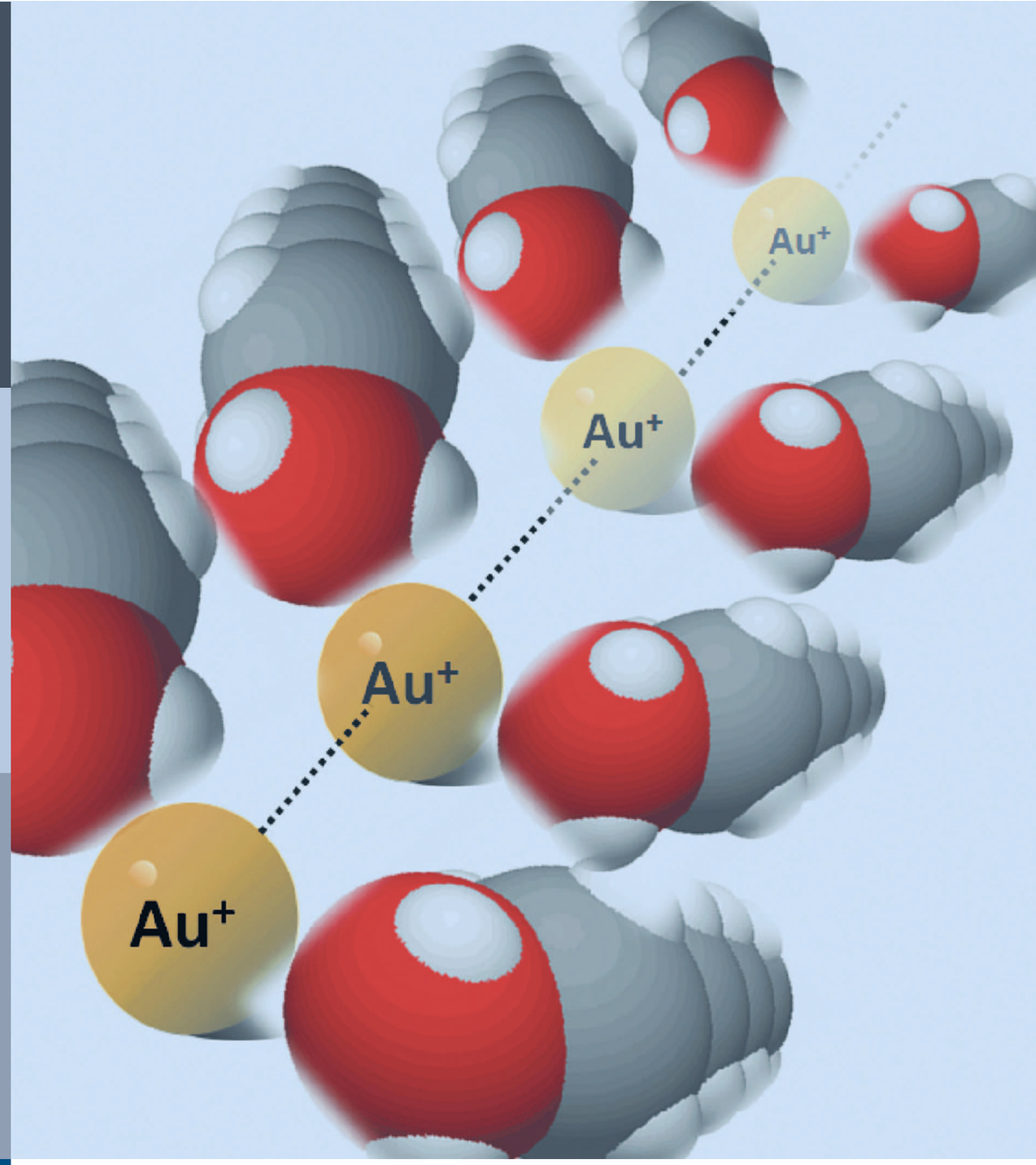

Ultrathin Gold Nanowires – Chemistry, Electrical Characterization and Application to Sense Cellular Biology

Alexandre Kisner

JÜLICH
FORSCHUNGSZENTRUM